OPTIMUM DESIGN OF STIFFENED COMPOSITE CYLINDRICAL SHELLS WITH A CUTOUT FOR MAXIMUM BUCKLING STRENGTH

by

Sezer Değer

B.S., Mechanical Engineering , Boğaziçi University, 2018

Submitted to the Institute for Graduate Studies in
Science and Engineering in partial fulfillment of
the requirements for the degree of
Master of Science

Graduate Program in Mechanical Engineering

Boğaziçi University

2022

ACKNOWLEDGEMENTS

First of all, I would like to express my deep gratitude to my thesis supervisor, Prof. Fazıl Önder Sönmez for his guidance, assistance, and philanthropy through this master study. I have learned from him how to approach a problem scientifically.

I would like to thank my life partner Betül for her love and endless support throughout my whole study. It would not be possible to finish this thesis without her support and I am grateful for having her by my side. I am also sending my love to our sweet cats Zoya and Tesla for always being lovely and fluffy.

I would also like to express my gratitude to my mother for always channeling me her positivity, my father for always believing in me from the very beginning of this study, and my brother for his empathy and all the chit chats we had.

Last but not least, I would like to thank my team leader Serdar for being an empathetic leader and giving me the opportunity to work flexibly for my studies, and my dear colleagues Tamer and Alperen for their support and helpfulness whenever I needed.

ABSTRACT

OPTIMUM DESIGN OF STIFFENED COMPOSITE CYLINDRICAL SHELLS WITH A CUTOUT FOR MAXIMUM BUCKLING STRENGTH

Thin-walled composite cylindrical shells have low resistance to buckling and out-of-plane deformations. Introducing a cutout to these structures reduces the load-carrying capacity of such structures drastically. One effective way to recover the load-carrying capacity lost due to a hole is to place stiffeners around the hole. The objective of this study is to find an optimum reinforcement for thin-walled composite cylindrical shells with a cutout to maximize the buckling load and minimize the additional mass due to the reinforcement.

A finite element model of a thin-walled composite cylinder with an opening is created and validated using the results of an experimental and numerical study. Then hat-type stiffeners are applied around the cutout. A parametric study is carried out to determine the effect of each stiffener parameter on the buckling strength of the structure and to choose suitable upper and lower limits for optimization. A modified simulated annealing algorithm is used to find the global optimum reinforcement design. Both the FEA and the optimizations are carried out using ANSYS Parametric Design Language (APDL). In the first step , the optimum designs are obtained for stiffeners placed in the axial direction at certain distances to the center of the cutout by varying only the cross-sectional parameters and the length of the stiffener. In the second stage, the distance to the hole center is also optimized. Finally, using the optimum stiffener dimensions optimization is performed by placing additional small stiffeners on the top and bottom of the cutout. Significant improvements are achieved by using optimum stiffener designs. The most effective parameters are found to be the stiffener length, stiffener distance to the center of the opening and stiffener height.

ÖZET

İNCE CİDARLI KOMPOZİT SİLİNDİRİK DELİKLİ KABUK YAPILARIN AZAMİ BURKULMA DİRENCİ İÇİN OPTİMUM TASARIMI

İnce cidarlı silindirik kabuk yapıların düzlem dışı eğilme ve burkulma dayanımları düşüktür. Bu yapılara açılan delikler, yapının yük taşıma kapasitesini önemli ölçüde azaltırlar. Delik dolayısıyla azalan yük taşıma kapasitesini artırmanın etkili bir yolu, delik etrafına berkiticiler uygulamaktır. Bu çalışmanın amacı, burkulma yükünü azami ve ağırlık artışını asgari düzeyde tutacak optimum berkiticiyle güçlendirme konfigürasyonunu bulmaktır.

Deneysel ve numerik bir çalışmanın sonuçları kullanılarak ince cidarlı kompozit silindirik delikli kabuk bir yapının sonlu elemanlar modeli oluşturuldu ve bu çalışmanın sonuçlarıyla kıyaslanarak doğrulandı. Akabinde delik etrafına şapka şeklinde berkiticiler uygulandı. Berkitici parametrelerinin her birinin yapının burkulma direncine etkisini incelemek ve optimizasyon için kullanılacak parametrelerin alt ve üst limitlerini belirlemek adına parametrik çalışmalar yapıldı. En iyi konfigürasyonu bulmak için yenilenmiş tavlama benzeşimi algoritması kullanıldı. Hem sonlu eleman analizleri, hem de eniyileme çalışmaları ANSYS Parametrik Tasarım Dili (APDL) kullanılarak gerçekleştirildi. İlk adımda, yalnızca berkiticilerin kesit alanı parametreleri ve berkitici uzunluğu değiştirilmek suretiyle deliğe belli bir uzaklıkta olan ve silindirin eksenel yönü boyunca uzanan berkiticiler için optimum tasarım bulundu. İkinci adımda deliğe olan mesafe değiştirilererek bir başka eniyileme daha yapıldı. Son olarak, bulunan optimum berkitici boyutları kullanılarak ekstra küçük berkiticiler deliğin üstüne ve altına uygulanarak eniyileme gerçekleştirildi. Optimum berkitici tasarımları kullanılarak önemli ölçüde iyileşmeler elde edildi. En etkili berkitici parametrelerinin berkitici uzunluğu, berkiticinin deliğe mesafesi ve bertkici yüksekliği olduğu sonucuna ulaşıldı.

TABLE OF CONTENTS

LIST OF FIGURES

LIST OF TABLES

LIST OF SYMBOLS

d_{st}	Circumferential distance between the center of the cutout and the axis of one stiffener
D	Flexural rigidity
$\{F\}$	Force vector
$[K]$	Stiffness matrix
h_{st}	Stiffener height
l_{arc}	Axial distance between the center of the cutout and the small stiffener
l_{st}	Stiffener length
$\{u\}$	Displacement vector
U	Strain energy
W	Virtual work
w_c	Width of the cap of the stiffener
w_f	Width of the flange of the stiffener
w_{total}	Total width of the stiffener
ε	Strain
λ	Load factor
Θ_{st}	Flange-to-cap angle of the stiffener
Θ_1	Inner layer fiber orientation of the patch
Θ_2	Outer layer fiber orientation of the patch

LIST OF ACRONYMS/ABBREVIATIONS

2D	Two Dimensional
3D	Three Dimensional
APDL	Ansys Parametric Design Language
ASTM	American Society for Testing and Materials
DSA	Direct Simulated Annealing
FEA	Finite Element Analysis
FEM	Finite Element Model
LBMI	Linear Buckling Mode-shape Imperfection
MSA	Modified Simulated Annealing
SA	Simulated Annealing
SPLA	Single Perturbation Load Approach

1. INTRODUCTION

1.1. Background

A material composed of two or more different materials is defined as a composite material. There are two kinds of constituent materials namely matrix and reinforcement. Reinforcement can be fibers or whiskers made of materials such as glass and carbon. Although these reinforcement elements have high strength in the direction of their length, they cannot form a structural element that can withstand loads without proper binding elements. Matrix, also called as binder, is the constituent that holds the reinforcement elements together, supporting them, protecting them and transmitting loads between reinforcement elements [1].

Thanks to different material properties of its constituent materials, a composite material can have properties tailored as desired such that its mechanical properties can be much better than its constituents. Depending on the composition, composite materials can have enhanced properties such as better durability, high resistance against corrosion, high strength-to-weight ratio. That is why composite materials always draw the attention of engineers.

Fiber reinforced composites (FRC), a type of composite material that has fibers as reinforcing element, are widely used for applications where weight is an important aspect. Therefore, high strength-to-weight ratio and increased rigidity of these materials make them highly favored against conventional isotropic materials such as plastics or metals. A few exemplary applications are racing car bodies, aerospace structures, aircraft wings and fuselages. Use of FRC for these applications is generally in the form of thin-walled curved panels or thin-walled cylindrical shells.

Considering the fuselage of an aircraft or a spacecraft, which is in the form of a thin-walled cylindrical shell, one or multiple cutouts are necessary for doors, windows,

or visual inspection openings. These cutouts lead to discontinuity in the stress and strain field of the structure under loading [2]. Introduction of openings not only leads to stress concentration that risks the safety of the structure against static loads, but also decreased buckling resistance of the structure, which is a crucial factor for fuselage applications since they work under high thrust loads. Additionally, these thin-walled cylindrical structures have low resistance for out-of-plane deformations. Consequently, cutouts lead to a significant reduction in the load-carrying capacity of a thin-walled cylindrical shell.

To remedy reduced load-carrying capacity of a thin-walled cylindrical shell under compression due to introduced cutout, the bending stiffness of the structure around the cutout must be increased. Rather than thickening the whole structure, use of stiffeners is a commonly used option that can increase the bending stiffness of the structure significantly without a significant increase in weight or material cost. Considering that thin-walled composite cylindrical shell structures are used for weight critical applications that also require high strength, achieving an optimum reinforcement design that provides high enough strength-to-weight ratio becomes a critical aspect for the structural design.

1.2. Literature Review

Buckling phenomenon has been the subject of concern for thin-walled structures in the literature. The fact that introducing an opening to a structure may lead to elevated stresses and also unstable deformation, decreasing the strength of the structure, has also been known for years. Tennyson [3] studied the effects of the presence of a circular cutout on the buckling performance of circular cylindrical shells. The results showed that increase in the ratio of radii of cutout to cylinder lead to a sudden reduction in the critical buckling load at a specific point beyond which further increase of the ratio had a decreased effect until the buckling load converged to a value. Jullien and Limam [4] conducted experimental and numerical studies on thin-walled cylindrical shells to investigate the effect of size, number and location of the cutout. They also

indicated that as the cutout size decreased, the effect of initial imperfection became dominant on determining the buckling load. Han et al. [5] also conducted an experimental and numerical investigation on the buckling response of thin walled cylindrical shells with cutout. In addition to examining the influence of cutout parameters on the buckling performance, an empirical equation was derived from the experimental results using the least-square method. Jacob et al. [6] compared the buckling performance of steel cylindrical shells with and without cutout based on experimental data. They also obtained a relation between the buckling load and the cutout size and location.

As thin-walled composite cylindrical shells proved to be a much better alternative to metallic materials because of their higher strength-to-weight ratio, buckling performance of such materials has drawn the attention of researchers. A numerical and experimental study conducted by Hilburger et al. [7] considered the buckling response of composite cylindrical shells with rectangular cutouts. The results indicated that the size of the cutout, material properties used and the amount of out-of-plane imperfections could considerably affect the buckling performance of the cylinder. Tafreshi [8] carried out a numerical investigation of the buckling response of composite shells with cutouts and found that increase in the size of the cutout lead to a decrease in the buckling load of the cylinder. Arbelo et al. [9] studied the effect of the presence of a cutout on a thin-walled composite cylindrical shell. The relation between the size of a cutout and the buckling load was investigated. Furthermore, the influence of initial imperfections on the buckling load of the structure was also investigated using single perturbation load approach (SPLA), a method of creating an imperfection on a structure via applying a lateral load to the location of the imperfection. The relationship between the amount of lateral load applied and the corresponding buckling load of the structure was determined. Celebi et al. [10] also investigated the effect of cutout size on the buckling load of a composite circular cylindrical shell with symmetric cutouts. The importance of the effect of initial imperfections on the buckling load of cylindrical shells was emphasized by comparing the results with and without taking into account the imperfections of the structure. Hühne et al. [11] also studied the buckling of thin-walled cylindrical shells using SPLA and showed that this method had a great potential to de-

sign against buckling without being too conservative. Taheri-Behrooz et al. [12] studied the impact of initial imperfections on the buckling behavior of composite cylindrical shells with cutout both experimentally and numerically. Linear buckling mode-shape imperfections (LBMI) and single perturbation load approach (SPLA) were both used to create imperfections. It was found that the presence of a cutout had much more dominant effect than the imperfections on the buckling load. Gangadhar and Kumar [13] numerically analyzed thin-walled composite cylindrical shells with and without cutouts to identify the effect of presence of a cutout. LBMI method along with a nonlinear analysis was used. They also compared the buckling resistance of the cylinder with rectangular and circular cutouts, and found that the latter had higher buckling load.

Some researchers investigated the effect of reinforcements on the strength of thin-walled composite cylindrical shells. Senocak et al. [14] studied the effect of hydrostatic compression and axial pressure on symmetrically laminated composite circular cylindrical shells with and without cutouts. Using minimum energy principle, they proposed an optimum edge reinforcement for a cutout. Hilburger et al. [15] conducted a parametric study to determine the effects of a patch reinforcement around the cutout in a cylindrical shell. They found that changing the thickness, the size and the ply orientations of the reinforcement patch could reduce the out-of-plane deformations and stresses around the cutout and postpone buckling of the structure. Jingxuan et al. [16] conducted a parametric study on the geometric parameters of cutout grid reinforcements on an advanced grid stiffened composite cylindrical shell with a cutout. The study proved that proper selection of parameters could prevent the local buckling around the cutout, leading to an increase in the global buckling load of the cylinder. Shi et al. [2] investigated the buckling and post-buckling responses of axially loaded advanced grid-stiffened carbon-fiber composite cylindrical shells with reinforced circular and rectangular cutouts. Skin reinforcements and grid reinforcements were compared. Different grid configurations were analyzed. Comparing the strength of cylindrical shells with rectangular and circular cutouts, the former showed lower strength against buckling due to increased stress concentrations with rectangular cutout. Also comparing skin reinforcements and grid reinforcements around the cutout, the latter showed better

performance against buckling when a configuration that can transmit loads smoothly was found. Hao et al. [17] proposed curvilinear stiffener reinforcement around a cutout on a thin-walled aluminum cylindrical shell with a rectangular cutout. A hybrid bilevel optimization method was used to obtain the optimum design for metallic stiffeners. Alhajahmad et al. [18] proposed a method for the optimal design of fuselage panels against buckling. To increase the buckling strength, the fiber paths for each ply of the laminate were used as optimization parameters. It was shown that use of non-conventional laminate lay-up with changing fiber orientations within each ply rather than the use of conventional laminates with straight fibers can lead to increased buckling resistance. Albazzan et al. [19] also proposed a variable stiffness layout for a thin-walled composite cylindrical shell. An optimization study maximizing the buckling load was conducted using lamination parameters. Shojaee et al. [20] compared the buckling performance under the application of planar, longitudinal and ring type stiffeners around the circular cutout on a composite laminate. Longitudinal stiffeners were found to be the most promising amongst all three in terms of resistance against buckling.

1.3. Problem Statement

The structure considered in this study is a thin-walled composite cylindrical shell with a circular cutout in the middle under axial compression loading as shown in Figure 1.1. The primary failure mode of thin-walled structures with cutouts is buckling under axial loadings. The objective of this study is to find optimal reinforcement for the structure to maximize the critical buckling load and to recover the buckling resistance lost due to the introduction of the cutout. The dimensions of the unreinforced cylinder are taken directly from the experimental study conducted by Taheri-Behrooz et al. [12].

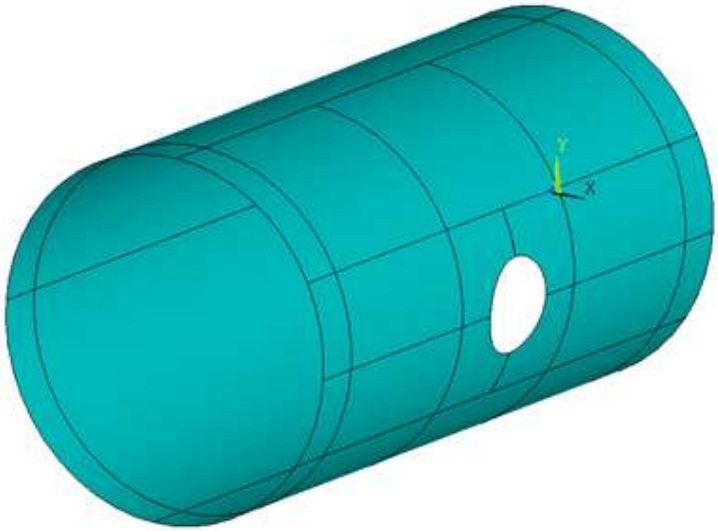

Figure 1.1. Initial unreinforced geometry.

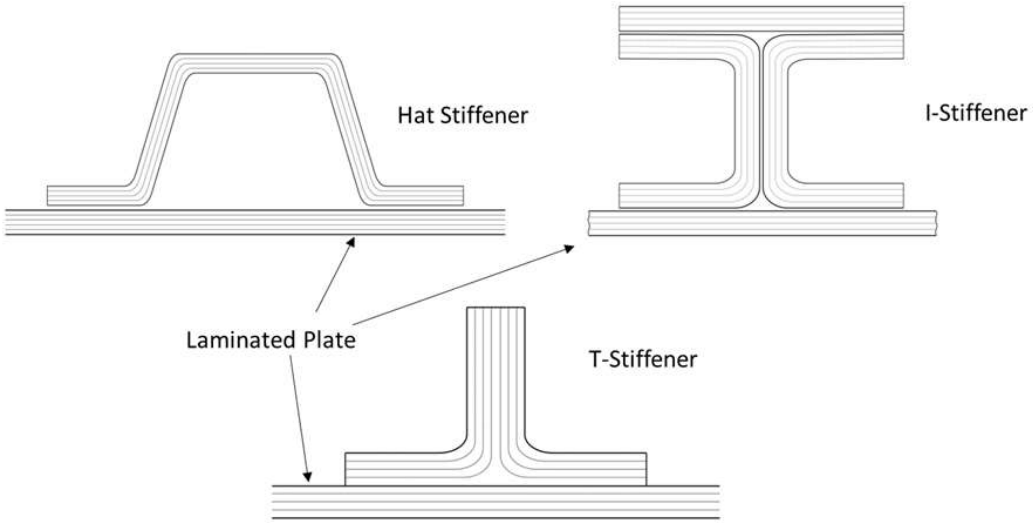

Figure 1.2. Types of stiffener cross-sections.

Different types of stiffener cross-sections are shown in Figure 1.2. Although the most dominant deformation in buckling is in the form of bending, twisting deformations can also be observed. Since closed-section stiffeners like hat-type stiffeners can have

higher torsional stiffness than open-section types such as T-stiffeners or I-stiffeners [1], hat type stiffeners are chosen as the reinforcement method. Figure 1.3 shows the geometric parameters of the stiffeners used where l_{st} denotes the stiffener length, w_c denotes the width of the cap, w_f denotes the width of the flange measured along the circumference of the cylinder, h_{st} denotes the height of the stiffener, the angle between the flange and cap sections of the stiffener is denoted by θ_{st}.

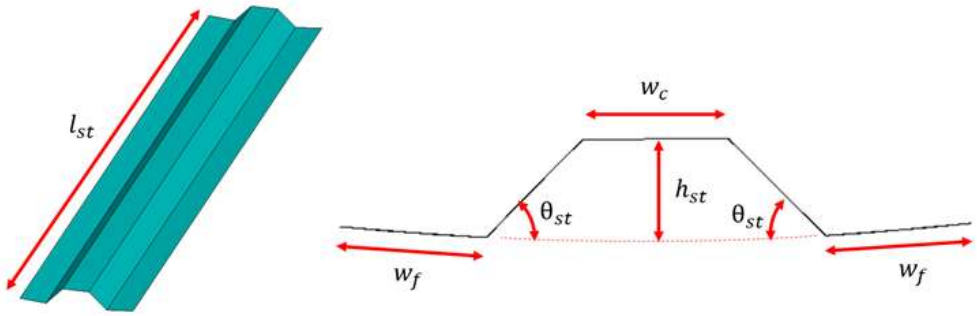

Figure 1.3. Geometric parameters of the stiffener.

Among different configurations, two symmetric stiffeners symmetrically placed at both sides of the cutout are considered. The general stiffener configuration can be seen in Figure 1.4 where d_{st} denotes the distance between the center of the circular cutout and the axis of one stiffener measured along the circumference of the cylinder.

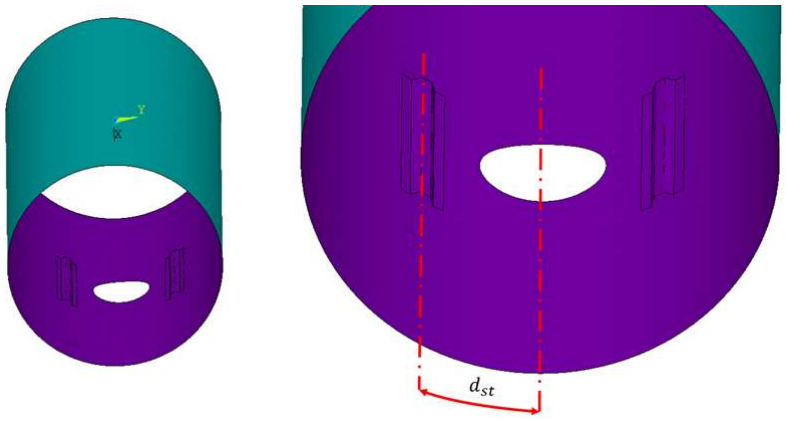

Figure 1.4. Stiffener application around the cutout.

As shown earlier, there is a significant amount of research on the effect of cutouts on a thin-walled panel or a thin-walled cylindrical shell. There are also several studies in the literature about the optimum design of thin-walled cylindrical shell structures, both metallic and composite. However, there is no study in the literature about optimum design of a thin-walled composite circular cylindrical shell with a cutout using a stochastic global optimization method. In contrast to the conventional aerospace applications where longitudinal and circumferential stringers are mostly used, local patch applications and non-conventional stiffener layouts are also proposed in this study.

2. THEORY

2.1. Buckling

Buckling is a phenomenon that occurs when a structure under compressive load starts to lose its stability, therefore having an increased deformation. Slender or thin-walled structures are most prone to buckling. After reaching a critical load, the structure loses its ability to withstand more load and loses its stability, undergoing a large lateral deformation.

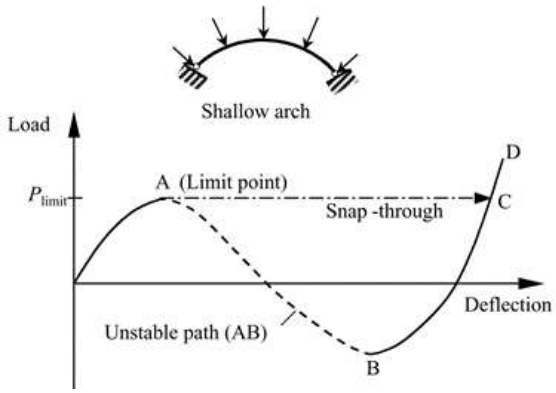

Figure 2.1. Snap-through buckling[21].

There are two main types of buckling: bifurcation buckling and limit load buckling [21]. The deformation path changes suddenly after reaching the critical buckling load in the case of bifurcation buckling. To find the bifurcation buckling load, eigenvalue linear buckling analysis is used. In limit load buckling, no bifurcation is observed; rather, the structure has almost linear load-deflection curve up to the limit buckling load, after which the slope of the load-deflection curve reaches to zero and then decreases. This behavior is called snap-through buckling (See Figure 2.1). Similar behavior can also be observed for shell structures (See Figure 2.2). In order to capture the structural behavior beyond the limit point for these limit load buckling scenarios, nonlinear analyses are required.

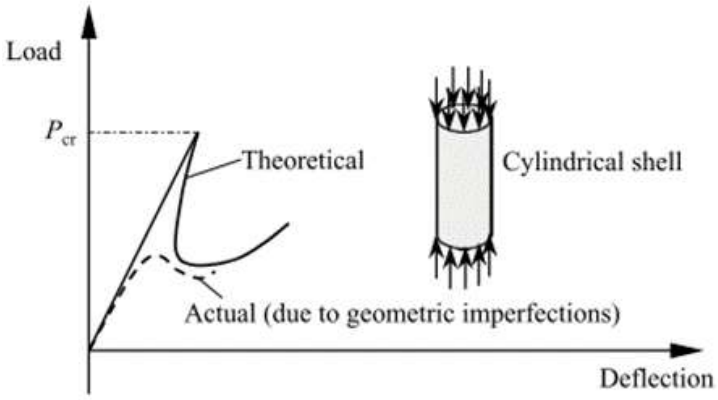

Figure 2.2. Finite-disturbance shell buckling[21].

2.2. Buckling of Thin-Walled Cylindrical Shells

It is of vital importance to check the structural stability of thin-walled cylindrical structures, as they generally work under compressive forces, which might lead to the buckling of the structure. In order to formulate the axial buckling of a circular cylinder under uniform axial compression, principal of virtual work is used [22]. The material of the cylinder is taken to be linearly elastic isotropic homogeneous. A cylinder in a symmetrically buckled form is shown in Figure 2.3.

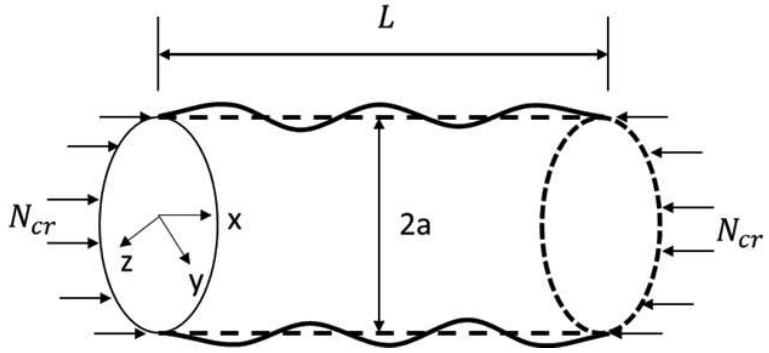

Figure 2.3. A symmetrically buckled cylinder.

The principal of virtual work can be basically expressed as

$$\delta U = \delta W \tag{2.1}$$

where δU denotes the variation of strain energy during a virtual displacement in the structure and δW denotes the variation of virtual work done by the external forces. Therefore, Equation (2.1) states that the total work done on the structure must be zero under virtual displacements.

Assuming that the cylinder is simply supported at both ends, the deflection in the radial direction of the cylinder can be expressed as

$$w = -c_0 \sin \frac{m\pi x}{L} \tag{2.2}$$

where w denotes the radial displacement of the cylinder, c_0 denotes a constant, m denotes the number of half sine waves in the axial direction of the cylinder, x denotes the axial direction of the cylinder, and L denotes the length of the cylinder.

Modeling the cylinder at the midsurface of the cylinder thickness, the axial midsurface strain prior to buckling is expressed as

$$\varepsilon_{x1} = -\frac{N}{Et} \tag{2.3}$$

where N denotes the axial force, E denotes the modulus of elasticity of the material, and t denotes the wall thickness of the cylinder. Using Hooke's Law, the axial and circumferential strains at the midsurface after buckling can be calculated as

$$\varepsilon_{x2} + \nu\varepsilon_{\theta 2} = (1 - \nu^2)\varepsilon_{x1} \tag{2.4}$$

where ε_{x2} and $\varepsilon_{\theta 2}$ denotes the axial and circumferential strains at the midsurface after buckling, and denotes the Poisson's ratio. The circumferential strain can be expressed in terms of the axial strain before buckling as

$$\varepsilon_{\theta 2} = -\nu\varepsilon_{x1} + \frac{c_0}{a} \sin \frac{m\pi x}{L}. \tag{2.5}$$

Inserting Equations (2.3) and (2.5) into Equation (2.4),

$$\varepsilon_{x2} = \varepsilon_{x1} - \nu \frac{c_0}{a} \sin \frac{m\pi x}{L}. \tag{2.6}$$

Using Equations (2.2)-(2.6) with the assumption of axisymmetric deformation, the work done by the external force N is

$$\delta W = 2\pi N \left\{ \nu \int_0^L c_0 \sin \frac{m\pi x}{L}\, dx + \frac{a}{2} \int_0^L \left(c_0 \frac{m\pi}{L} \sin \frac{m\pi x}{L} \right)^2 dx \right\}. \tag{2.7}$$

The virtual work expressed in Equation(2.7) is composed of work due to the change in axial strain ($\varepsilon_{x2} - \varepsilon_{x1}$) and work due to the bending, related deformation of which is expressed in Equation (2.2).

The strain energy due to bending is calculated as

$$U_b = \frac{1}{2} D \iint_A \left\{ (\chi_x + \chi_y)^2 - 2(1-\nu)(\chi_x \chi_y - \chi_{xy}^2) \right\} dx\, dy \tag{2.8}$$

where χ_x and χ_y represents the change of curvature of the cylinder midsurface in x and y directions respectively, χ_{xy} denotes the twist of the cylinder midsurface, A denotes the surface area of the cylinder, and D denotes the flexural rigidity of the cylinder. The flexural rigidity is expressed as

$$D = \frac{Et^3}{12(1-\nu^2)}. \tag{2.9}$$

The strain energy due to membrane deformations is calculated as

$$U_m = \frac{Et}{2(1-\nu^2)} \iint_A \left\{ (\varepsilon_{x0} + \varepsilon_{y0})^2 - 2(1-\nu) \left(\varepsilon_{x0}\varepsilon_{y0} - \frac{1}{4}\gamma_{xy0}^2 \right) \right\} dx\, dy \tag{2.10}$$

where ε_{x0} and ε_{y0} denotes the unit deformation of the midsurface in x and y directions, γ_{xy0} denotes the unit shear of the midsurface.

As the shell deformations are composed of membrane and bending deformations, the strain energy of a deformed shell can be found as

$$U = U_b + U_m. \tag{2.11}$$

Combining Equations (2.8)-(2.11), the change in strain energy is calculated as

$$\delta U = 2\pi N \left\{ \nu \int_0^L c_0 \sin\frac{m\pi x}{L}\, dx + \frac{a}{2}\int_0^L \left(c_0 \frac{m\pi}{L} \sin\frac{m\pi x}{L} \right)^2 dx \right\}. \tag{2.12}$$

The criterion for buckling is that Equation (2.1) must be satisfied. Equating the right-hand-side of Equation (2.7) and Equation (2.12),

$$\left(\frac{\pi E t L}{2a} + \frac{\pi^5 a m^4 D}{2L^3} - \frac{\pi^3 a m^2 N}{2L} \right) c_0^2. \tag{2.13}$$

Since Equation (2.13) must be valid for all c_0 values, the corresponding load N_{cr} can be expressed as

$$N_{cr} = D\left(\frac{m^2\pi^2}{L^2} + \frac{E t L^2}{D a^2 m^2 \pi^2} \right). \tag{2.14}$$

Considering that the mode shape corresponding to the lowest critical load is a half-sine wave, the minimum buckling load of the cylinder is calculated as

$$N_{cr} = \frac{E t^2}{a\sqrt{3(1-\nu^2)}}. \tag{2.15}$$

Therefore, applying an axial load over the load given by Equation (2.14)-(2.15) to a thin-walled cylindrical shell structure results in an unstable equilibrium point for the structure. Any perturbation from this unstable equilibrium point would lead to a larger deformation without any possible turn-back to the equilibrium.

2.3. Newton-Raphson Method vs Arc-Length Method for Buckling Analyses

Thanks to its ability to model and analyze complex solid mechanics problems, finite element method is widely used not only in the industry but also in the academia as well. The primary equation of finite element method for static analyses is as follows:

$$[K]\{U\} = \{F^a\} \tag{2.16}$$

where $[K]$ stands for the stiffness matrix, $\{U\}$ stands for the displacement vector, and $\{F\}$ stands for the vector of the externally applied loads. By discretizing the geometry with meshing, the stiffness matrix is obtained first. Considering that either force or displacement is known for a given degree of freedom as boundary condition, substituting the known values in the force and displacement vectors, the number of unknowns become equal to the number of equations. Then the finite element equations are solved to find all the unknown displacements and the unknown reaction forces.

When large displacements occur, nonlinear effects are included in the model via updating the stiffness matrix at each time increment. This makes the stiffness matrix $[K]$ dependent on the unknown displacement values. Therefore, Equation (2.16) becomes a nonlinear equation. Newton-Raphson method is used to solve nonlinear equations using an iterative procedure. Applying Newton-Raphson method, the nonlinear equations of finite element model can be rearranged as follows [23]:

$$[K^T_{n,i}]\{\Delta u_i\} = \{F^a_n\} - \{F^{nr}_{n,i}\}, \tag{2.17}$$

$$\{u_{i+1}\} = \{u_i\} + \{\Delta u_i\}. \tag{2.18}$$

where $[K^T_{n,i}]$ denotes Jacobian matrix for time step n, $\{F^{nr}_{n,i}\}$ denotes restoring load vector for internal loads for time step n, $\{F^a_n\}$ denotes applied load vector at time step n, i subscript stands for the current equilibrium iteration [24]. Steps for each iteration are as follows:

(i) Assumption of the initial displacement vector $\{u_0\}$,

(ii) Compute the new Jacobian matrix and restoring load vector from configuration,

(iii) Calculate $\{u_i\}$ using Equation (2.17),

(iv) Use Equation (2.18) to find $\{u_{i+1}\}$,

(v) Repeat steps (ii) to (iv) until convergence is achieved.

Let's take the following equation into consideration:

$$[K_i^T]\{\Delta u_i\} = \lambda\{F^a\} - \{F_i^{nr}\} \tag{2.19}$$

where λ denotes the load incrementation coefficient. This coefficient helps to control the load incrementation in the Newton-Raphson method. At each increment, λ is changed by an amount of $\Delta\lambda$ so that

$$\lambda_{i+1} = \lambda_i + \Delta\lambda. \tag{2.20}$$

Given $\Delta\lambda$, the equations are solved iteratively to find Δu. Convergence is achieved when $\{\Delta u_i\}$ is smaller than some reference amount. Figure 2.4 shows the full Newton-Raphson procedure applied on a load-displacement curve.

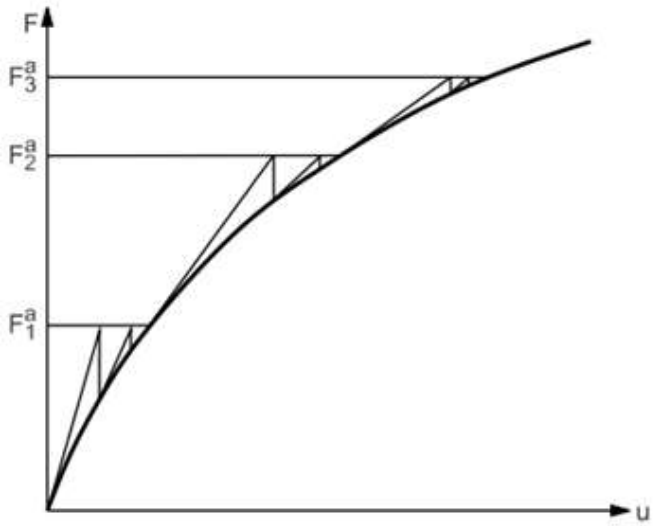

Figure 2.4. Newton-Raphson procedure on load-displacement curve [24].

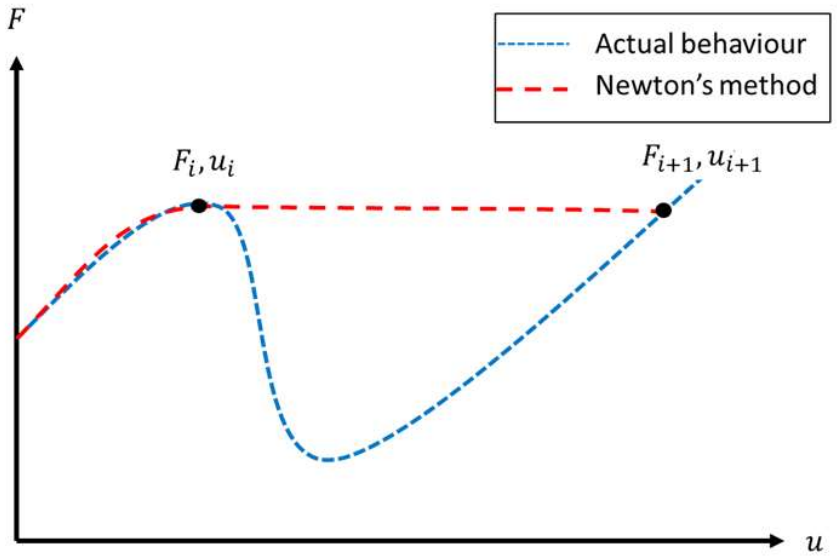

Figure 2.5. Newton-Raphson method vs actual behavior beyond a critical point.

Newton-Raphson method assures convergence in fewer iterations than other iterative methods for solving large non-linear equations. That's why it is widely used in all commercial FEA packages. However, the method fails to converge after the point where Jacobian matrix (tangent stiffness matrix) becomes zero, which is the case for critical points such as critical buckling load [25]. Therefore, Newton-Raphson method cannot capture load-displacement behavior beyond critical points correctly (See Figure 2.5).

There is quite an efficient method for solving complex systems of non-linear equations in the case of existence of a critical point called arc-length method. Originally developed by Eduard Riks [26], arc-length method uses changes not only in displacement (like in Newton-Raphson method) but also the changes in loading. Thus, $\Delta\lambda$ is also an unknown in addition to Δu. Representing internal and external forces as F_{int} and F_{ext}, the equilibrium requires the satisfaction of following equation [25]:

$$F_{int}(u_0 + \Delta u) - (\lambda_0 + \Delta\lambda)F_{ext} = 0. \tag{2.21}$$

In order to satisfy Equation (2.21), additional correction factors for change in displacement and load increments are introduced as δu and $\delta\lambda$. In addition to the equilibrium equation, the arc-length equation

$$(\Delta\mathbf{u}+\delta\mathbf{u})^T\cdot(\Delta\mathbf{u}+\delta\mathbf{u})+\psi^2(\Delta\lambda+\delta\lambda)(\mathbf{F_{ext}^T}\cdot\mathbf{F_{ext}})=\Delta l^2 \tag{2.22}$$

must also be satisfied where the two parameters ψ and Δl are defined by the user. Since the method requires the modification of the equations to be solved due to incremental corrections in Δu and $\Delta\lambda$, this method was found inefficient and inapplicable for finite element applications.

Michael Anthony Crisfield showed an alternative method of solving non-linear equations having critical points [27]. This method is based on not changing the step size or arc-length radius, when equilibrium iterations are being held [24]. The first step is to add load factor to Equation (2.17) as follows:

$$[K_i^T]\{\Delta u_i\}=\lambda\{F^a\}-\{F_i^{nr}\}. \tag{2.23}$$

Then applying incremental form at the substep number n,

$$[K_i^T]\{\Delta u_i\}-\Delta\lambda\{F^a\}=\{\lambda_n+\lambda_i\}\{F^a\}-\{F_i^{nr}\}=-\{R_i\} \tag{2.24}$$

where $\{R_i\}$ denotes the residual force vector in equilibrium iteration i, λ_n denotes the proportional load factor in nth substep, λ_i denotes the proportional load factor in ith equilibrium iteration. Using Equation (2.24), the incremental displacement can be divided into two parts as follows:

$$\{\Delta u_i\}=\Delta\lambda\{\Delta u_i^I\}+\{\Delta u_i^{II}\}, \tag{2.25}$$

$$\{\Delta u_i^I\}=[K_i^T]^{-1}\{F^a\}, \tag{2.26}$$

$$\{\Delta u_i^{II}\}=-[K_i^T]^{-1}\{R_i\}. \tag{2.27}$$

In order to finish an iteration when using arc-length method, Equations (2.26) and (2.27) are solved and then the incremental displacement can be stated as in Equation (2.25). Then a vector connecting the former equilibrium point and the iteration i is defined as

$$t_i=\{\Delta u_n\}+\beta\lambda_i \tag{2.28}$$

where $\{\Delta u_n\}$ denotes the displacement incrementation at the current time step and β denotes the scale vector for unit displacements. For the iteration $i+1$, the same vector is defined as follows:

$$t_{i+1} = \{\Delta u_n\} + \{\Delta u_i\} + \beta(\lambda_i + \Delta\lambda). \tag{2.29}$$

Crisfield's method originally assumes that the norm of the vector connecting a former equilibrium point to the current iteration point is unchanged in an equilibrium iteration [27], which indicates that

$$|t_i| = |t_{i+1}|. \tag{2.30}$$

Combining Equations (2.28), (2.29) and (2.30), the following quadratic formula is obtained:

$$a(\Delta\lambda)^2 + b(\Delta\lambda) + c = 0 \tag{2.31}$$

where the coefficients a, b, and c can be expressed as follows:

$$a = \beta^2 + \{\Delta u_i^I\}^T\{\Delta u_i^I\}, \tag{2.32}$$

$$b = 2(\beta^2\lambda_i + \{\Delta u_n\}^T\{\Delta u_i^I\} + \{\Delta u_i^{II}\}^T\{\Delta u_i^I\}), \tag{2.33}$$

$$c = 2\{\Delta u_n\}^T\{\Delta u_i^{II}\} + \{\Delta u_i^{II}\}^T\{\Delta u_i^{II}\}. \tag{2.34}$$

Using Equations (2.31)-(2.34), the quadratic equation gives two distinct real roots. The angle θ between the vector of the last converged substep and the vector in the current iteration of the current substep can be found using the following equation:

$$\cos(\theta) = \frac{(t_{i+1})^T \cdot (t_{n-1})}{|t_n||t_{n-1}|}. \tag{2.35}$$

Since there are two distinct roots, there are also two vectors that define the direction the equilibrium path will follow. The vector having an angle having cosine closest to 1 is selected as the route using Equation (2.35).

Accordingly, the displacement vectors are updated as follows:

$$\{u_{i+1}\} = \{u_n\} + \{\Delta u_n\} + \{\Delta u_i\}, \tag{2.36}$$

$$\lambda_{i+1} = \lambda_n + \lambda_i + \Delta\lambda. \tag{2.37}$$

To start the method, an initial arc length radius is defined. Taking the initial stiffness matrix as $[K_0^T]$, external load applied as F^a, and an initial load factor as λ_0, the initial arc-length radius can be calculated using Equations (2.38)-(2.40) as follows:

$$t_o = \sqrt{\{u_o\}^T\{u_o\} + \beta^2\lambda^2} \tag{2.38}$$

$$u_0 = [K_0^T]^{-1}\{\lambda_0 F^a\} \tag{2.39}$$

$$\beta = \frac{\sqrt{\{u_0\}^T\{u_0\}}}{\lambda_0}. \tag{2.40}$$

ANSYS APDL software lets the user define a minimum and maximum limit for arc-length radius to obtain a balance between solver time and efficiency.

The arc-length method is represented in Figure 2.6.

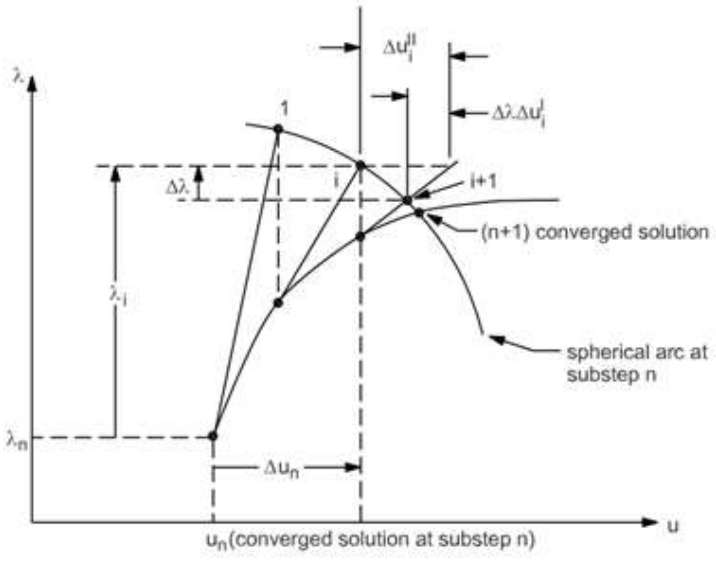

Figure 2.6. Arc-length method representation [24].

2.4. Optimization

Optimization is the method of maximizing or minimizing an output or a quality by finding the best combination of controllable parameters taking the predefined constraints into consideration. Mathematically, it corresponds to maximization or minimization of a function via finding the best combination of the variables of this function.

Structural optimization process has three main elements: Design variables, objective function, and constraints.

Design variables that define the design of the system can be discrete or continuous. Continuous design variables can take any value between their limiting values, whereas discrete design variables can only take values from a predefined list of values. Radius of a hole, ply angle of a laminated composite structure, or elastic modulus of a material used are examples for design variables. The design variables that are changed during an optimization process are called optimization variables.

Objective function, a metric showing how effective a structure is, must be directly or indirectly affected via the design variables [28]. The determination of the function to be minimized/maximized is of vital importance for a better design of the structure. There may be single or multiple objectives to be achieved. In case there are multiple objectives, either the most important one is selected and used in the optimization process or several of them are chosen and combined by assigning weighting coefficients depending on their importance for the optimum design. The more important an objective is, the larger its weighting coefficient should be.

Constraints can basically be defined as the restrictions on the design. In order for a constraint to have a meaning for the design of a structure, it has to be a function of one or several design variables [28]. Constraints can impose upper or lower limits on design variables, in that case they are called inequality constraints, whereas some constraints

require an equation to be satisfied, in that they are called equality constraints.

$$\begin{aligned} &\textit{Minimize } f(x) \\ &\textit{such that } g_j(x) \geq 0, j = 1, ..., a \\ &\qquad\qquad h_k(x) = 0, k = 1, ..., b \end{aligned} \tag{2.41}$$

is the generic formulation of the optimization problem where x denotes the vector of design variables, $f(x)$ denotes the objective function, $g_j(x)$ denotes the inequality constraints, $h_k(x)$ denotes equality constraints.

A point in the design space is called local minimum if the objective function value is smaller than other points in the close neighborhood. On the other hand, in design optimization a point in the design space should be smaller than all other points in the design space, that means it should be global optimum assuming that the objective function is not unbounded.

Although being very capable, the classical optimization methods may sometimes converge to a local optimal solution rather than a global one due to having a monotonic decrease in the objective function value and therefore being dependent on the starting point [29]. This is where global optimization methods, which are mostly stochastic as opposed to the deterministic classical methods, succeed to achieve a global optimum point. In contrast with the classical methods that depend on the starting point, global search algorithms can seek for the global solution within a very broad range of design space thanks to the random generation of points present in the algorithms. Simulated annealing algorithm is one of those stochastic methods.

2.5. Simulated Annealing

First proposed by Kirkpatric et al. [30], the main principle of simulated annealing(SA) is hinged on the physical process of annealing. In material science, annealing is a type of heat treatment where the material is heated up to a specific temperature,

maintained there for some time, and then slowly cooled down to reach a ground state of matter where a highly ordered low energy perfect crystalline is achieved [29]. To reach the lowest-energy state possible, the system is allowed to reach thermal equilibrium at each temperature, where the probability of the system having an energy E is calculated as

$$P(E_{sys} = E) = \frac{1}{Z(T_{sys})} \cdot exp\bigg(- \frac{E}{k_B T_{sys}} \bigg) \tag{2.42}$$

where P denotes the probability function, $Z(T_{sys})$ denotes a normalization factor, E_{sys} denotes the energy of the system, k_B denotes the Boltzmann constant and T_{sys} denotes the temperature of the system. What Equation (2.42) indicates is that, as the temperature is decreased, the average behavior of the system gets to a lower energy state. However, reduction of temperature does not guarantee lowest energy state. Another important aspect is how slow the cooling process takes place. If the cooling is rapid, then crystals with defects may form, which prevents the process to achieve the perfect crystal. Combining all these aspects of physical annealing process and using it as an analogy, Kirkpatric et al. [30] stated that this principal stated in Equation (2.42) can be used to find the global optimum point in an optimization process.

Simulated annealing algorithm starts with a random initial point in the design space, and a predefined initial temperature. Then a new random configuration is generated. Metropolis acceptance criterion is used for a newly created configuration in simulated annealing. According to Metropolis et al. [31], if the newly generated configuration is better than the current configuration, then this new configuration is accepted as the current configuration. If not, then the acceptance of the newly generated point depends on it's an exponential function. The acceptance criterion used can be shown as

$$P_{accept} = \begin{cases} exp\{-\frac{f_n - f_c}{T}\} & \text{if} f_n > f_c \\ 1 & \text{if} f_n \leq f_c \end{cases} \tag{2.43}$$

where P_{accept} denotes the acceptance probability of a newly generated point, f_n denotes the objective function value of the newly generated point, f_c denotes the current point, and T denotes the temperature parameter used. It is important to state that the temperature T in Equation (2.43) does not represent any physical temperature. It is rather a control parameter of the optimization process such that the probability of accepting a worse configuration is reduced as the temperature is reduced. A high enough initial value for the temperature parameter is desired, since high temperature in the beginning means that not only better configurations but also worse configurations are accepted with a high probability. This prevents the algorithm to move in a monotonic way, thereby covering much larger area in the design space.

The number of iterations at each temperature is predefined. So, after defining the initial point at the initial temperature, a specific number of iterations are performed until the temperature is reduced. So, there are two chains in the algorithm. The one occurring at constant temperature is called Markov chain and it has a Markov chain counter parameter that is reset in the beginning of each Markov chain. Once a Markov chain is finished, the temperature is reduced, and the next Markov chain starts. All the successive Markov chains represent the outer loop each with a lower value of the temperature parameter.

As the successive outer loops proceed and the temperature parameter decreases, the acceptance of a worse condition becomes less probable so that only improvements will be accepted right before a predefined stopping criterion is met. This criterion might be a limiting temperature limit at the lower bound, minimum number of improvements in a Markov chain, a minimum limit for the objective function, etc.

Ali et al. [32] has proposed an alternative algorithm called Direct Simulated Annealing (DSA). Unlike SA where the newly generated configuration is compared with the current generation only, DSA adds an additional dimension to the algorithm by adding a memory array A to it. DSA algorithm starts with the generation of N initial points such that $N > n$ where N represents the size of the subset of the points stored,

and n represents the number of optimization variables. The best, the worst and all the points lying in between are stored in the memory. The progress of optimization can easily be controlled and monitored using this set of current configurations. When generating a new configuration, a random configuration in the near vicinity of a randomly chosen current configuration in array A is created. Acceptance criterion is changed such that the objective function of the newly generated configuration is compared with that of the worst configuration such that

$$P_{accept} = \begin{cases} exp\{-\frac{f_n - f_w}{T}\} & \text{if} f_n > f_w \\ 1 & \text{if} f_n \leq f_w \end{cases} \tag{2.44}$$

where f_w denotes the objective function value of the worst configuration. If the newly generated configuration is accepted, the newly generated configuration and its objective function value replaces those of the worst point in the array A. This way, loss of good current solutions at high temperatures in SA is prevented. However, this replacement method has a drawback: Since a new point is created using the current configurations, replacing the worst value leads to the fact that the configurations other than the worst one reach to local minimums, especially when the temperature value is large.

To deal with this drawback of DSA, Akbulut and Sonmez [33] proposed a new variant of simulated annealing called Modified Simulated Annealing(MSA). In MSA, the main difference is the replacement method, such that, the new configuration that is accepted replaces a random configuration in a set of worst configurations. The specific use in the study by Akbulut and Sonmez [33] suggests that the accepted point to replace a configuration randomly chosen from the $(n + 1)$ worst configurations, with the total population of the memory of the algorithm being $9(n + 1)$.

3. METHODOLOGY

The first step of the study is to create a reliable finite element model (FEM) that can simulate the buckling behavior of a thin-walled composite cylinder with a cutout. The experimental work done by Taheri-Behrooz et al. [12] is used both as design starting point and a validation method for the finite element model to be used throughout the study.

A mesh convergence study is conducted to help find a mesh size fine enough to have accurate solutions, but also not too fine to avoid long computational times. The first and second critical buckling loads found by eigenvalue linear buckling analyses are used separately to find a suitable mesh.

Following the mesh convergence study, three different configurations of thin-walled composite cylinders, each with a cutout having a different diameter, used by Taheri-Behrooz et al. [12], are analyzed using the chosen mesh size. Nonlinear analysis using arc-length method with full Newton-Raphson method is used for model validation study. Prior to nonlinear analysis, an eigenvalue linear buckling analysis is done first. Then the displacement results of the first buckling mode found are scaled such that the maximum amount of initial geometric imperfection on the cylinder is 18% of the wall thickness of the cylinder, which is the reference value used by Taheri-Behrooz et al. [12]. Then the initial geometry of the cylinder is updated using these scaled displacement results, which therefore create an initial imperfection around the cutout to initiate the buckling of the structure. The next step is the nonlinear analysis of the structure. Numerical results are compared with the experimental findings.

Upon validating the model, a stiffener configuration is introduced to reinforce the cylinder. A parametric study is conducted to examine the effect of each design variable of the stiffener configuration to the buckling load of the cylinder. According to the results of parametric study, the optimization variables are chosen among the

design variables. Additionally, the upper and lower limits to be used throughout the optimization process for each optimization variable are specified.

Since the aim of this study is to find the optimum design to achieve maximum buckling strength without significant increase in the weight of the reinforced cylinder, the objective function to be minimized is formulated accordingly. Optimization is conducted using Modified Simulated Annealing. The upper and the lower limits found in the parametric study are used in the optimization procedure. If any of the parameters begins to converge to the upper or lower bound during optimization, the bounds of the parameter are extended.

Ansys Mechanical APDL (Ansys Parametric Design Language), a software made by Ansys is used for Finite Element Analysis of structures throughout the study. Model creation, meshing, eigenvalue linear buckling analyses, and nonlinear analyses are done in APDL. Thanks to the parametric nature and the ability to use logic operators such as logical loops, if conditions, and random number generations, parametric studies and the optimization studies are all conducted in Ansys Mechanical APDL (Ansys Parametric Design Language).

4. FE MODEL AND ITS VALIDATION

4.1. Model Details

A finite element model for the buckling behavior of composite cylinders with a cutout is developed. In order to validate the model, the results of the experimental and numerical study conducted by Taheri-Behrooz et al. [12] are used. The accuracy of the results is checked by carrying out a mesh convergence of the same specimen. The geometric parameters of the cylinder specimens used in that study are given in Figure 4.1 and Table 4.1. Since the reinforcement to be optimized are applied on cylinders with cutout, only B50, B80 and B100 cylinder specimens are used in mesh convergence study.

Table 4.1. Geometrical parameters of the samples[12].

Code	Cutout diameter (mm)	Length (mm)	Total thickness(mm)	Inner diameter(mm)	Number of samples
A3	-	700 ± 2	2.1 ± 0.1	378	4
B50	50 ± 1	700 ± 2	2.1 ± 0.1	378	2
B80	80 ± 1	700 ± 2	2.1 ± 0.1	378	2
B100	100 ± 1	700 ± 2	2.1 ± 0.1	378	2

All the cylinders were fabricated using E-glass fiber and Araldite LY 556 epoxy resin hardened with HY917 hardener. The cylinders were fabricated using a stacking sequence of [90/23/-23/-90], where the thickness of each layer was 0.55 mm and the total thickness of the cylinder is 2.2 mm. The mechanical properties of the materials used in that study were obtained from tests according to ASTM D3039 and ASTM D7078. Five specimens were tested. The mechanical properties found according to the test results is given in Table 4.2.

B80 cylinder specimen, one of the three specimens used, is given in Figure 4.2.

Figure 4.1. Cylinder dimensions and lay-up configurations for cylinders with a cutout [12].

Figure 4.2. B80 cylinder specimen [12].

Table 4.2. Mechanical properties of the cylinder specimens[12].

Property	Symbol	Value
Young's modulus in fiber direction	E_x (GPa)	35.5
Young's modulus in matrix directions	E_y (GPa)	5.4
In-plane shear modulus	G_{xy} (GPa)	4.085
Poisson's ratio	ν_{xy}	0.28

4.2. Experimental Loading Conditions

The fixtures used in the experimental setup can be seen in Figure 4.3. The cylinder was clamped between the top clamp part and bottom clamp part. The cylinder was compressed in the axial direction via moving the pushing part in the axial direction of the cylinder. The alignment ball helps the clamped top end of the cylinder slightly rotate with respect to the radial axis of the cylinder so that a uniform load can be applied, which might not be possible without such alignment due to imperfect upper surface of the cylinder specimens. The translation was only permitted in the axial direction. Bottom end of the cylinder, connected to the bottom fixture, was grounded completely. Therefore, all the degrees of freedom of the bottom end of the cylinder were constrained.

4.3. FE Model Details

In order to efficiently represent a thin-walled structure in a finite element model, shell elements are widely used due to their reduced computational requirements compared to solid elements of the same size. The reason for this is the reduced number of equations to be solved when shell elements are used. The shell element called SHELL181 in ANSYS Mechanical is used throughout this whole study.

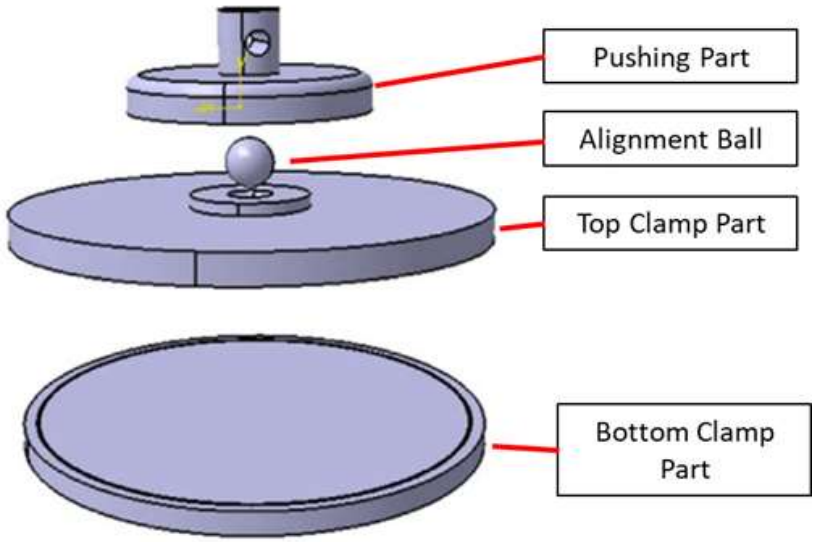

Figure 4.3. Buckling text fixture [12].

SHELL181 is a 4-node structural shell element that gives accurate results for thin-to-moderately thick shell structures thanks to its use of first-order shear deformation theory (Mindlin-Reissner shell theory) [4]. It can also be used for layered applications. Activating the nonlinear geometry option, SHELL181 elements can also calculate the change in shell thickness. As the ANSYS Help suggests, the full integration option is activated for SHELL181 for composite shells. Use of full integration with incompatible modes prevents hourglassing, which is a problem faced when reduced integration and a coarse mesh are used, and helps to capture in-plane bending more accurately thanks to the additional incompatible mode shapes. In addition to full integration at the shell level, the number of section integration points through thickness is five, which is sufficient to capture out-of-plane bending stiffness accurately.

Shell elements are generated in 2D geometries (in 2D or 3D space). Accordingly, the cylinder considered in this study is modeled using 2D geometric entities (areas) as shown in Figure 4.4. Although the general practice is to create the mesh in the mid surface of the thickness, the areas, and accordingly the meshes, are created at the inner radius of the cylinder considering that reinforcements are to be applied on the inner surface of the cylinder.

In general practice, rectangular (quad) elements are favored over triangular elements due to the latter being overly stiff and therefore numerically less accurate. In order to create an all-quad mesh with high quality, the best algorithm is the mapped meshing, which requires areas to be meshed to have four distinct edges. Thus, areas on the cylinder are divided into rectangular curved parts. Partitioning the geometry also helps to add in extra mesh controls to refine the mesh around the cutout in a neater way so that not only a refined mesh around the cutout is obtained but also all quad mesh with the required mesh density around hole and a uniform mesh away from the whole can be achieved.

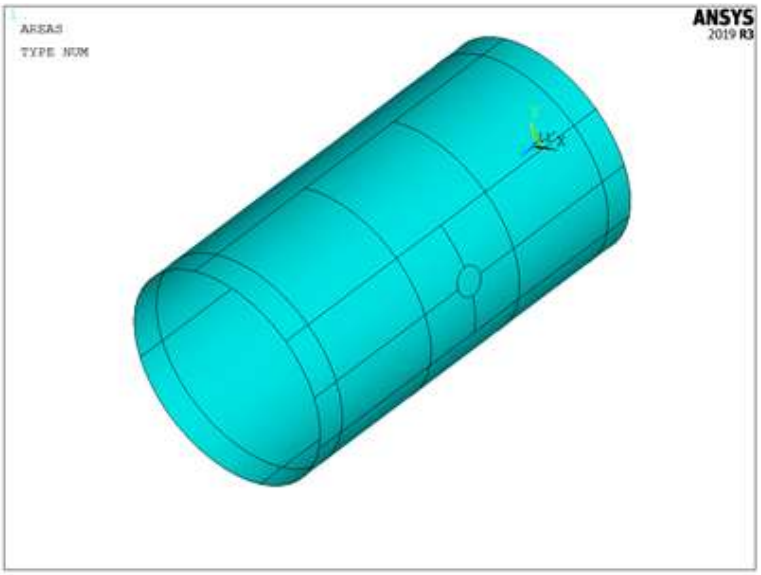

Figure 4.4. Modeled geometry.

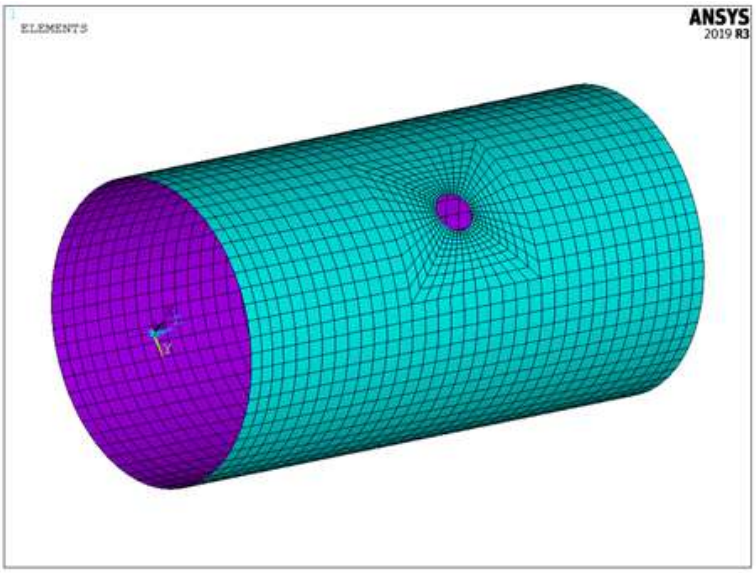

Figure 4.5. Finite element mesh with a mesh size of 20 mm.

An example mesh with a global mesh size of 20 mm can be seen in Figure 4.5. As explained earlier, regions around the cutout are refined to obtain more accurate results at the critical region while maintaining relatively large elements away from the cutout, which strongly reduces the computational time of the analysis. For this purpose, cutout region is separated from other areas by lines created.

The refinement region is 100x100mm around the cutout. The bias factor, which is the ratio of the last element length to the first element length on the selected line, is parameterized such that the first elements around the cutout are perfect squares. Therefore, the elements close to the most important region have an aspect ratio of one, which qualifies these elements as perfect elements with respect to the meshing metrics.

The top end of the cylinder in the experimental setup corresponds to the origin of the coordinate system shown in Figure 4.5, whereas the bottom end of the cylinder corresponds to the opposite side. The boundary conditions are applied to these two ends according to the loading conditions in the experimental setup. For this purpose, all degrees of freedom of the bottom end of the cylinder are constrained. Since the top

end of the cylinder, which is clamped by the top clamp part, cannot move in x and y-axes due to the stiffness of the top clamp part, degrees of freedom of the top end of the cylinder are constrained in x and y axes. Thus, the top end can translate only in the z-axis of the cylinder (See Figure 4.6) during compression. The top end can rotate with respect to the x and y axes, which is related to the alignment ball in the experimental setup. Therefore, during buckling, some parts of the top end may have different displacements in the axial direction. The top end is also free to rotate about z axis.

To apply the axial compressive force to the top of the cylinder, RBE3 elements are used. RBE3 elements are flexible coupling elements that does not add any extra stiffness to the structure and only distribute the load from one master node to the slave node(s) with a weighting factor specified. The master node for RBE3 elements is created at the centroid of the top of the cylinder, whereas the nodes at the top end of the cylinder are selected as slave nodes for RBE3 elements. Then, the master node is connected to the slave nodes. Since the slave nodes are equidistant to the master node at the center, the compressive force is divided to these slave nodes equally. By applying the force to the master node of RBE3 coupling in the axial direction, a load application similar to the experimental setup is achieved. The applied boundary conditions and the load can be seen on Figure 4.6.

Material properties shown in Table 4.2 are used throughout this study. The material is assumed to be linearly elastic orthotropic homogeneous. In order not to overcomplicate the FEM and increase the solution time drastically, composite damage mechanisms are not considered.

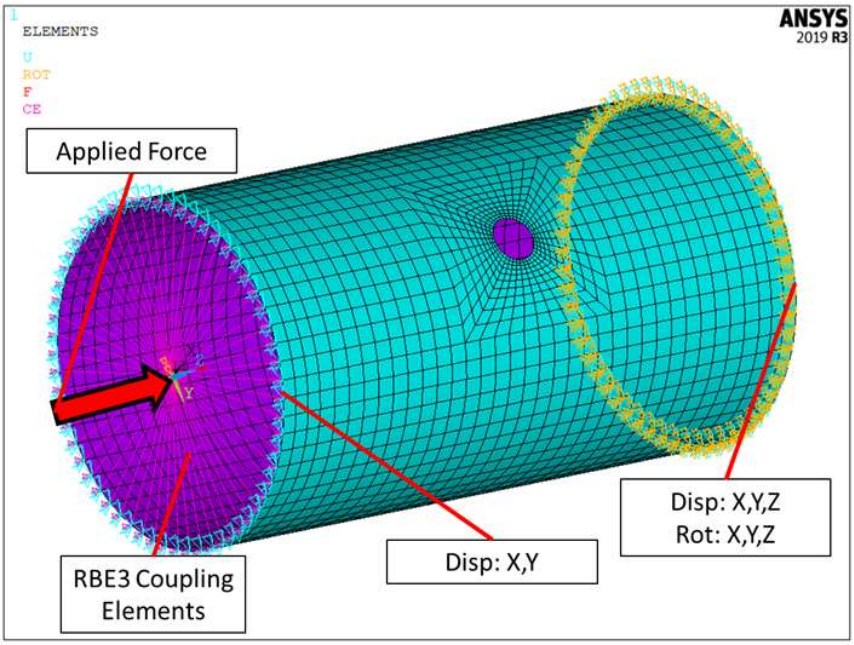

Figure 4.6. Applied load, boundary conditions and RBE3 elements.

4.4. Mesh Convergence Study

The aim of the mesh convergence study is to determine the appropriate mesh size for the analysis to be reliable. Results of linear eigenbuckling analysis are used for the mesh convergence study. The cylinder with the smallest opening is used for mesh convergence study, considering that a smaller opening needs a better mesh resolution compared to a larger cutout to obtain accurate results. Thus, B50 cylinder is chosen for the mesh convergence study. Reducing the mesh size step by step by a constant factor of 1/1.25, percentage difference of the buckling loads for the first and second buckling mode of B50 cylinder are investigated. The reason for using a division factor of 1.25 rather than 2 is to reach a converged mesh at a larger element size, which helps to reduce the computational time during the optimization process greatly. The stop criterion for convergence is assumed to be 0.5% difference in the results.

Mesh details of all the sizes used can be seen in Figure 4.7 and Figure 4.8.

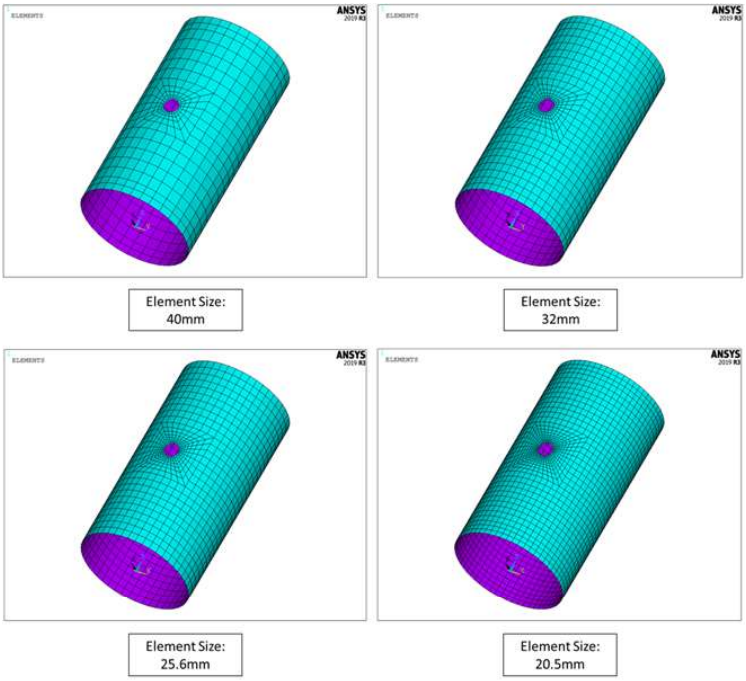

Figure 4.7. Mesh details for mesh convergence - 1.

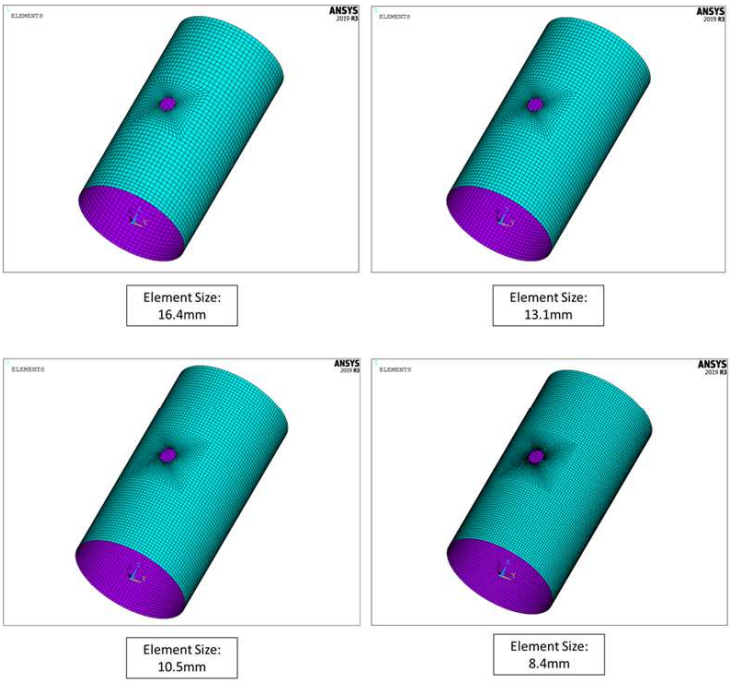

Figure 4.8. Mesh details for mesh convergence - 2.

It can be seen in Figure 4.7 and Figure 4.8 that not only local but also global mesh size is reduced systematically without changing the mesh pattern, which is possible via the use of geometric partitioning shown on Figure 4.4.

Table 4.3. Mesh convergence table for B50 cylinder under linear buckling analysis.

Mesh Size(mm)	1st Buckling Load(kN)	2nd Buckling Load(kN)	1st Percentage Difference	2nd Percentage Difference
40.0	109.90	115.45	-	-
32.0	104.14	108.75	5.24%	5.80%
25.6	101.77	106.10	2.28%	2.43%
20.5	99.18	103.13	2.54%	2.81%
16.4	97.31	100.98	1.88%	2.09%
13.1	96.47	100.03	0.86%	0.94%
10.5	95.76	99.21	0.74%	0.82%
8.4	95.34	98.73	0.44%	0.48%

The results of mesh convergence study are shown on Table 4.3.

At each step, the global mesh size, and accordingly the mesh size around the cutout, is reduced by a factor of 1/1.25 and the percentage difference with respect to the previous step is calculated for each buckling mode. Reducing the global mesh size from 10.5 mm to 8.4 mm results in a change of 0.44% in the 1st buckling load and a change of 48% in the 2nd buckling load. Considering the chosen stop criterion, 10.5 mm is selected as the global element size in the model.

Meyer-Piening et al. [34] proposed that for thin walled cylindrical structures, an appropriate mesh size can be found for FE analysis using the following equation:

$$m = 0.5\sqrt{Rt} \tag{4.1}$$

where R denotes the inner radius of the thin-walled cylinder, t denotes the thickness of the cylinder and m denotes the mesh size. Substituting the parameters of B50 cylinder into Equation (4.1), the mesh size is found to be approximately 10 mm. Combining the mesh convergence study and the suggestion of Meyer-Piening et al. [34], a mesh

size of 10 mm is chosen to be used throughout this whole study.

4.5. Model Validation

To locate the global optimum point accurately using an optimization algorithm, the numerical values used to calculate the objective function should be accurate as well. This is only possible via using a model giving accurate results. Therefore, the finite element model should have as low margin of error as possible to represent the physical event accurately. For this purpose, a more elaborate finite element model than the one used in the mesh convergence study is developed first. Then the numerical results found using this model for each cylinder is compared with the experimental results.

The comparison is made according to the critical buckling loads of different cylinder configurations that are found in the experimental study. The geometrical parameters of the cylinders are given in Table 4.1. The samples of different cylinder configurations are tested under the application of axial compression which is applied true a constant crosshead speed of the upper fixture of 0.01 m/s. As can be seen in Table 4.4, the experimental results consist of the buckling load and the end shortening of tested cylinders.

In order to take the geometric imperfections into account, the method of linear buckling mode-shape imperfections (LBMI) is used. As explained earlier, this method first requires obtaining the eigenbuckle modes and corresponding mode shapes using linear buckling analysis, and then applying one or several of these mode shapes with a scale factor to the geometry. Accordingly, the original geometry is changed to represent the initial imperfection. Since the aim of this study is to optimize the buckling performance, the objective at each step of the optimization is to increase the first buckling mode. Therefore, the mode-shape used to create the geometric imperfection is always the first mode of the current geometry.

Table 4.4. Buckling load and end shortening of tested cylinders[12].

Code	Buckling load(kN)	End-shortening(mm)
A3-1	181.94	3.32
A3-2	183.17	3.40
A3-3	182.36	3.37
A3-4	182.05	3.39
A3 (Average)	182.38	3.38
B50-1	118.38	2.36
B50-2	120.16	2.92
B50 (Average)	119.27	2.64
B100-1	104.10	2.21
B100-2	100.64	2.18
B100 (Average)	102.37	2.21

As explained in the previous chapter, the buckling force is affected by the amount of initial imperfection. The investigation of imperfection sensitivity of the perfect cylinder was held by Taheri-Behrooz et al. [12]. The magnitude of imperfection was defined in terms of the wall thickness of the cylinder. Applying different scale factors multiplied by the wall thickness as the magnitude of imperfection, load-displacement curves were found via use of FEA (See Figure 4.9). The load-displacement curves for cases with a scale factor of above 0.2 did not show any unstable equilibrium point and a snap-back behavior as desired. Examining the cases with scale factors 0.1 and 0.2, the curves had sudden loss of stiffness due to buckling. In the end, researchers decided to use a scale factor of 0.18. Based on the findings of that study, in the present study the maximum amount of imperfection on the cylinder due to the first buckling mode is set to an amount of $\delta = 0.18t$, where δ denotes the maximum amount of imperfection, and t denotes the wall thickness of the cylinder.

The resultant displacement and the radial displacement corresponding to the first buckling mode found from linear buckling analysis are shown in Figure 4.10 and Figure 4.11 respectively.

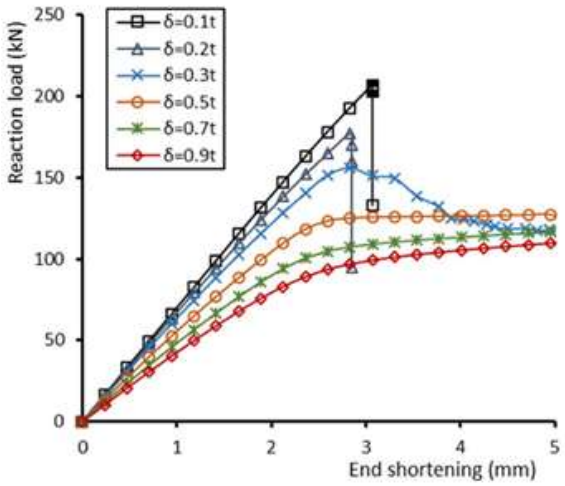

Figure 4.9. Load-displacement curves for different amounts of imperfections[12].

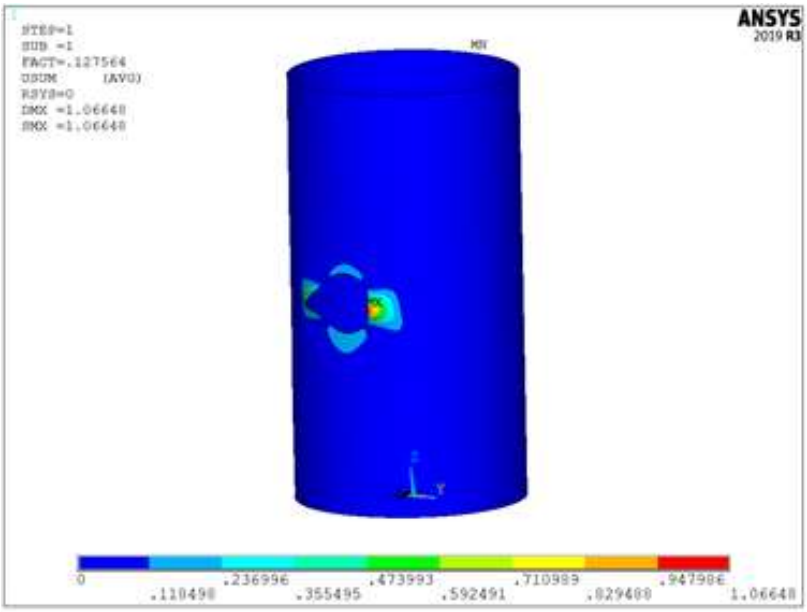

Figure 4.10. Resultant displacement of first buckling mode shape of B100 cylinder.

Updating the original geometry with the displacement from the first buckling mode, an imperfection around cutout is obtained. The original geometry and the updated geometry around cutout can be seen in Figure 4.12. In order to make the imperfection visible, an imperfection amount ten times the one used in FEA is shown in Figure 4.12.

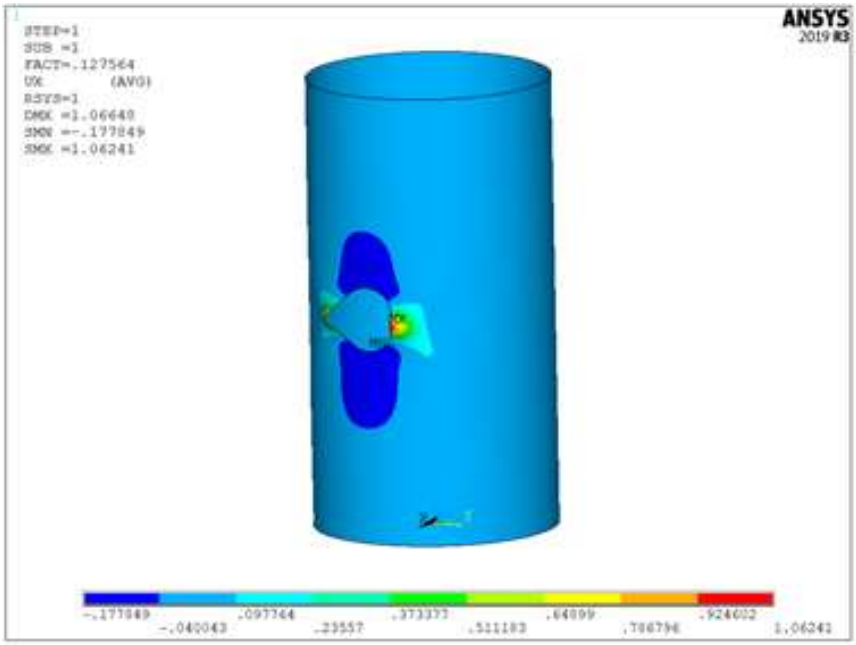

Figure 4.11. Radial displacement of first buckling mode-shape of B100 cylinder.

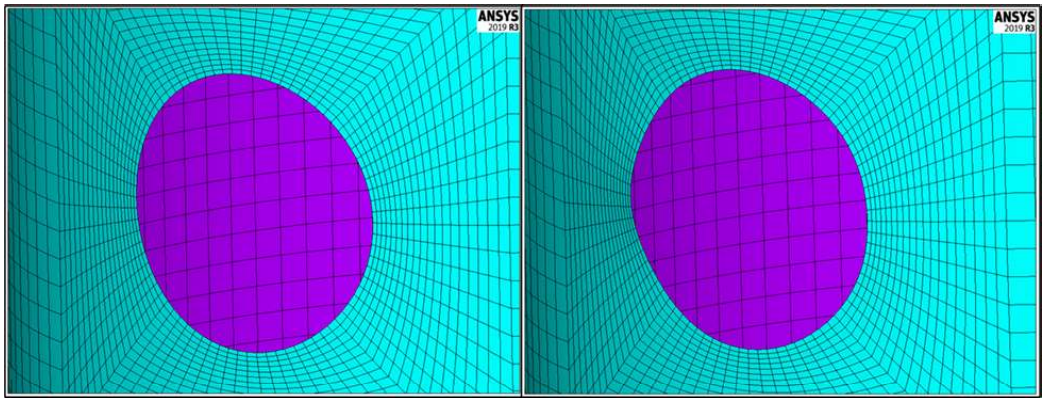

Figure 4.12. The original geometry (left) and the updated geometry (right) of the cutout.

Since Newton-Raphson method, a very efficient method to solve non-linear equation systems, falls short capturing the unstable equilibrium of buckling, arc-length method is used to find the unstable equilibrium point. Thus, the steps of the finite element analysis used for model validation, parametric studies and the optimization study are as follows:

(i) Static analysis with compressive force and boundary conditions is carried out to obtain the prestress effects, which represents the changes in the stress stiffness matrix. This step is necessary prior to a linear buckling analysis.

(ii) Using the prestress effects, linear buckling analysis is carried out to obtain the mode-shape of the first buckling mode.

(iii) A displacement field with the maximum resultant displacement of the first buckling mode scaled to $0.18t$ is applied to the initial geometry to create the imperfection.

(iv) Non-linear static analysis is carried out via the use of arc-length method, which gives the critical load at which the structure starts buckling.

The results of the model validation study can be seen in Table 4.5. Considering the percentage differences being about 5%, which is an acceptable error margin, the finite element model and the analysis method are found to be reliable. Considering that the maximum of buckling load was lost for B100 cylinder according to the experimental data by Taheri-Behrooz [12], B100 cylinder is chosen as the configuration to be optimally reinforced.

Table 4.5. The results of the model validation study.

Type of Cylinder	Buckling Load (kN) in FEA	Experimental Buckling Load (kN)	Percentage Difference
B50	113.051	119.27	5.21%
B80	97.227	102.37	5.02%
B100	96.187	91.49	5.13%

4.6. Stiffener Application and Contact Modeling

As explained earlier, a symmetric stiffener configuration around cutout is proposed. In order to have the same mesh pattern and mesh density for the cylinder through the whole study, stiffener geometries are modeled separately as can be seen in Figure 4.13.

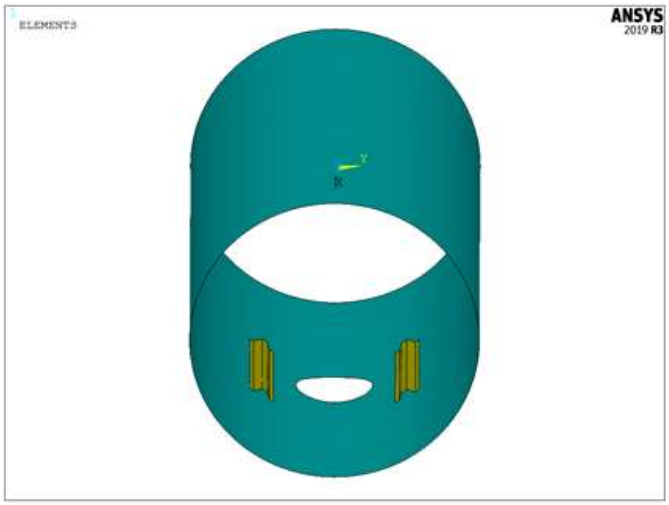

Figure 4.13. B100 cylinder with stiffeners applied.

The mesh details of the stiffened cylinder can be seen in Figure 4.14. SHELL181 elements are used with full integration option enabled. A denser mesh is used only in the middle part, a segment of 100 mm. This not only improves the accuracy of the analysis close to cutout where the maximum deflection is expected according to the results of linear buckling analyses (See Figure 4.10 and Figure 4.11), but also reduces the solution time by decreasing the number of the nodes used in the model. Improvements in the solution time becomes much apparent as the size of the stiffener (especially the length) is increased.

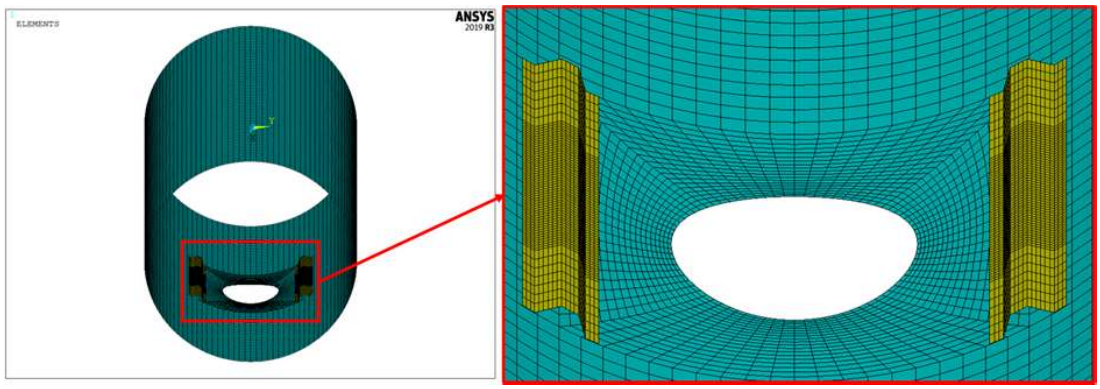

Figure 4.14. Mesh details of stiffened cylinder.

The contact between stiffeners and the cylinder is modeled using surface-to-surface contact elements of ANSYS Mechanical, namely CONTA174 and TARGE170 elements. These elements can accurately represent the contact between two flexible bodies. Since this is an optimization-based study, delamination between the internal layers of laminates and between stiffeners and the cylinder is not modeled in order not to overcomplicate the model and increase the solution time of each simulation. Contact behavior is defined as bonded-always, which means the contacting surfaces neither separate nor move transversely against each other. So, friction is not modeled as well. Multipoint constraint (MPC) algorithm is used with coupling constraint option. It means that the nodes in contact during analysis are constrained to have the same displacement solutions. Therefore, the contact becomes flexible and deformable.

5. OPTIMIZATION PROCEDURE

Modified Simulated Annealing (MSA) is used to find the optimum design of stiffeners in this study. To reinforce stiffeners against buckling while providing a lightweight application, an objective function to be formulated is formulated as

$$f_{objective} = w_{mass}\left(\frac{m_{re}}{m_{ur}}\right) + w_{load}\left(\frac{F_{ur}}{F_{re}}\right) \tag{5.1}$$

where $f_{objective}$ denotes the objective function used during optimization, w_{mass} denotes the weighting coefficient for mass ratio, w_{load} denotes the weighting coefficient for load ratio, m_{re} denotes the mass of the reinforced cylinder, m_{ur} denotes the mass of the unreinforced reference cylinder, F_{re} denotes the critical buckling load of the reinforced cylinder, and F_{ur} denotes the critical buckling load of the unreinforced reference cylinder. Because decrease in m_{re} and increase in F_{re} lead to decrease in the objective function, $f_{objective}$, minimization of the objective function achieves the goal of obtaining a design having highest resistance to buckling with minimum use of material. By choosing different values for the weighting coefficients, one may bias either buckling resistance or low weight.

Initially, only the geometric parameters of the stiffeners are optimized: l_{st}, h_{st}, θ_{st}, w_c and w_f. Therefore,

$$n = 5 \tag{5.2}$$

where n denotes the number of optimization parameters used in the first step of the optimization.

Random configurations are created by randomly changing the values of these five optimization parameters. To explain the working principle of the algorithm, the equations regarding the generation of a new configuration, the decrement of parameters and other equations including the optimization parameters are given in terms of the

stiffener length. A new random value for the stiffener length of a new configuration is generated as

$$l_{st,n} = l_{st,c} + r_{rand}\Delta l_{st} \tag{5.3}$$

where $l_{st,n}$ denotes the stiffener length of the newly generated configuration, $l_{st,c}$ denotes the stiffener length of the current configuration, r_{rand} denotes a random number between -1 and 1, and Δl_{st} denotes the maximum variation in the length of the stiffener. The initial maximum variation in the stiffener length is taken as

$$\Delta l_{st} = \left(\frac{l_{st,max} - l_{st,min}}{3} \right) \tag{5.4}$$

where $l_{st,max}$ and $l_{st,min}$ denote the upper and the lower bound for the stiffener length. The variation of stiffener length given as Δl_{st} in Equation (5.4) represents the initial value of variation. As the optimization progress, this variation is decreased gradually.

The optimization starts with a random generation of the initial configuration set. The number of configurations in the set is equal to N_{set}, which is calculated as

$$N_{set} = 9n \tag{5.5}$$

where n denotes the number of optimization parameters. Combining equations 5.2 and 5.5, a set of 45 configurations are randomly generated first. Then the objective function value for each configuration is calculated using Equation (5.1). The configurations are ordered from the best to the worst, the best having the smallest objective function value and the worst having the largest objective function value. The order of the best configuration is 1.0 and the order of the worst configuration is N_{set}. The "worse" configuration is the one with the order number $(N_{set} - 2n)$, whereas the "worst-best" configuration is the one with the order number $(N_{set} - 2n + 1)$.

After creating a set of configurations having a size N_{set}, a new configuration is generated using a random configuration selected amongst the current set at each iteration. Then a new configuration is created using Equations (5.3) and (5.4). After

generating a new configuration, its objective function value is calculated. The acceptance probability of the newly generated configuration is calculated as

$$P_{accept} = \begin{cases} exp\{-\frac{f_n - f_{wb}}{T}\} & \text{if} f_n > f_{wb} \\ 1 & \text{if} f_n \leq f_{wb} \end{cases} \tag{5.6}$$

where f_n denotes the objective function value of the new configuration, f_{wb} denotes the objective function value of the worst-best configuration. According to Equation (5.6), if the new configuration is better than the worst-best configuration, it is accepted directly. If the new configuration is worse than the worst-best configuration, then the corresponding value for the exponential function defined in Equation (5.6) is calculated and compared with a random number generated between 0.0 and 1.0. If the exponential calculated is larger than a random number generated between 0.0 and 1.0, the new configuration is accepted. Else, the new configuration is rejected. If the new configuration is better than the best configuration, the new one is accepted directly, and the current Markov chain is finished. All the new configurations better than worse configuration are considered as improvement.

When a new configuration is accepted, it replaces a configuration randomly chosen from the 2n worst configurations, with the total population of the current configuration being 9n. After each acceptance and replacement, the set is ordered from the best to the worst.

The minimum length of each Markov chain is defined as

$$L_m = 3n. \tag{5.7}$$

Equation (5.7) states that, there are at least $3n$ number of iterations in each Markov chain unless a configuration better than the best configuration in the current set is generated. Optimization starts with a Markov chain length of $3L_m$. The length of a Markov chain is decreased when the number of improvements in the last Markov chain is less than 10% of the maximum Markov chain length. In such a case, the

current Markov chain length is reduced as

$$L_{m,c} = nint\left(L_m\left(1 + 2\left(\frac{\Delta l_{st,c}}{\Delta l_{st,i}}\right)\right)\right) \tag{5.8}$$

where $L_{m,c}$ denotes the current maximum Markov chain length, L_m denotes the initial maximum Markov chain length that is defined in Equation (5.7), $\Delta l_{st,c}$ denotes the current maximum variation of the length parameter and $\Delta l_{st,i}$ is its initial value. If the number of improvements in the worst-best configuration is less than 10% of the total number of iterations in a Markov chain, the maximum variation of the optimization parameters is decreased by 10% and the new maximum value of variation for each parameter is calculated as

$$\Delta l_{st,n} = 0.9(\Delta l_{st,c}). \tag{5.9}$$

Considering a reduced variation in parameters, the Markov chain length is reduced as well using Equation (5.8).

As explained in Section 2.5, the optimization algorithm consists of two loops: the inner loop and the outer loop. The iterations carried out in the inner loop called Markov chain are carried out at a constant value of the temperature parameter. After the completion of each Markov chain, the temperature parameter is decreased, resulting in decreased probability of acceptance of a configuration worse than the worst-best configuration is decreased as well. The only exception where the temperature parameter is not decreased after finishing a Markov chain is when a new configuration better than the current best configuration is found. The amount of decrement of the temperature parameter depends on the ratio of acceptance and the ratio of step size, which are defined as

$$R_{step} = \frac{\Delta l_{st,c}}{\Delta l_{st,i}} + 0.01 \tag{5.10}$$

$$R_{acc} = \frac{m_{acc}}{m_{it}} \tag{5.11}$$

where m_{acc} denotes the number of accepted configurations and m_{it} denotes the number of iterations carried out in the current Markov chain. The decrement of temperature is controlled with a constant that is defined as

$$\alpha = \begin{cases} 0.9 & \text{if } R_{acc} > R_{step} \\ 0.9999 & \text{if } R_{acc} \leq R_{step} \end{cases} \tag{5.12}$$

where R_{acc} denotes the ratio of acceptance and R_{step} denotes the ratio of the current step size. Equations (5.10)-(5.12) regulate the decrement of temperature after each Markov chain, and the new temperature is calculated as

$$T_n = \alpha T_c \tag{5.13}$$

where T_n and T_c denote the new and the current values for temperature parameter. The initial value for the temperature parameter is chosen to be 20. The initial value of the temperature parameter is determined such that almost all the randomly generated configurations are accepted regardless of the objective function value during the initial phases of the optimization, whereas the amount of time spent for the whole optimization process is minimized as much as possible. In order to decrease the temperature parameter slowly in the beginning, an amount of 0.01 is added to the definition of R_{step} as shown in Equation (5.10). Thus, a larger amount of α is used in the beginning.

The optimization is finished when the initial temperature becomes less than $(1e-05)$ and the difference between the objective function values of worse and the best configuration is less than 0.0005.

6. PARAMETRIC STUDY

Having an initial geometric design with no predefined upper and lower limits for the optimization parameters extremely widens the design space and makes it quite difficult to reach an optimum design efficiently. To perform optimization efficiently in a reasonable time, defining proper upper and lower bounds for the optimization variables is essential.

Before starting the design of a system with the assumption of having an initial geometric design, it is a common practice to conduct a parameter analysis/parametric study. Upon specifying physical and/or geometric parameters affecting the performance of the design, the effect of each parameter on the performance of the whole design should be investigated individually. In a one-factor-at-a-time parametric study, the parameter to be investigated is varied, while holding the other parameters constant.

Even though the main application of reinforcements to be investigated and optimized is chosen to be stiffeners, increasing the thickness of the cylinder locally around the cutout by using a local patch application is considered in the first place. For this purpose, a local patch is applied around the cutout and the effect of the design parameters of the patch on the buckling load of the reinforced structure is investigated prior to the parametric study of the stiffeners. After that, a parametric study is carried out for stiffeners around the cutout.

The geometric parameters of the stiffeners are shown in Figure 1.3. The other parameters are the thickness and fiber orientations of the stiffener and its distance from the hole. The parametric study should be repeated for at least two different configurations to observe the effect of varying parameters for different configurations.

To find reasonable upper and lower bounds for the optimization parameters, a parametric study is carried out. The effect of each optimization parameter is investi-

gated using three different configurations. The critical buckling load and corresponding objective function values are taken as measures of performance for the reinforced cylinder.

For the parametric studies of the stiffeners, the effect of the geometric properties of the stiffeners shown in Figure 1.3 are investigated only, while keeping the distance to hole center, the fiber orientations, and the total thickness of the stiffener constant. These constant parameters are 100 mm, [90°/23°/-23°/-90°] and 0.55 mm, respectively.

6.1. Parametric Study for the Patch Application

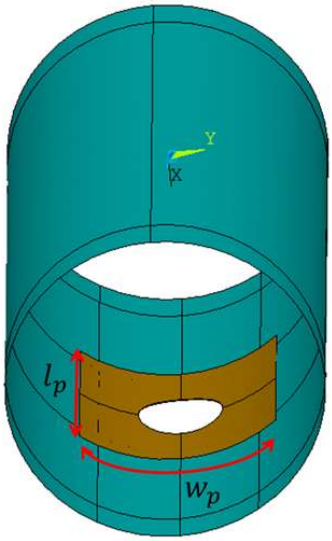

Figure 6.1. The geometric parameters of the patch application.

As can be seen in Figure 6.1, the patch is applied symmetrically around the cutout. The length of the patch, l_p, is defined along the axial direction of the cylinder, while the width of the patch, w_p, is measured along the circumference of the cylinder. Square patch application is considered in this study. Therefore, l_p and w_p are taken to be equal. Beside the dimensions, the thickness of the patch and the ply orientations of the layers are also varied during the parametric studies. The patches are taken to be

made of four layers, having fiber orientations symmetrically used as $[\theta_1/\theta_2/-\theta_2/-\theta_1]$, where θ_1 denotes the outer layer fiber orientation angle and θ_2 denotes the inner layer fiber orientation angle.

6.1.1. The effect of the size of the patch

The configurations of the patches used for the parametric study of the size of the patch are shown in Table 6.1.

Table 6.1. Patch configurations used in the parametric study of the size of the patch.

Patch Number	Ply angles for patch layers (deg)	Thickness (mm)	Size of the patch (mm x mm)
1	90/23/-23/-90	0.55	150 x 150-400 x 400
2	90/45/-45/-90	1.1	150 x 150-400 x 400
3	30/60/-60/-30	2.2	150 x 150-400 x 400

As can be seen in Table 6.1, the parametric study is conducted for values of one side of the patch varying from 150 mm to 400 mm with intervals of 50 mm. The resulting buckling loads and objective function values of the parametric study for the size of the patch are shown in Figure 6.2 and Figure 6.3, respectively.

As seen in Figure 6.2 and Figure 6.3, increasing the patch size results in an increase in the critical buckling load of the structure. This increasing trend is up to a size of 250 mm x 250 mm or 300 mm x 300 mm, depending on the configuration, beyond which only marginal gains are observed. Additionally, the increase in the weight becomes more effective in the objective function as the improvements in the buckling load becomes marginal. This leads to increases in the objective function value.

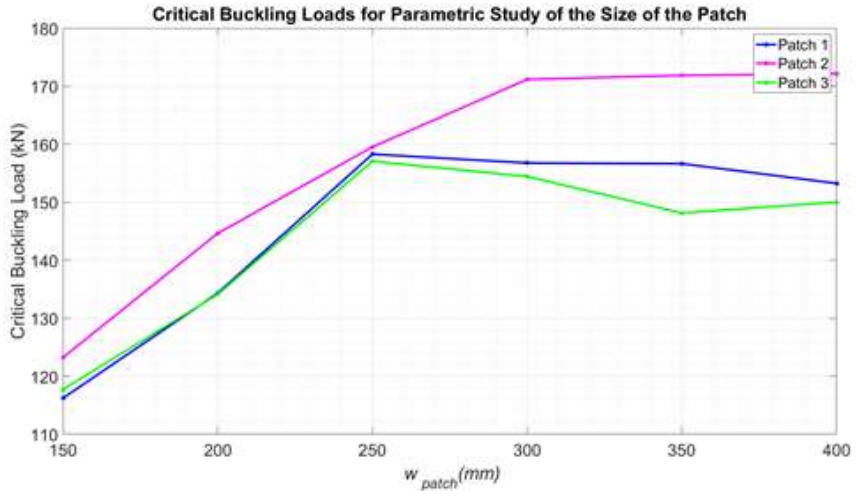

Figure 6.2. Critical buckling load vs. the size of the patch.

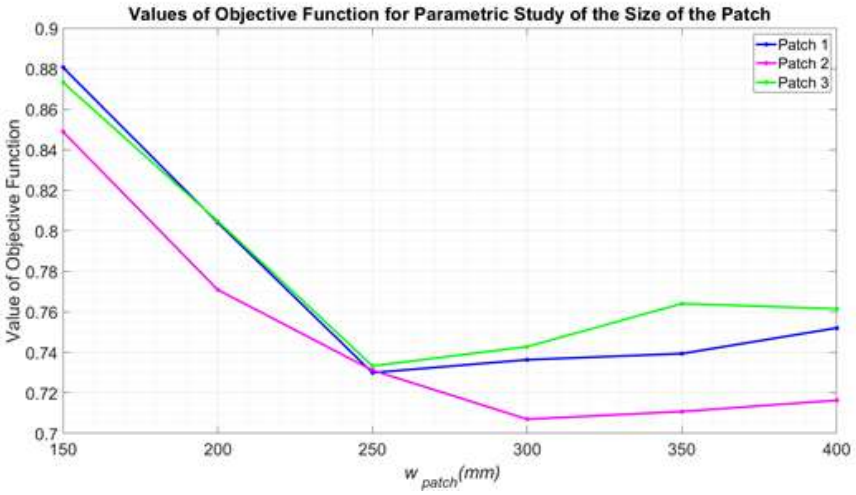

Figure 6.3. Objective function value vs. the size of the patch.

6.1.2. The effect of the thickness of the patch

The patch configurations used in the parametric study of the thickness of the patch are shown in Table 6.2.

Table 6.2. Patch configurations used for the parametric study of the thickness of the patch.

Patch Number	Ply angles for patch layers (deg)	Thickness (mm)	Size of the patch (mm x mm)
4	90/23/-23/-90	0.55-3.3	150 x 150
5	90/60/-60/-90	0.55-3.3	300 x 300
6	90/45/-45/-90	0.55-3.3	400 x 400

As can be seen in Table 6.2, the parametric study is conducted for values of the thickness of the patch varying from 0.55 mm to 3.3 mm with intervals of 0.275 mm. The resulting buckling loads and objective function values of the parametric study for the thickness of the patch are shown in Figure 6.4 and Figure 6.5, respectively.

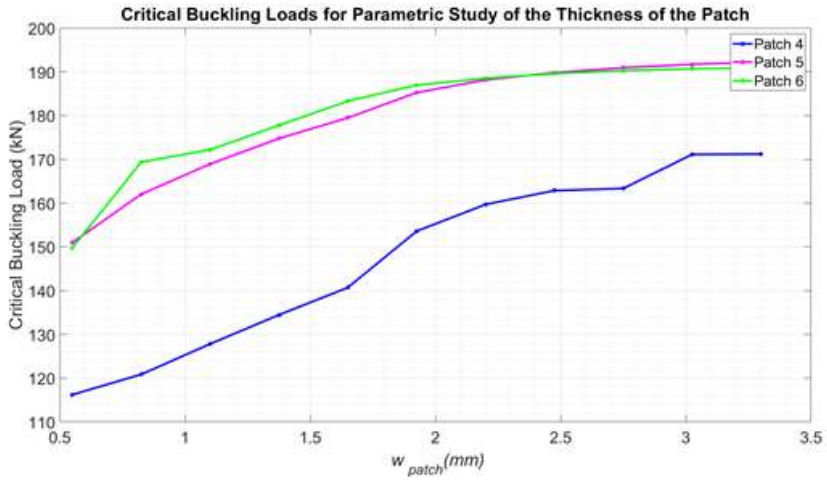

Figure 6.4. Critical buckling load vs. the thickness of the patch.

As can be observed in Figure 6.4 and Figure 6.5, increasing the patch thickness results in an increase in the critical buckling load of the structure. However, as the thickness is increased, the amount of improvement in buckling load decreases. Furthermore, the increase in the weight becomes more effective than the gains in the buckling load as the thickness increases. Consequently, the objective function value starts to increase when thickness is increased beyond a certain value.

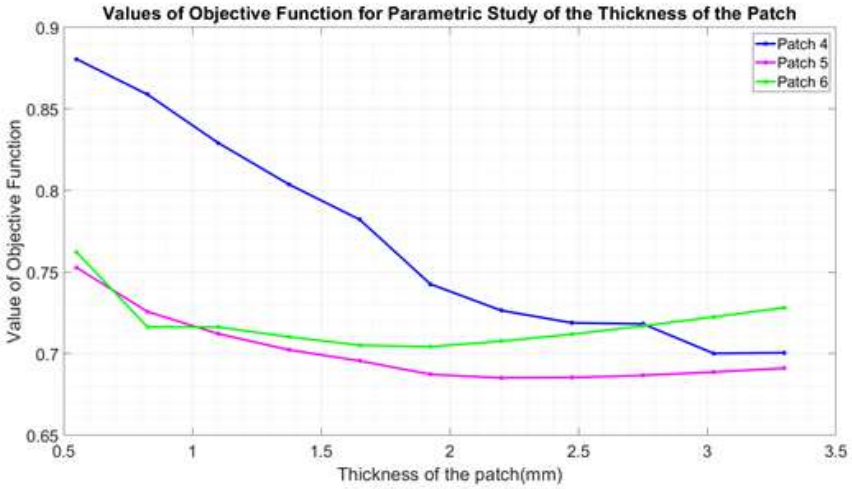

Figure 6.5. Objective function value vs. the thickness of the patch.

6.1.3. The effect of the outer layer fiber orientation

The patch configurations used in the parametric study of the outer layer fiber orientation of the patch are shown in Table 6.3.

Table 6.3. Patch configurations used in the parametric study of the outer layer fiber orientation of the patch.

Patch Number	Outer layer fiber orientation (deg)	Inner layer fiber orientation (deg)	Thickness (mm)	Size of the patch (mm x mm)
7	0-90	23	0.55	250 x 250
8	0-90	23	2.2	350 x 350
9	0-90	60	1.1	350 x 350

As can be seen in Table 6.3, the parametric study is conducted for values of the outer layer fiber orientation of the patch varying from 0° to 90° mm with intervals of 10°. The resulting buckling loads and objective function values for the outer layer fiber orientation of the patch, θ_1, are shown in Figure 6.6 and Figure 6.7, respectively.

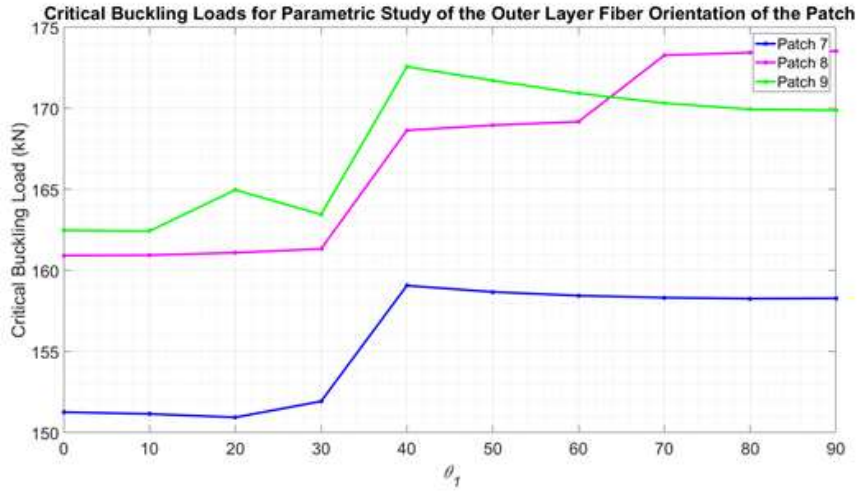

Figure 6.6. Critical buckling load vs. the outer layer fiber orientation of the patch.

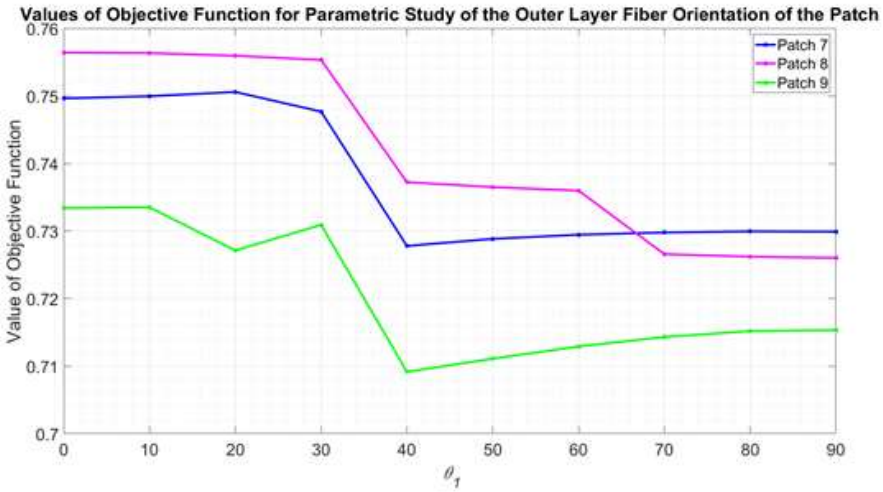

Figure 6.7. Objective function value vs. the outer layer fiber orientation of the patch.

As seen in Figure 6.6 and Figure 6.7, increasing the fiber orientation angle of the outer layers leads to an increase in the buckling load of the reinforced cylinder. However, patches 7 and 9 show a slightly different trend, where the maximum buckling load is reached at around 40° and the load decreases slightly up to 90°. This indicates that the effect of the layer orientation angle of the outer layers on the critical buckling cannot be simply explained, and it is rather dependent on the other parameters.

6.1.4. The effect of the inner layer fiber orientation

The patches used for the parametric study of the inner layer fiber orientation of the patch are shown in Table 6.4.

Table 6.4. Patches used for the parametric study of the inner layer fiber orientation of the patch.

Patch Number	Inner layer fiber orientation (deg)	Inner layer fiber orientation (deg)	Thickness (mm)	Size of the patch (mm x mm)
10	0-90	90	0.55	250 x 250
11	0-90	90	2.2	350 x 350
12	0-90	90	1.1	350 x 350

As can be seen in Table 6.4, the parametric study is conducted for values of the inner layer fiber orientation of the patch varying from 0° to 90° with intervals of 10°. The resulting buckling loads and objective function values for the inner layer fiber orientation of the patch, θ_2, are shown in Figure 6.8 and Figure 6.9, respectively.

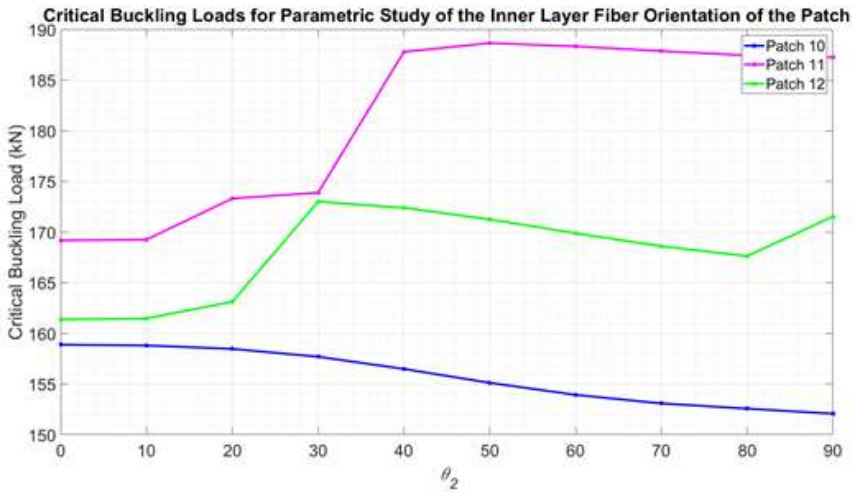

Figure 6.8. Critical buckling load vs. the inner layer fiber orientation of the patch.

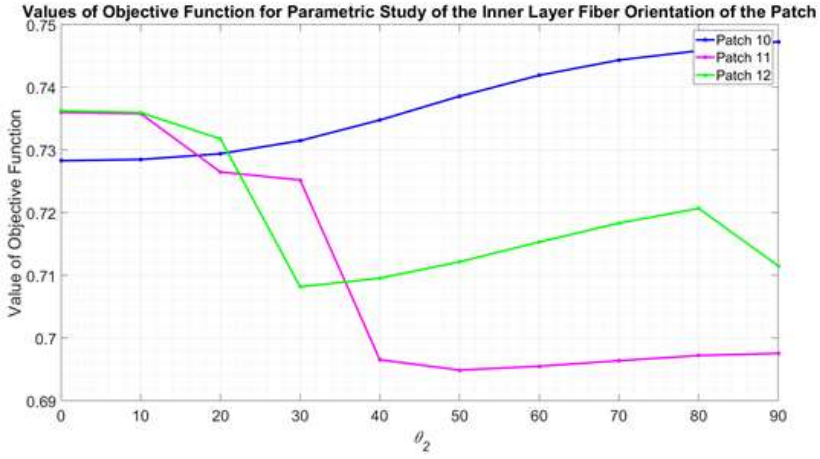

Figure 6.9. Objective function value vs. the inner layer fiber orientation of the patch.

As Figure 6.8 and Figure 6.9 indicate, increasing the fiber orientation angle of the inner layers leads to a decrease in the buckling load of the reinforced cylinder for patches 11 and 12, whereas the opposite trend is observed for patch 10. Therefore, the effect of the orientation angle of the inner layers on the critical buckling load depends on the values of the other parameters.

6.2. Parametric Study for the Stiffener Application

6.2.1. The effect of width of the cap of the stiffener

The configurations used for the parametric study of w_c are shown in Table 6.5.

Table 6.5. Configurations used for the parametric study of width of the cap of the stiffener.

Configuration Number	Ply angles for stiffener(deg)	l_{st} (mm)	h_{st} (mm)	θ_{st} (deg)	w_c (mm)	w_f (mm)	d_{st} (mm)
1	90/23/-23/-90	120	4	45	3-18	4	100
2	90/23/-23/-90	160	4	60	3-18	6	100
3	90/23/-23/-90	240	5	30	3-18	8	100

As can be seen on Table 6.5, the parametric study is conducted for values of w_c varying from 3 mm to 18 mm with intervals of 1 mm. The resulting buckling loads and objective function values of the parametric study for the width of the cap of the stiffener are shown in Figure 6.10 and Figure 6.11, respectively.

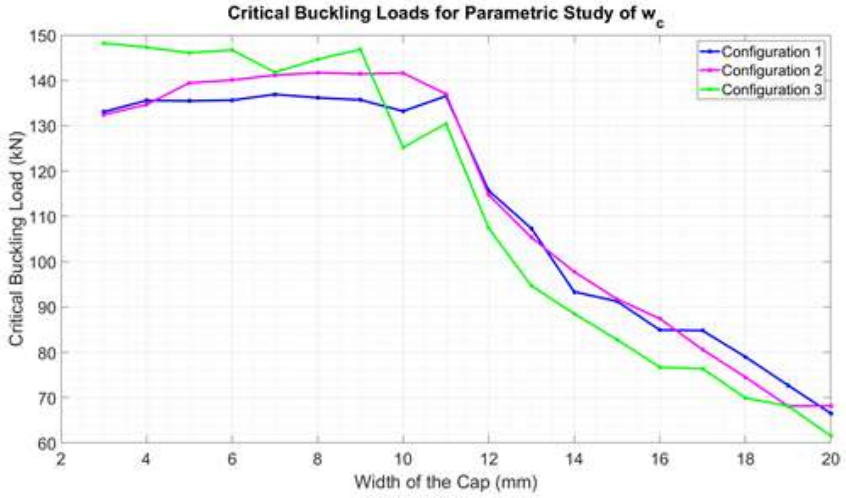

Figure 6.10. Critical buckling load vs. w_c.

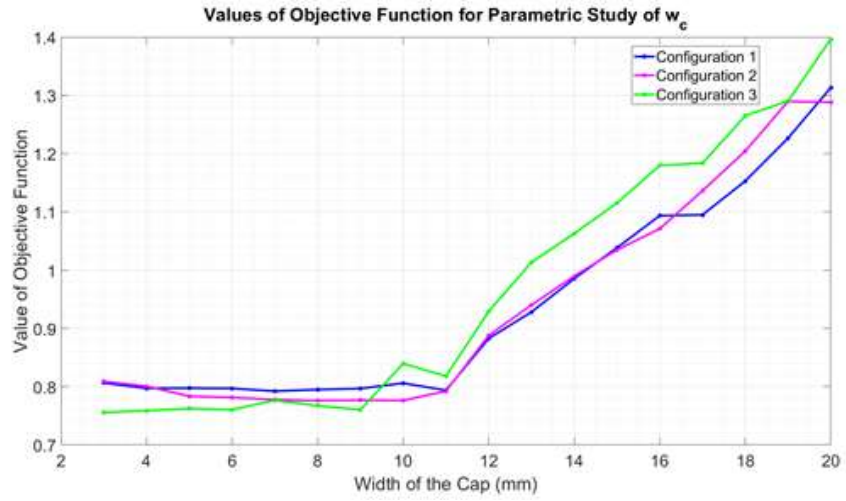

Figure 6.11. Objective function value vs. w_c.

Analyzing Figure 6.10 and Figure 6.11, it can be observed that increasing w_c beyond 10 mm leads to a decrease in the critical buckling load of the structure and an increase in the objective function value. In order to investigate this change in the buckling load and the objective function, the results of configuration 2 with a w_c value of 8 mm and a w_c value of 16 mm are compared. The results are shown in Figure 6.12 to Figure 6.14.

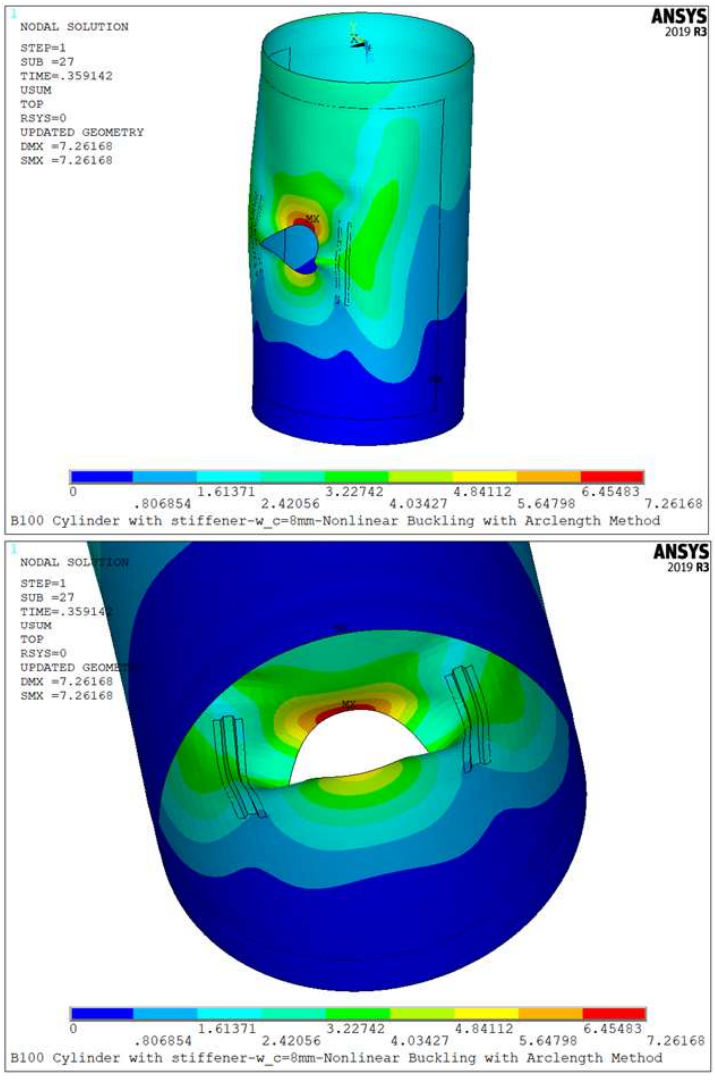

Figure 6.12. Resultant displacement contour plot, with a scale factor of five, for Configuration 2 with $w_c = 8mm$.

Figure 6.12 shows the resultant displacement of Configuration 2 with $w_c = 8mm$ at the onset of the buckling of the structure. According to the displacement results, the added stiffener reinforcements lead to an increase in the stiffness around the cutout, enhancing the buckling resistance of the structure.

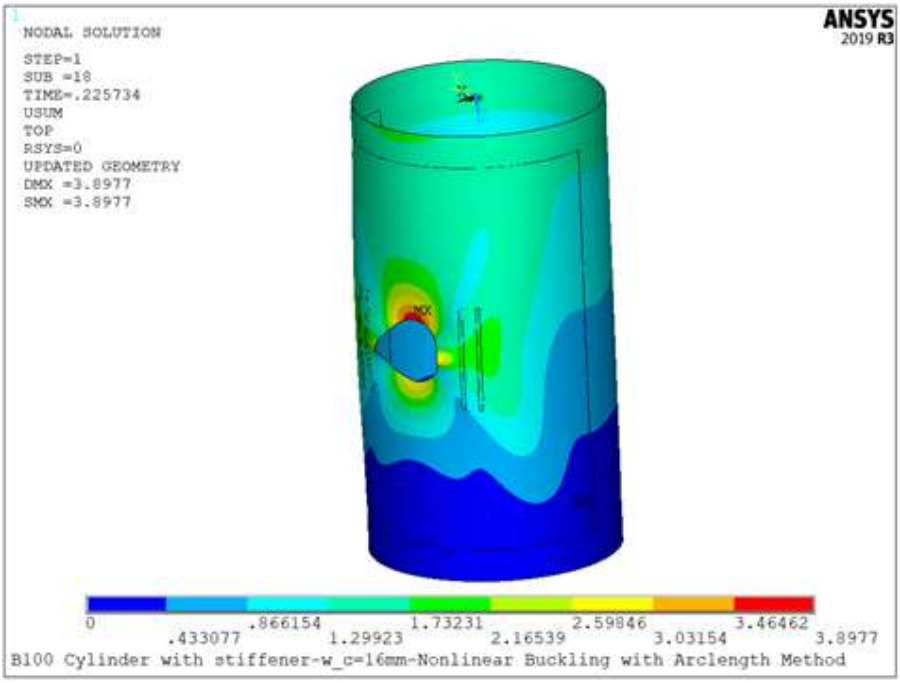

Figure 6.13. Resultant displacement contour plot #1, with a scale factor of five, for Configuration 2 with $w_c = 16mm$.

Figure 6.13 and Figure 6.14 show the resultant displacement of Configuration 2 with $w_c = 16$ mm at the onset of the structure. According to the displacement results, increase in w_c resulted in buckling of the cap of the stiffener itself leading to a reduction in its stiffness. Considering the buckling mode shown in Figure 6.14, it can be deduced that increasing w_c further would lead to premature buckling of stiffeners.

Combining all the available data, the upper and the lower bounds for w_c are chosen to be 12 mm and 4 mm, respectively.

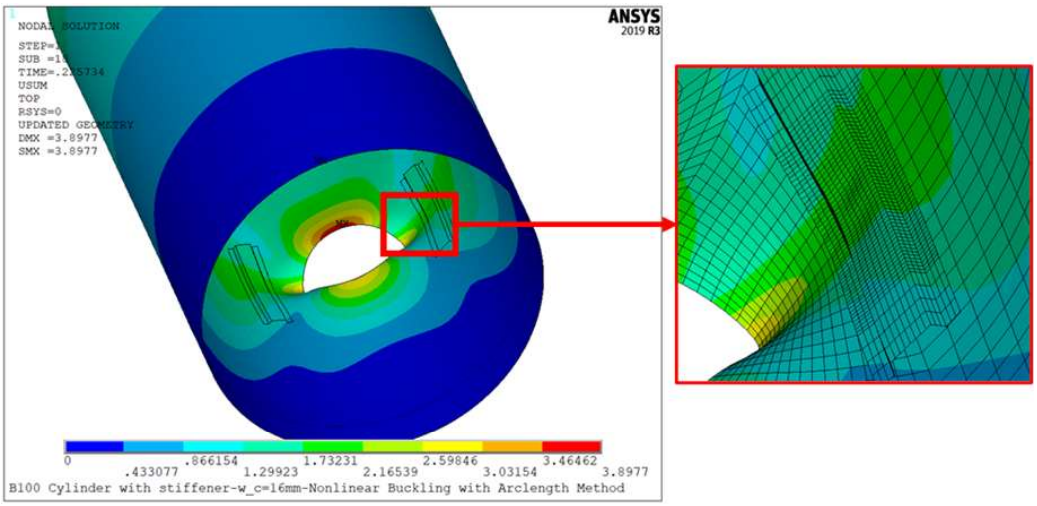

Figure 6.14. Resultant displacement contour plot #2, with a scale factor of five, for Configuration 2 with $w_c = 16$ mm.

6.2.2. The effect of width of the flange of the stiffener

The configurations used for the parametric study of w_f are shown in Table 6.6.

Table 6.6. Configurations used for the parametric study of width of the flange of the stiffener.

Configuration Number	Ply angles for stiffener(deg)	l_{st} (mm)	h_{st} (mm)	θ_{st} (deg)	w_c (mm)	w_f (mm)	d_{st} (mm)
4	90/23/-23/-90	120	4	45	4	4-20	100
5	90/23/-23/-90	250	4	60	6	4-20	100
6	90/23/-23/-90	350	6	75	4	4-20	100

As can be seen on Table 6.6, the parametric study is conducted for w_f values varying from 4 to 20 mm with intervals of 1.0 mm. The resulting buckling loads and objective function values of the parametric study for the width of the flange of the stiffener are shown in Figure 6.15 and Figure 6.16 respectively.

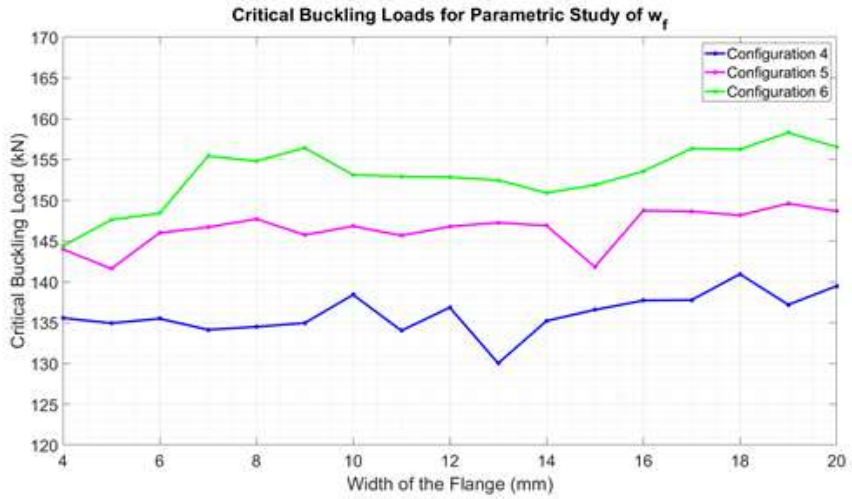

Figure 6.15. Critical buckling load vs. w_f.

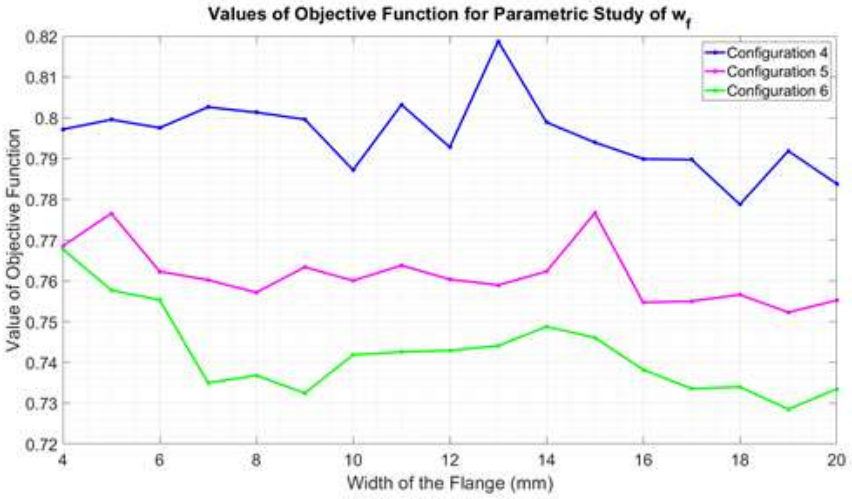

Figure 6.16. Objective function value vs. w_f.

Figure 6.15 and Figure 6.16 show that increasing the width of the flange may increase the critical buckling load of the structure. The impact of an increase in the buckling load changes depending on the configuration. Since the thickness of the stiffener is taken to be one-fourth of that of the cylinder, the effect of additional thickness coming from the width of the flange is expected to be much less, but the

width of the cap has a more significant effect because the cap leads to a larger increase in bending stiffness. That is because additional width of the cap would increase the moment of inertia against out-of-plane buckling much more. Yet, the results do not imply a certain trend between the width of the flange and the buckling load or the objective function values. Therefore, there is no need to further increase the upper limit. There should also be a sufficiently wide flange to provide sufficiently strong adhesion between the stiffener and the cylinder. Accordingly, the lower and upper bounds of 5 mm and 20 mm are chosen. As the optimization proceeds further, changes in width of the flange values for optimal configuration are checked whether the direction of change is towards the upper or lower bounds.

6.2.3. The effect of the stiffener length

The configurations used for the parametric study of l_{st} are shown in Table 6.7.

Table 6.7. Configurations used for the parametric study of the length of the stiffener.

Configuration Number	Ply angles for stiffener(deg)	l_{st} (mm)	h_{st} (mm)	θ_{st} (deg)	w_c (mm)	w_f (mm)	d_{st} (mm)
7	90/23/-23/-90	80-600	4	45	4	6	100
8	90/23/-23/-90	80-600	6	60	6	4	100
9	90/23/-23/-90	80-600	8	75	5	5	100

As can be seen in Table 6.7, the parametric study is conducted for l_{st} values varying from 80 to 600 mm with intervals of 40 mm. The resulting buckling loads and objective function values of the parametric study for the length of the stiffener are shown in Figure 6.17 and Figure 6.18, respectively.

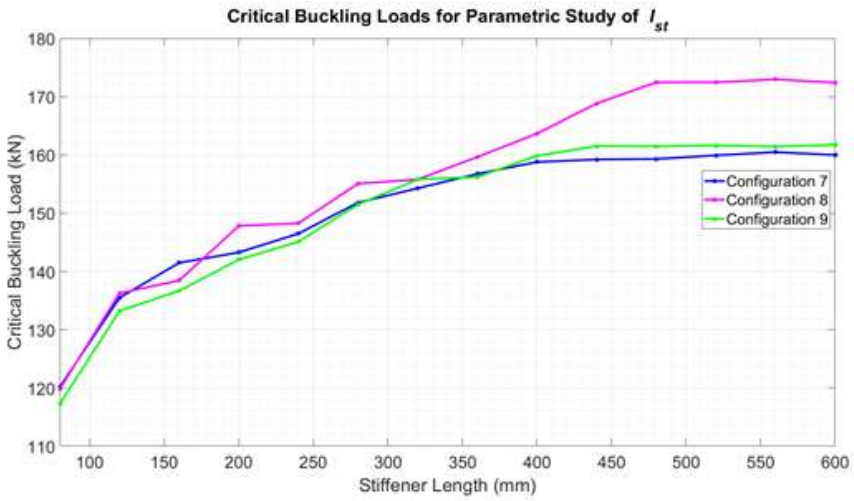

Figure 6.17. Critical buckling load vs. l_{st}.

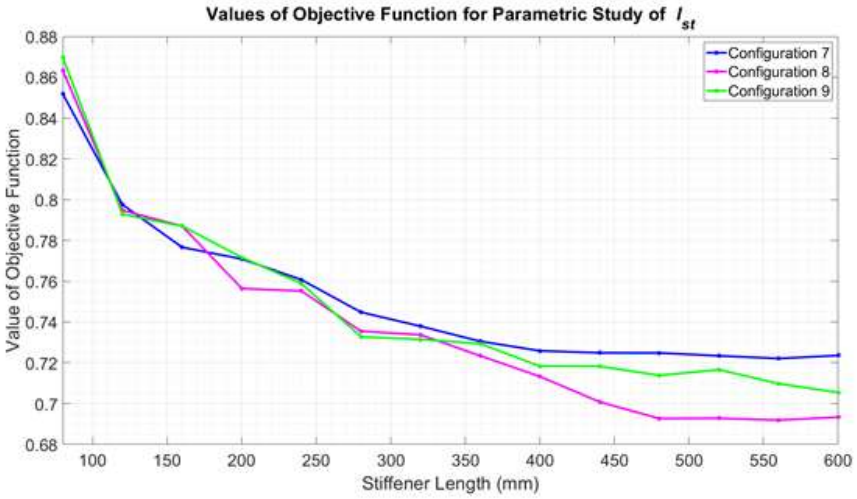

Figure 6.18. Objective function value vs. l_{st}.

Figure 6.17 and Figure 6.18 indicate that as the length of the stiffener is increased, the critical buckling load increase. Additionally, the gain in the buckling load exceeds the loss due to the increase in the total mass, which leads to a reduction in the objective function value. It is also important to note that the maximum amount of gain percentage of the critical buckling load occurs when the length is increased

from 80 mm to 400 mm. Considering that the diameter of the cutout is 100 mm, it can be deduced that having a stiffener longer than the diameter of the hole is more advantageous in terms of resistance against buckling. The lower and the upper bounds for the length of the stiffener is chosen to be 100 mm and 600 mm.

6.2.4. The effect of the stiffener height

The configurations used for the parametric study of h_{st} are shown in Table 6.8.

Table 6.8. Configurations used for the parametric study of the height of the stiffener.

Configuration Number	Ply angles for stiffener(deg)	l_{st} (mm)	h_{st} (mm)	θ_{st} (deg)	w_c (mm)	w_f (mm)	d_{st} (mm)
10	90/23/-23/-90	120	4-20	45	4	6	100
11	90/23/-23/-90	160	4-20	30	6	4	100
12	90/23/-23/-90	240	4-20	75	8	6	100

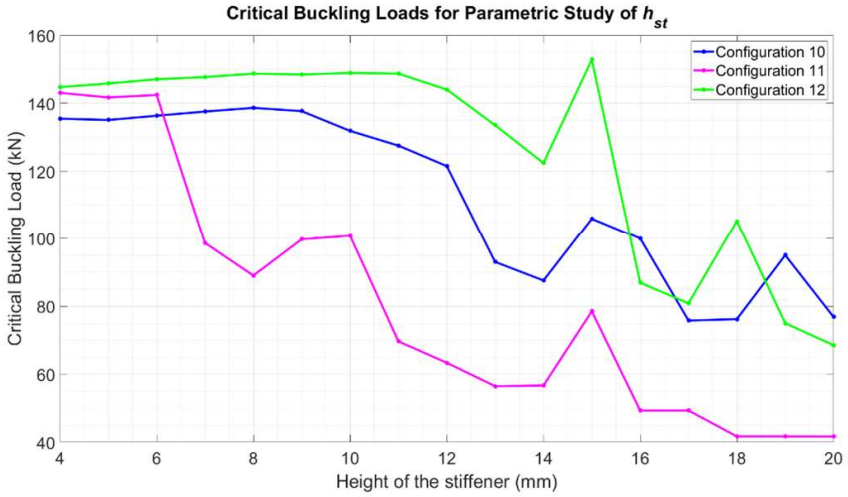

Figure 6.19. Critical buckling load vs. h_{st}.

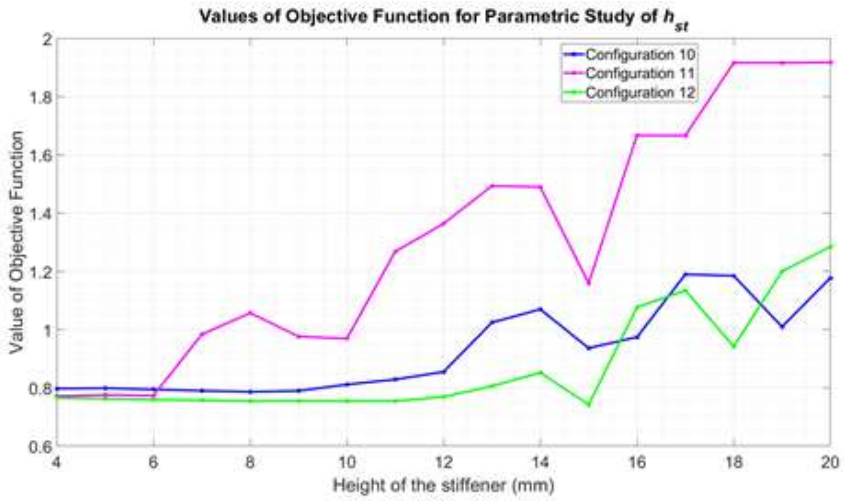

Figure 6.20. Objective function value vs. h_{st}.

As can be seen in Table 6.8, the parametric study is conducted for h_{st} values varying from 4 to 20 mm with intervals of 1.0 mm. The resulting buckling loads and objective function values of the parametric study for the stiffener height are shown in Figure 6.19 and Figure 6.20 respectively.

According to Figure 6.19 and Figure 6.20, the effect of the stiffener height on the buckling load and the corresponding objective function value depends on the configuration. For example, configuration 11 shows a sudden decrease in the buckling load when the height of the stiffener reaches above 6 mm, whereas the buckling load corresponding to configurations 10 and 12 even shows a slight increase up to a height of 8 mm. However, analyzing the figures it can be deduced that increasing the height of the stiffener leads to a reduction in the buckling load of the cylinder. In order to investigate this change in the buckling load and the objective function, the results of configuration 10 with h_{st} value of 6 mm and h_{st} value of 16 mm are compared. The results are shown in Figure 6.21 to Figure 6.23.

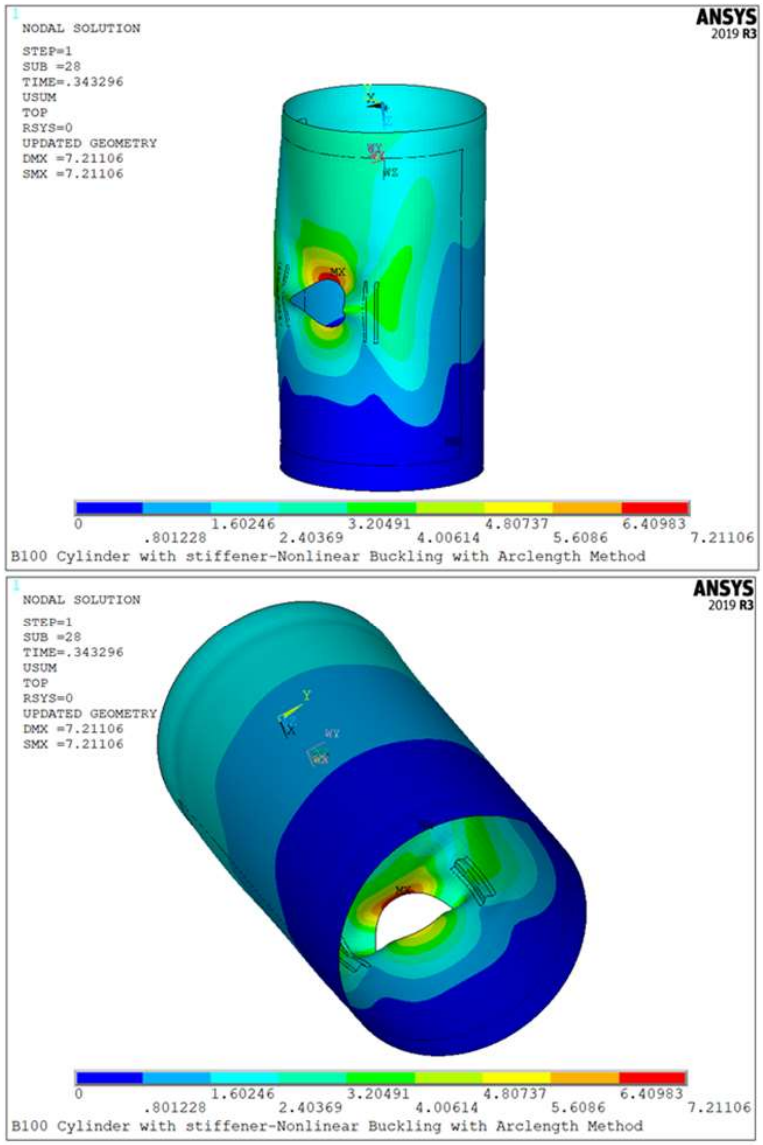

Figure 6.21. Resultant displacement contour plot, with a scale factor of five, for Configuration 10 with $h_{st} = 6mm$.

Figure 6.21 shows the resultant displacement for Configuration 10 with h_{st}=6 mm. Examining the figure, it can be deduced that as the cylinder starts to buckle, there is no local buckling in the stiffeners. Therefore, they serve as reinforcement elements properly.

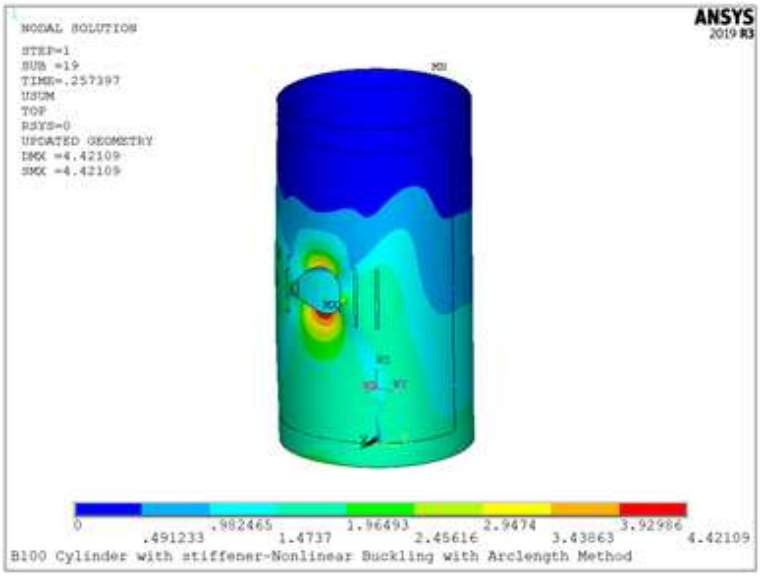

Figure 6.22. Resultant displacement contour plot #1, with a scale factor of five, for Configuration 10 with $h_{st} = 16mm$.

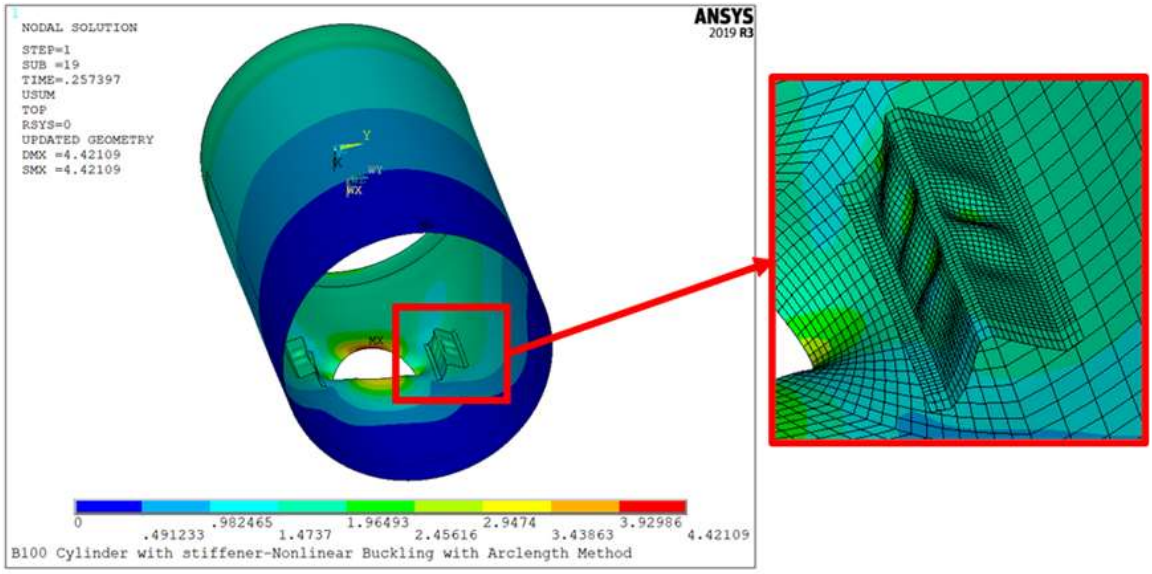

Figure 6.23. Resultant displacement contour plot #2, with a scale factor of five, for Configuration 10 with $h_{st} = 16mm$.

Figure 6.22 and Figure 6.23 show the resultant displacement state during the onset of buckling for configuration 10 with h_{st}=16 mm. Examining the deformation, it can be seen that the stiffeners experience out-of-plane bending as the structure starts to buckle. That is why the stiffeners cannot provide considerable resistance to buckling, resulting in a buckling load of 100 kN, which represents a 4% increase compared to the buckling load of the unreinforced cylinder, 96.2 kN. Thus, the lower and the upper bounds for the height of the stiffener is chosen as 5 mm and 15 mm, respectively.

6.2.5. The effect of flange-to-cap angle of the stiffener

The configurations used for the parametric study of θ_{st} are shown in Table 6.9.

Table 6.9. Configurations used for the parametric study of flange-to-cap angle of the stiffener.

Configuration Number	Ply angles for stiffener(deg)	l_{st} (mm)	h_{st} (mm)	θ_{st} (deg)	w_c (mm)	w_f (mm)	d_{st} (mm)
13	90/23/-23/-90	180	6	15-90	8	4	100
14	90/23/-23/-90	260	8	15-90	5	5	100
15	90/23/-23/-90	210	6	15-90	6	8	100

As can be seen on Table 6.9, the parametric study is conducted for θ_{st} values changing from 15 degress to 90 degrees with the intervals of 5 degrees. The resulting buckling loads and objective function values of the parametric study conducted for the flange-to-cap angle of the stiffener are shown in Figure 6.24 and Figure 6.25 respectively.

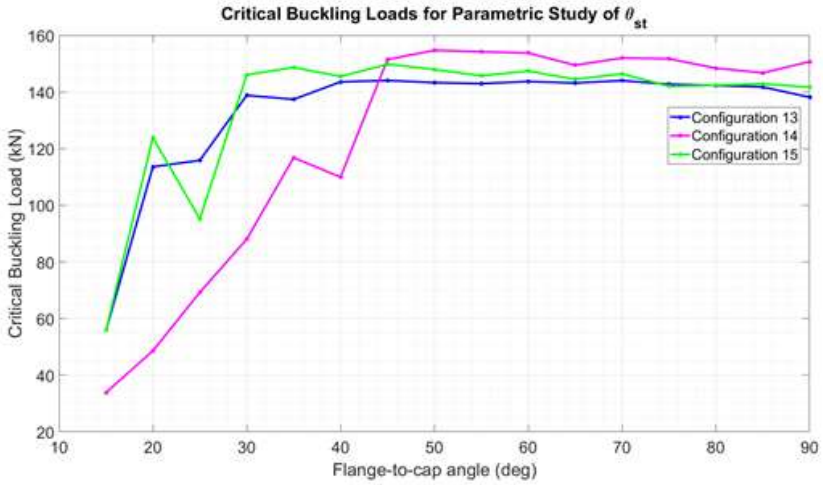

Figure 6.24. Critical buckling load vs. θ_{st}.

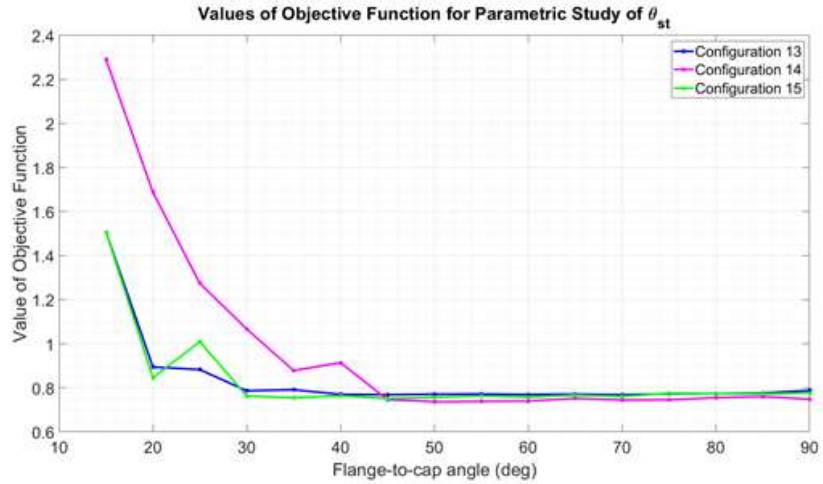

Figure 6.25. Objective function value vs. θ_{st}.

The results shown in Figure 6.24 and Figure 6.25 indicate that as the values for θ_{st} is increased, the critical buckling load of the structure increases drastically, accompanying a similar amount of decrease in the objective function value. In order to investigate this behavior, two analyses are carried out using Configuration 13 with values of 25 and 60 degrees for θ_{st}. The results of these analyses are shown in Figure 6.26 to Figure 6.28.

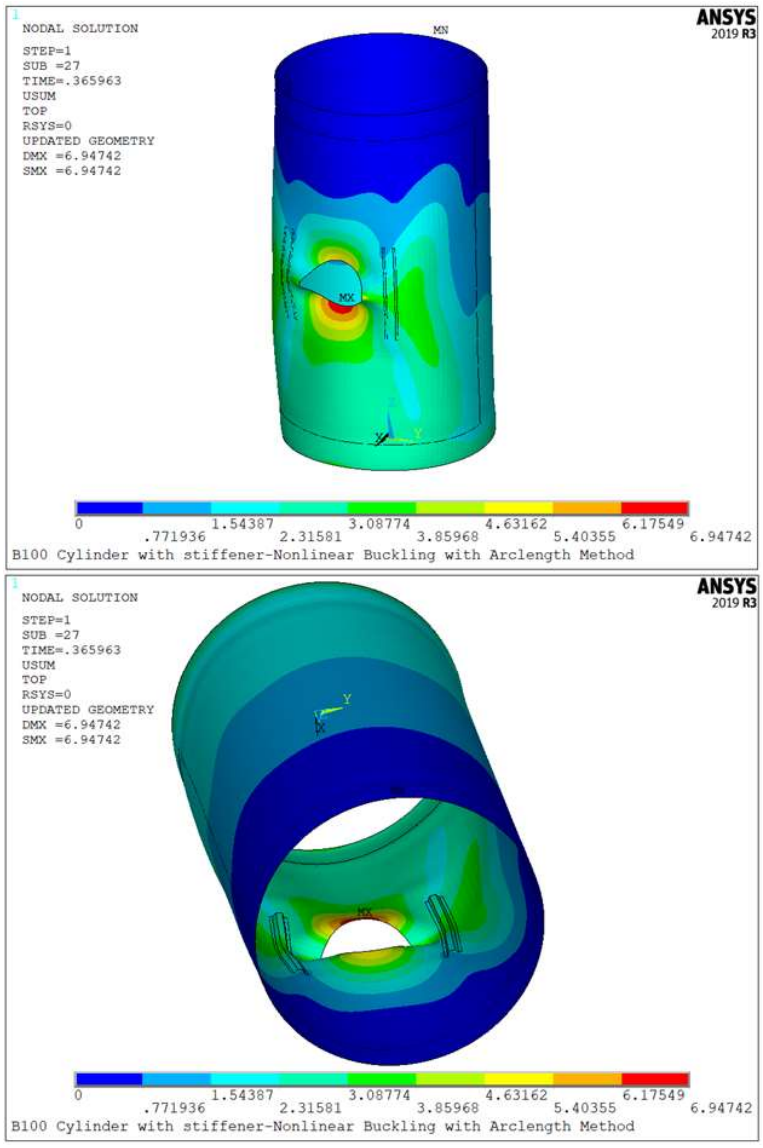

Figure 6.26. Resulting displacement contour plot, with a scale factor of five, for Configuration 13 with $\theta_{st} = 60$degrees.

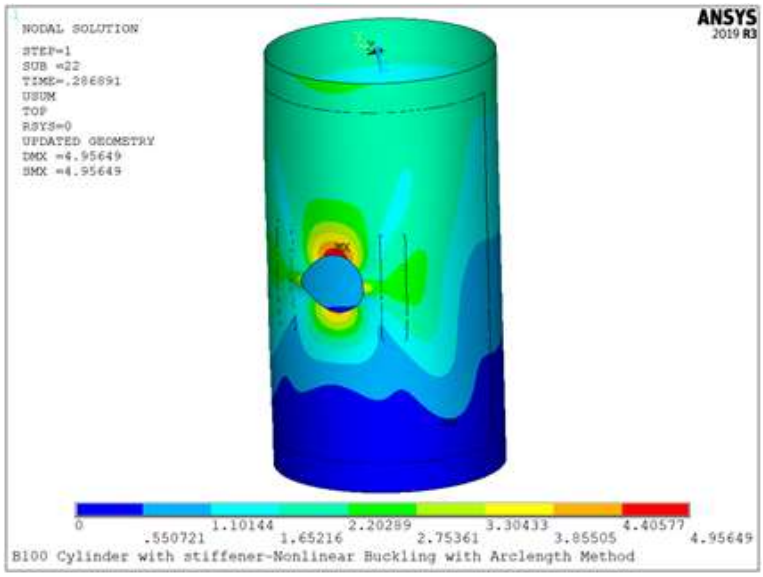

Figure 6.27. Resulting displacement contour plot #1, with a scale factor of three, for Configuration 13 with $\theta_{st} = 25$ degrees.

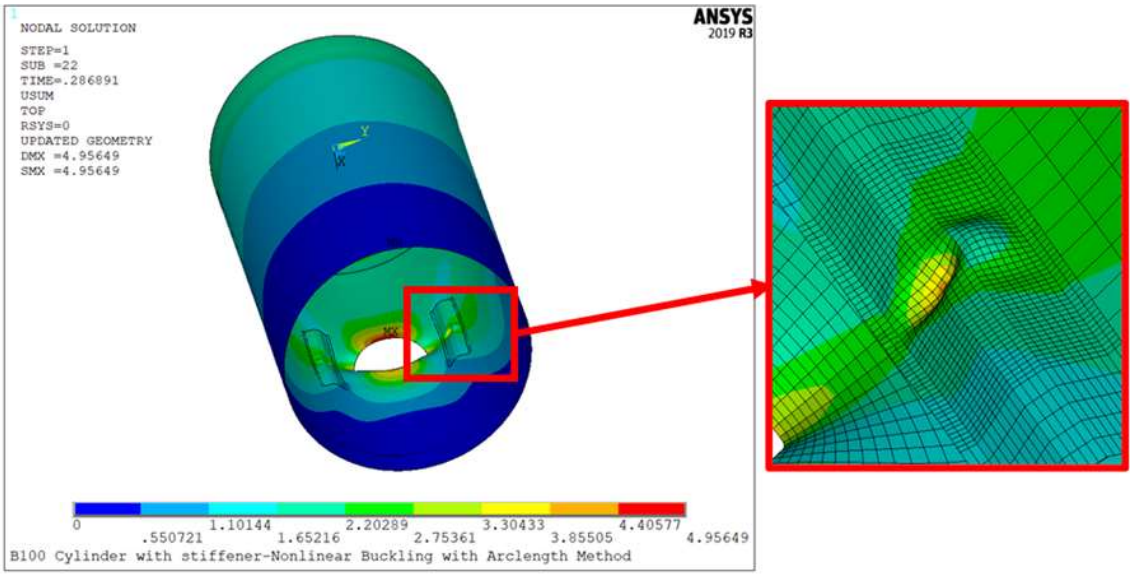

Figure 6.28. Resulting displacement contour plot #2, with a scale factor of three, for Configuration 13 with $\theta_{st} = 25$ degrees.

Comparing the results in Figure 6.26 and Figure 6.28, it can be observed that use of a flange-to-cap angle of 25 degrees leads to a premature local buckling of the stiffeners. That is because as the angle of the stiffener is decreased while keeping the height of the stiffener constant, the width of the section connecting the flange and the cap section increases. This leads to a decreased bending stiffness of the stiffeners, a behavior similar to that observed previously with increased w_c values. Considering the results of the parametric study, the lower and the upper bounds for the flange-to-cap angle are chosen as 40 degrees and 80 degrees.

7. RESULTS AND DISCUSSIONS

Weighting coefficients are chosen to be 0.7 and 0.3 for w_{mass} and w_{load} in the beginning, which give a higher importance to the critical buckling load compared to the weight reduction. Weighting coefficients of 0.9 and 0.1 for w_{mass} and w_{load} are also tried. No significant change is observed in the optimum configuration parameters. This may be because the mass of the stiffeners is very small compared to the total mass and the percentage increase in the mass of the structure due to reinforcement is much lower compared to the percentage increase in the critical buckling load of the structure due to reinforcement. Accordingly, the initially chosen values of the weighting coefficients are considered suitable and the weighting coefficients of 0.7 and 0.3 for w_{mass} and w_{load} are used throughout this study.

At first, two separate optimization studies are carried out. The constant parameters used in these studies are shown in Table 7.1. The parameters that define the geometry of the stiffeners are varied during optimizations #1 and #2, which are l_{st}, h_{st}, θ_{st}, w_c and w_f. As can be seen in Table 7.1, the only difference between the constant parameters used in the optimization studies #1 and #2 is the distance of the stiffener to the hole center.

Table 7.1. Parameters used in optimization studies #1 and #2.

Optimization Study Number	Ply angles for stiffeners (deg)	Total thickness of stiffeners (mm)	Distance to hole center (mm)
#1	90/23/-23/-90	0.55	100
#2	90/23/-23/-90	0.55	80

In the beginning of the optimization, random configurations are created in a large design space defined by the limits of the parameters. Consequently, the objective function values for these initial configurations may differ greatly. As the optimization

progresses, the objective function values in the configuration set not only decrease, but also become closer step by step, consequently converging to the minimum value. Since generating a new configuration better than the worse configuration is considered as an improvement, the difference between the worse configuration and the best configuration can be used as a metric to keep track of the progress of the optimization. Therefore, this difference is plotted for each optimization study.

In order to reach the optimum design, keeping track of the temperature parameter is also crucial. As the successive outer loops are completed, the temperature is decreased according to the values of R_{acc} and R_{step}. Therefore, not only temperature parameter but also R_{acc} and R_{step} are plotted for each optimization study.

Since the optimization algorithm reduces the variation in each optimization parameter depending on the Markov chain iterations conducted and the number improvements found in each Markov chain, keeping track of number of Markov chain iterations and number of improvements also gives an idea about the progress of the optimization. That is why these two metrics are plotted against each other in each optimization study to show the reduction of the variation in the parameters.

7.1. Results of Optimization #1

Figure 7.1 shows the difference between the objective function values of the worse and the best configurations found in optimization #1. As can be seen in Figure 7.1, the difference in the objective function values of the worse and best in the current set becomes smaller, and therefore, the set of configurations converge to the optimum design.

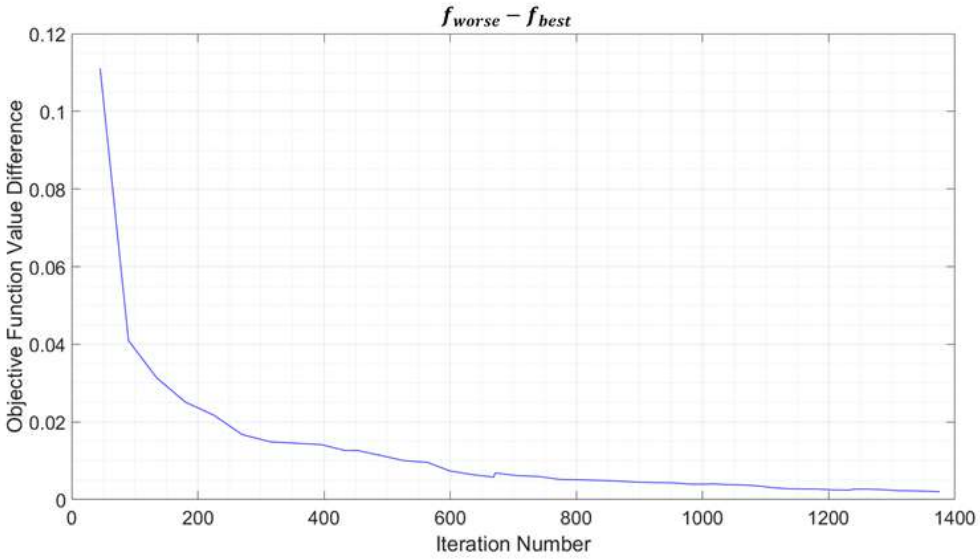

Figure 7.1. The difference between the objective function values of the worse and best points through optimization #1.

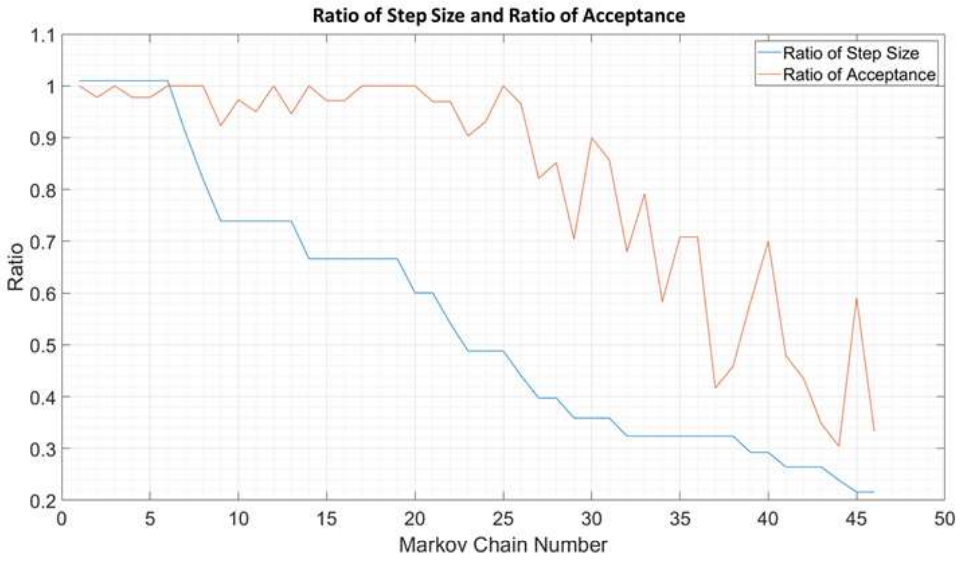

Figure 7.2. Comparison between the ratio of the current step size to initial step size and the ratio of the number of the accepted configurations to the total number of configurations in a Markov chain through optimization #1.

Figure 7.2 shows the comparison between the ratio of the current step size to

initial step size and the ratio of the number of the accepted configurations to the total number of configurations in a Markov chain through optimization #1 plotted against Markov chain number. Analyzing the trend of ratio of acceptance in Figure 7.2, the randomness of the optimization process can be seen.

The plot of temperature parameter value in each Markov chain is shown in Figure 7.3.

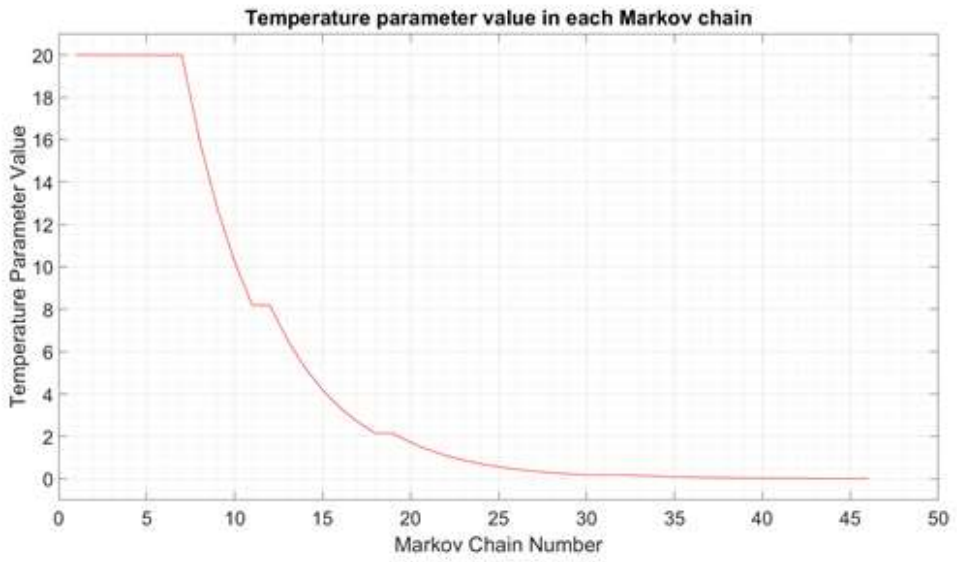

Figure 7.3. Temperature parameter value vs Markov chain number in optimization #1.

In Figure 7.3, it can be seen that the value of the temperature parameter decreases as the optimization progresses, until it converges to zero. This convergence shows that the optimization #1 converges to a point where the acceptance of a worse than worst-best configuration is improbable, since the probability of acceptance of such a condition also converges to zero as the temperature parameter converges to zero according to Equation (5.6).

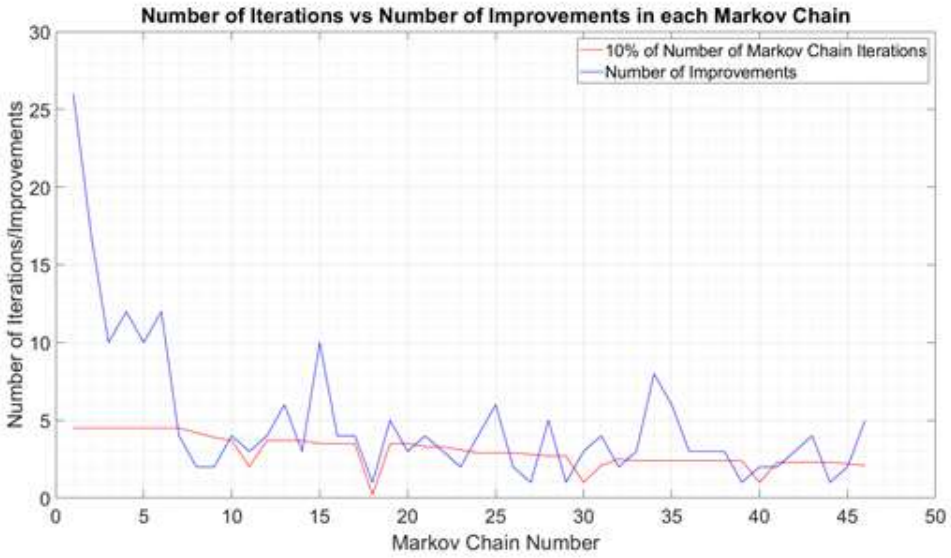

Figure 7.4. 10% of the number of iterations vs number of improvements in each Markov chain in optimization #1.

The comparison plot of %10 of the number of iterations and the number of improvements in each Markov chain is given in Figure 7.4. Comparing Figure 7.2 and Figure 7.4, it can be seen that the ratio of the step size decreases whenever the number of improvements drops below 10% of the number of Markov chain iterations.

The resultant displacement contour plot created at the buckling load in optimization #1 is shown in Figure 7.5.

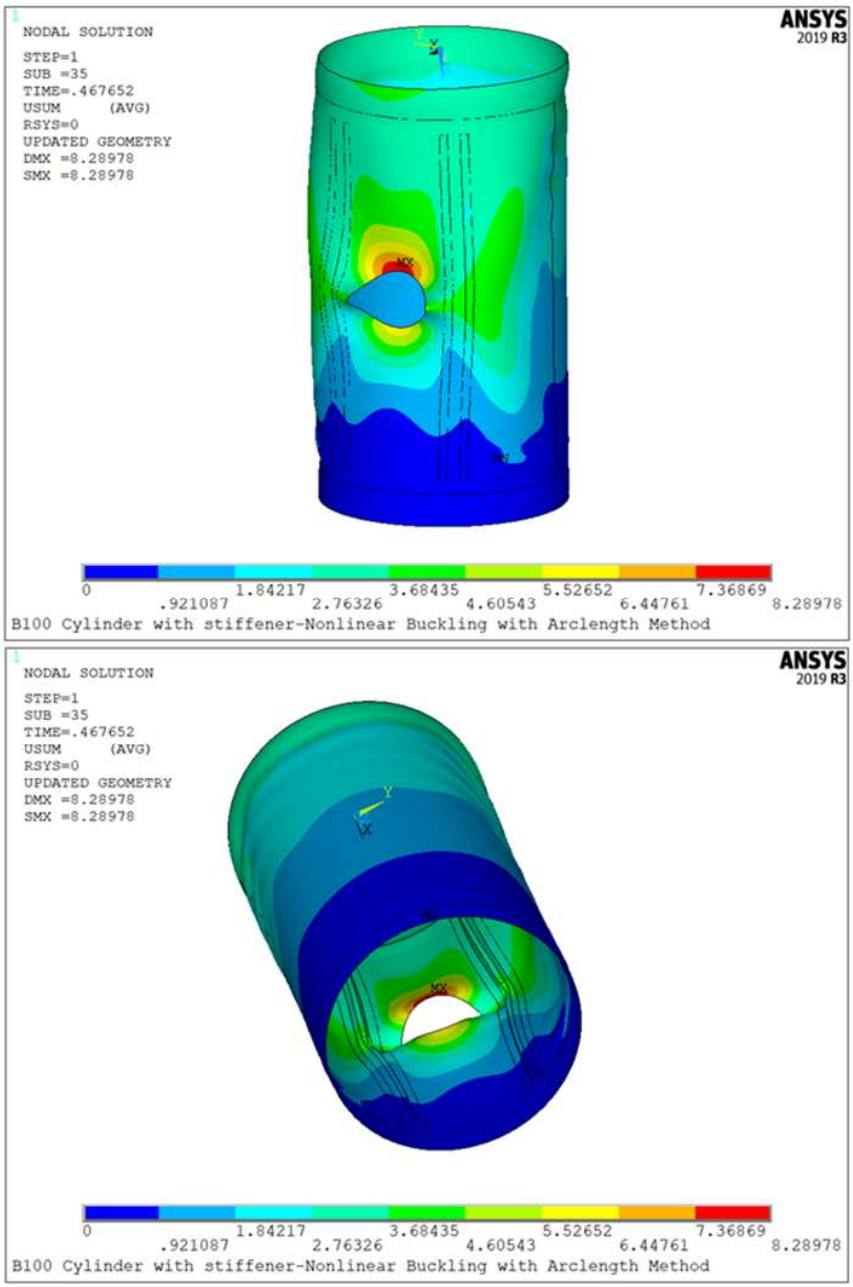

Figure 7.5. Resultant displacement contour plot of the optimum design found in Optimization #1 with straight stiffeners, with a scale factor of five.

Figure 7.6 shows the reaction load vs end displacement plot of the optimum design found in optimization 1 along with the numerical results found in the model validation step for B100 reference cylinder.

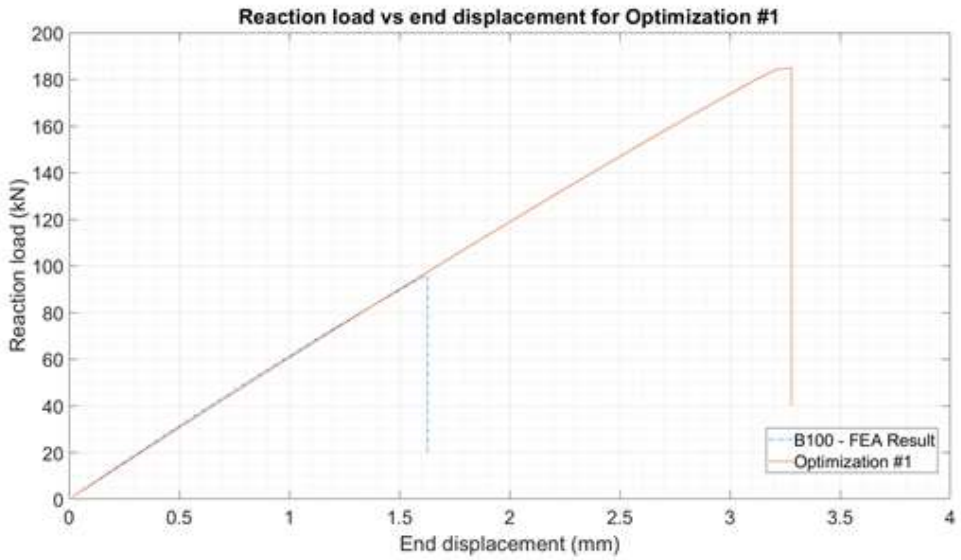

Figure 7.6. Reaction load vs end displacement for optimization #1.

The corresponding values for the geometric parameters, the critical buckling load, the stiffener mass, and the objective function value of the optimum design found in optimization #1 are given in Table 7.2.

Table 7.2. The cross-sectional design parameters, the mass of the stiffener and the objective function value of the optimum design found in optimization #1.

h_{st} (mm)	l_{st} (mm)	θ_{st} (mm)	w_c (mm)	w_f (mm)	F_{cr} (kN)	m_{re} (kg)	$f_{objective}$
9.835	552.12	59.167	7.528	12.366	184.9	0.066	0. 669286

7.2. Results of Optimization #2

Figure 7.7 shows the difference between the objective function values of the worse and the best configurations found in optimization #2. As can be seen in Figure 7.7, the difference in the objective function values of the worse and best configurations in the current set becomes smaller, and therefore, the set of configurations converge to the optimum design.

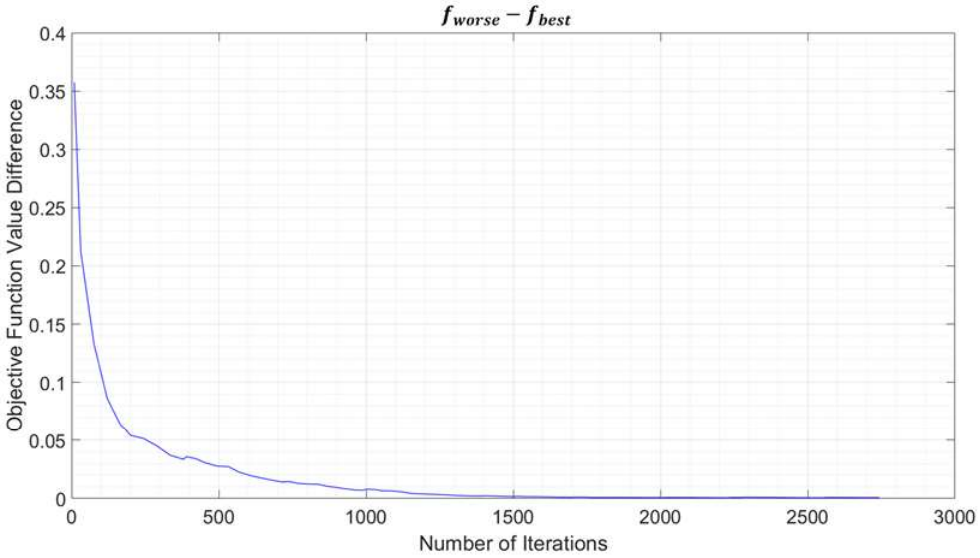

Figure 7.7. The difference between the objective function values of the worse and best points through optimization #2.

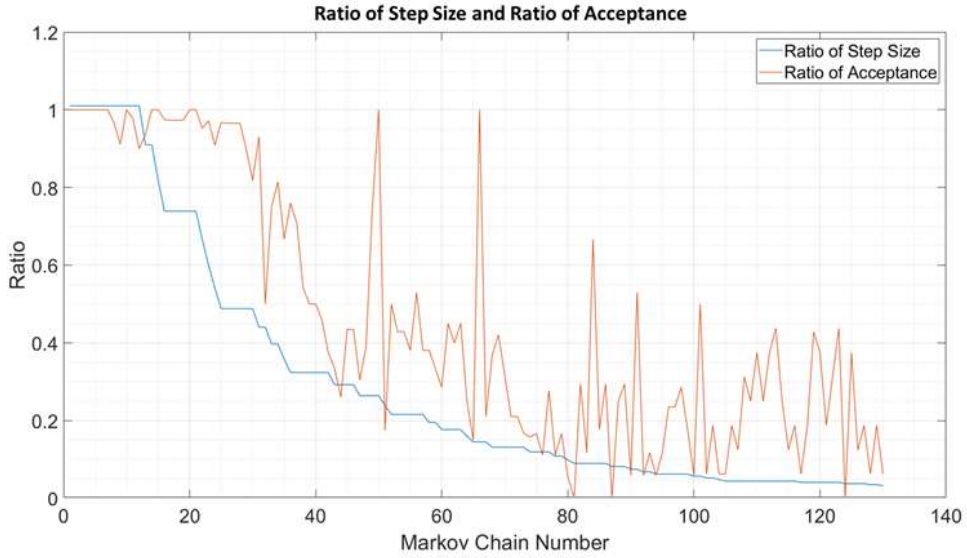

Figure 7.8. Comparison between the ratio of the current step size to initial step size and the ratio of the number of the accepted configurations to the total number of configurations in a Markov chain through optimization #2.

Figure 7.8 shows the comparison between the ratio of the current step size to initial step size and the ratio of the number of the accepted configurations to the total number of configurations in a Markov chain through optimization #2 plotted against Markov chain number. The trend of the ratio of acceptance in Figure 7.8 indicates the randomness of the optimization process.

The plot of the temperature parameter value in each Markov chain is shown in Figure 7.9.

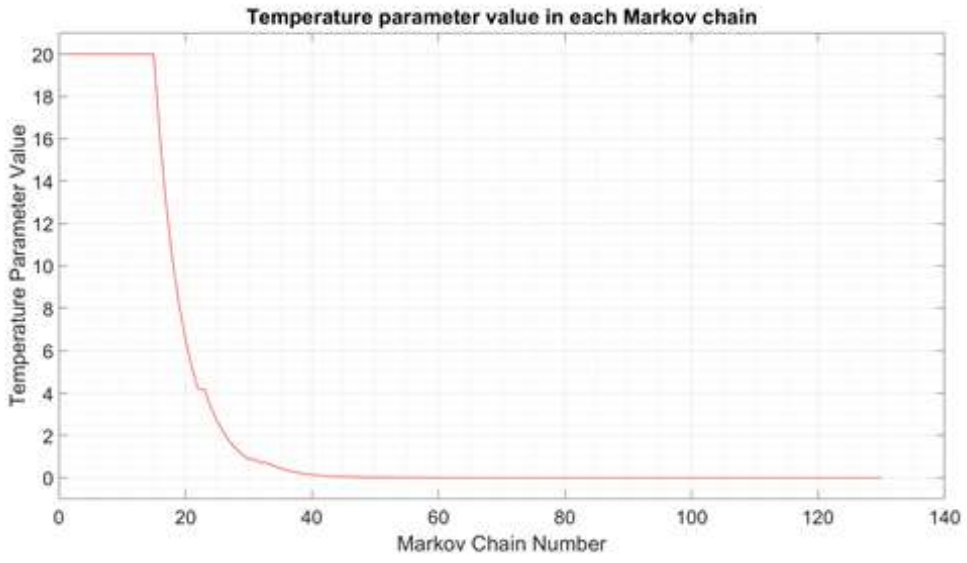

Figure 7.9. Temperature parameter value vs Markov chain number in optimization #2.

Figure 7.9 shows that the value of the temperature parameter decreases during the optimization progress until it converges to zero. This converging behavior shows that the optimization #2 has converged to a point where the acceptance of a worse than worst-best configuration is improbable, since the probability of acceptance of such a condition also converges to zero as the temperature parameter converges to zero according to Equation (5.6).

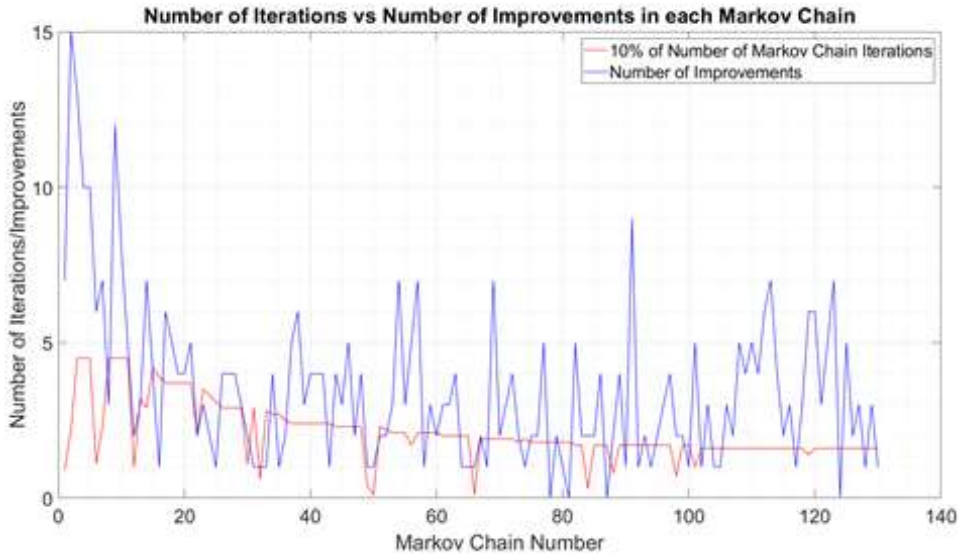

Figure 7.10. 10% of the number of iterations vs number of improvements in each Markov chain in optimization #2.

The comparison plot of 10% of the number of iterations and the number of improvements in each Markov chain is given in Figure 7.10. Comparing Figure Figure 7.8 and Figure 7.10, it can be seen that the ratio of the step size decreases whenever the number of improvements drops below 10% of the number of Markov chain iterations.

Figure 7.11 shows the resultant displacement contour plot, with a scale factor of five, for optimization #2.

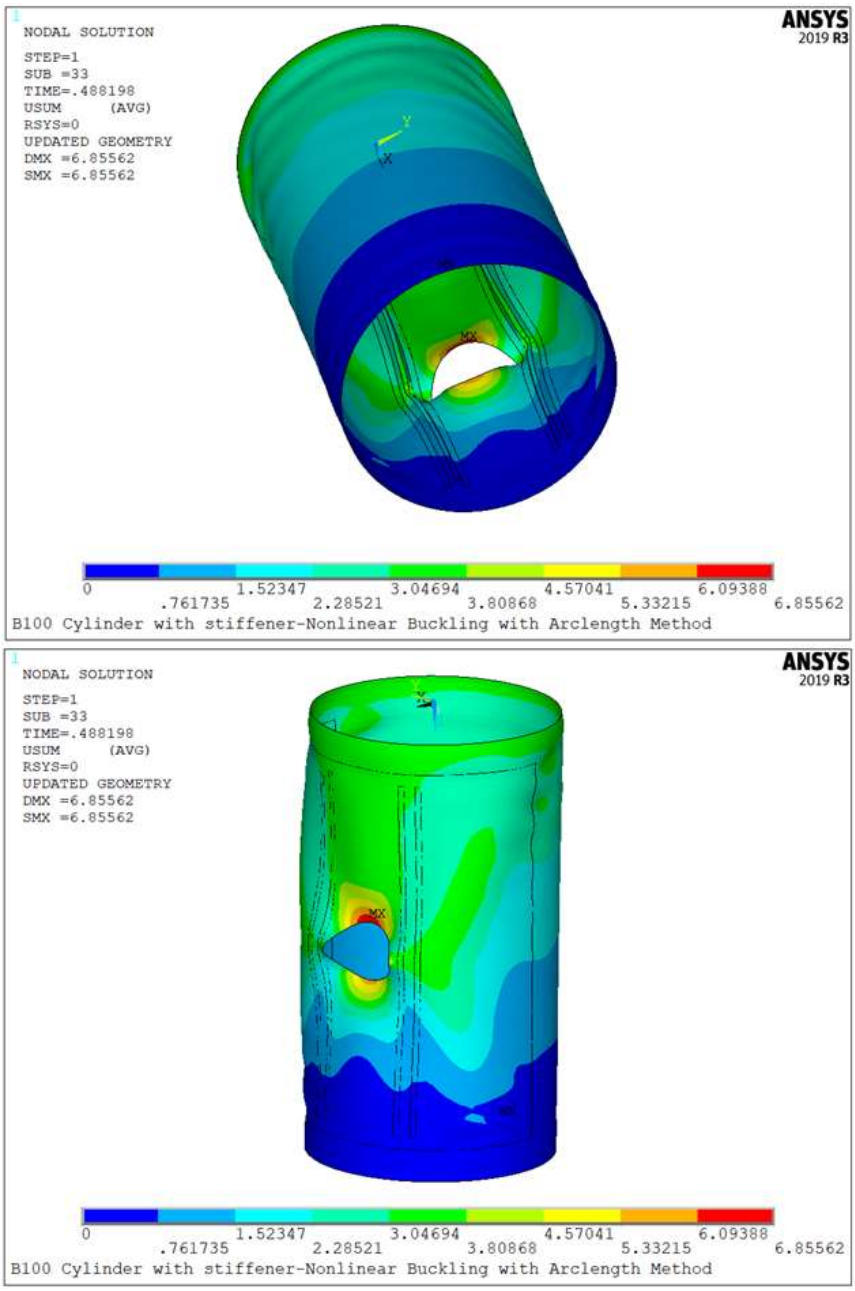

Figure 7.11. Resultant displacement contour plot of the optimum design found in Optimization #2 with straight stiffeners, with a scale factor of five.

Figure 7.12 shows the load vs end displacement plot of the optimum design found in optimization #2 along with the numerical results found in the model validation step for B100 reference cylinder.

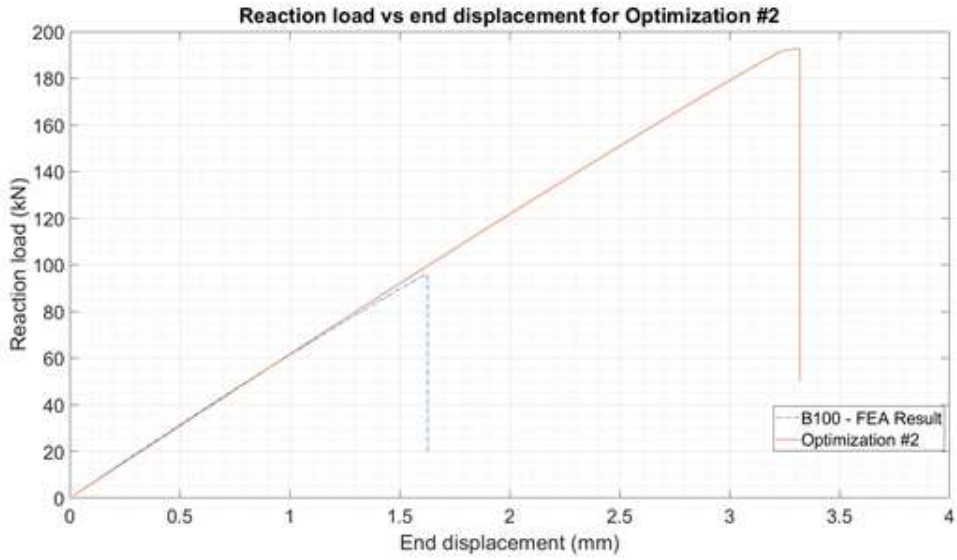

Figure 7.12. Reaction load vs end displacement for optimization #2.

The corresponding values for the geometric parameters, the critical buckling load, the stiffener mass, and the objective function value of the optimum design found in optimization #2 are given in Table 7.3.

Table 7.3. The cross-sectional design parameters, the mass of the stiffener and the objective function value of the optimum design found in optimization #2.

h_{st} (mm)	l_{st} (mm)	θ_{st} (mm)	w_c (mm)	w_f (mm)	F_{cr} (kN)	m_{st} (kg)	$f_{objective}$
11.35	560.21	64.589	6.258	9.028	192.8	0.060	0.653859

Comparing the results of optimization #1 and #2, the latter is found to be a better solution with a higher buckling load of 192.8 kN. This results also shows that placing the stiffeners closer to the cutout could yield higher buckling strength around the cutout. Therefore, this distance d_{st} is varied in the second step of the optimization where a total of four small stiffeners are applied around cutout.

7.3. Application of Small Stiffeners

In the second step of optimization, additional small stiffeners are applied around the cutout as shown in Figure 7.13. The cross section of a straight stiffener is rotated by an angle θ_{arc} and extruded with an amount l_{ext} along the yellow arrows shown in Figure 7.13 at four symmetric locations to create the small stiffeners, while d_{arc} denotes the axial distance between the center of the cutout and the point at which small stiffeners touch the straight stiffeners. To extend the reinforcements as much as possible, l_{ext} is calculated such that the two stiffeners on top and bottom coincide at the intersection point of the yellow arrows. Therefore, l_{ext} is dependent on parameters d_{arc}, θ_{arc}, and d_{st}, which is the distance between the center of the hole and the mid-point of the stiffener as mentioned before. That is why only these three parameters are varied in the second step of optimization. To determine the upper and lower bounds of these parameters, parametric studies are conducted for each parameter.

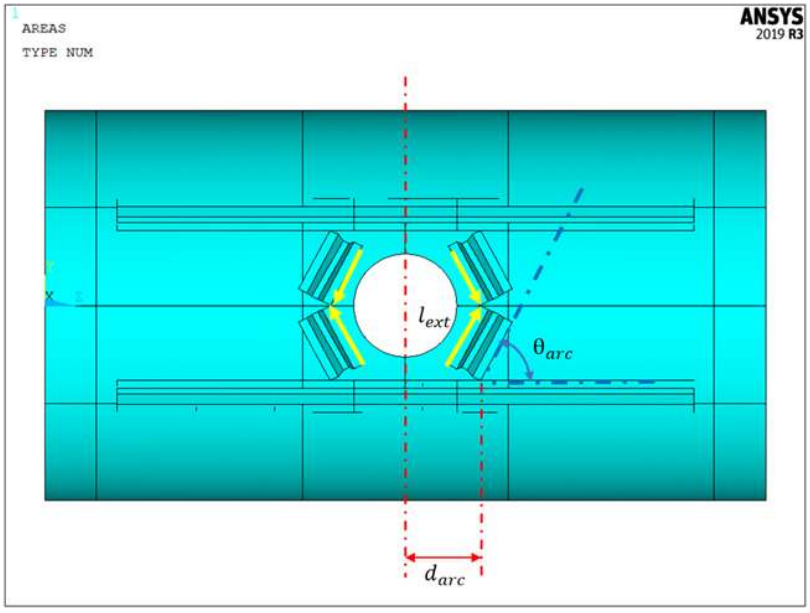

Figure 7.13. Application of small stiffeners around the cutout.

For this optimization study, the cross-sectional properties for small stiffeners are taken to be the same as those given in Table 7.3. Small stiffeners are applied directly to the optimum configuration found in optimization #2 given in section 7.2.

7.3.1. Parametric studies for small stiffeners

The configurations used for the parametric study of θ_{arc} are shown in Table 7.4.

Table 7.4. Configurations used for the parametric study of the rotation angle of small stiffeners.

Configuration Number	d_{st} (mm)	d_{arc} (mm)	θ_{arc} $(degrees)$
16	80	50	30-90
17	80	70	30-90
18	80	80	30-90

As can be seen in Table 7.4, the parametric study is conducted for values of θ_{arc} varying from 30° to 90° with intervals of 5.0°. The resulting buckling loads of the parametric study for the rotation angle of small stiffeners are shown in Figure 7.14.

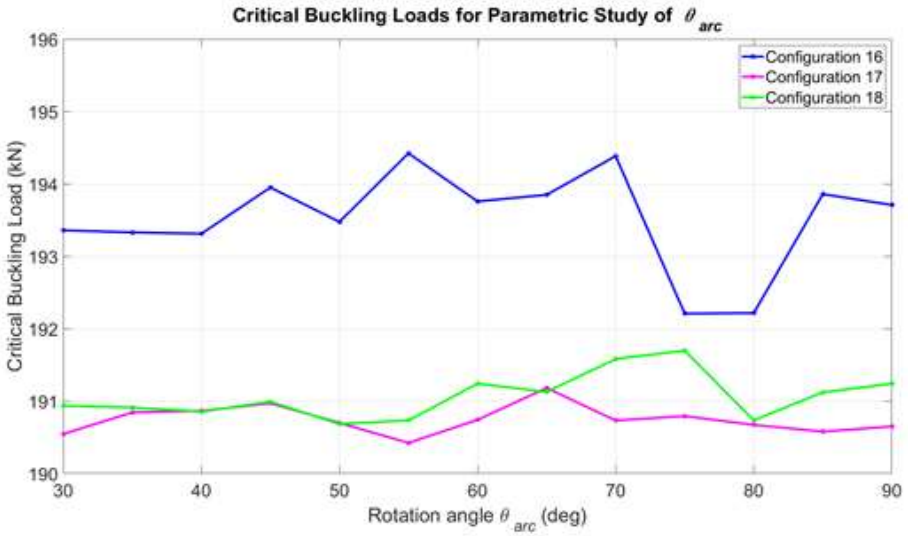

Figure 7.14. Critical buckling load vs. θ_{arc}.

The results shown in Figure 7.14 do not indicate a direct trend between the buckling load and the rotational angle of the small stiffeners. However, it can be seen that going below 45° does not provide an increase in the buckling load for any of the configurations. Increasing this angle beyond 75° leads to a decrease in the buckling load. The maximum amount of buckling load is observed at 70° for configuration 16 and at 75° for configurations 17 and 18. In order to include these points into the limits, the upper and lower bounds for the rotation angle of the small stiffeners is chosen as 45° and 80°, respectively.

The configurations used for the parametric study of d_{arc} are shown in Table 7.5.

Table 7.5. Configurations used for the parametric study of the axial distance between the center of the cutout and the small stiffeners.

Configuration Number	d_{st} (mm)	d_{arc} (mm)	θ_{arc} $(degrees)$
19	80	50-120	60
20	80	50-120	75
21	80	50-120	30

As can be seen in Table 7.5, the parametric study is conducted for values of d_{arc} varying from 50 mm to 120 mm with intervals of 5.0 mm. The resulting buckling loads of the parametric study for the axial distance between the center of the cutout and the small stiffeners are shown in Figure 7.15.

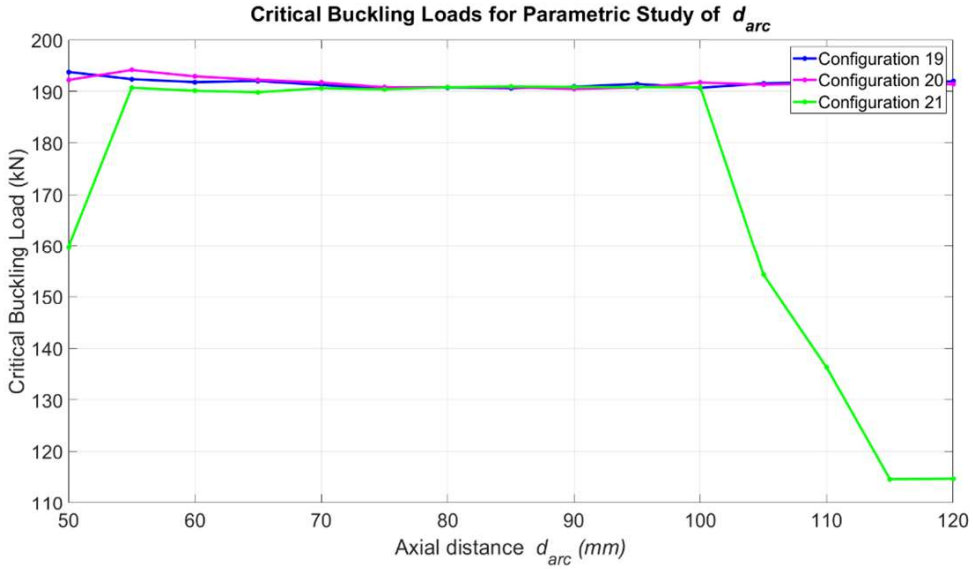

Figure 7.15. Critical buckling load vs. d_{arc}.

According to the results shown in Figure 7.15, the buckling load tends to decrease as the axial distance d_{arc} increases, although such a trend cannot be observed for configurations 19 and 20. Considering the experience gained in sections 7.1. and 7.2., small stiffeners should also be placed as close to the cutout as possible, also covering as much circumferential region of the cutout as possible. Thus, the upper and lower bounds for d_{arc} are chosen as 50 mm and 70 mm, respectively.

The effect of circumferential distance d_{st} between the straight stiffeners and the center of the cutout is already observed in sections 7.1. and 7.2 and it was found that the flange should be as close to the cutout as possible. Therefore, the upper and lower bounds for d_{st} is chosen as 65 mm and 100 mm, respectively.

7.3.2. Results of optimization with small stiffeners

Figure 7.16 shows the load vs end displacement plot of the optimum design found in optimization study with small stiffeners, along with the numerical results found in the model validation step for B100 reference cylinder.

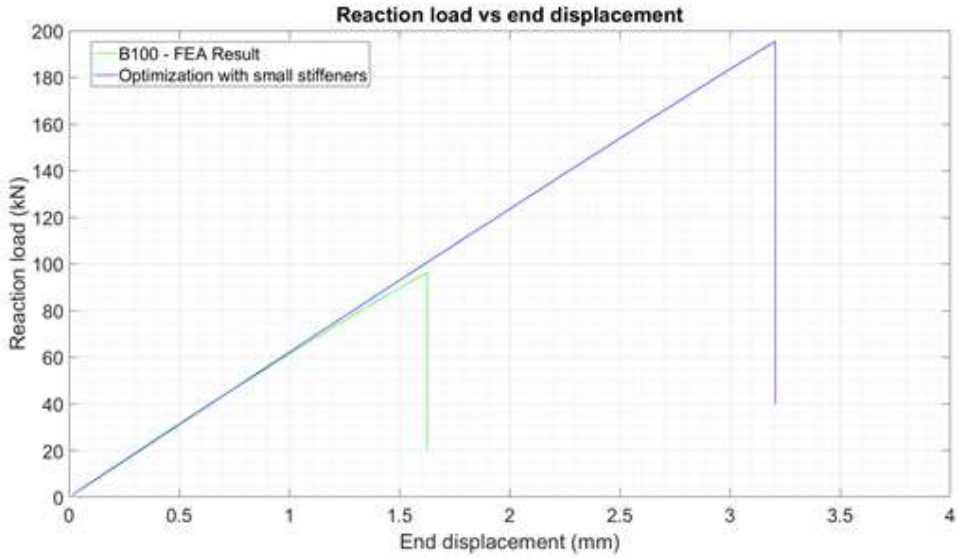

Figure 7.16. Reaction load vs end displacement for optimization with small stiffeners.

The optimum values of the geometric parameters defining the small stiffeners are given in Table 7.6.

Table 7.6. The optimum geometric properties of small stiffeners found.

$\theta_{arc}\ (degrees)$	$d_{arc}\ (mm)$	$d_{st}\ (mm)$	$F_{cr}\ (kN)$	m_{st} (kg)	$f_{objective}$
72.01	52.99	65.63	195.5	0.068	0.649678

The contour plots given in Figure 7.17 indicate that the buckling shape is changed compared to that found in Figure 7.11. This change is due to moving the stiffeners close to the cutout, which increases the bending stiffness against a deformation like that in Figure 7.11. However, the optimization study still results in an optimum design with straight stiffeners as close to the cutout as possible. This indicates that applying stiffeners on the lateral sections of the cutout is more effective in improving the buckling resistance of the structure compared to applying stiffeners to the top and bottom of the cutout.

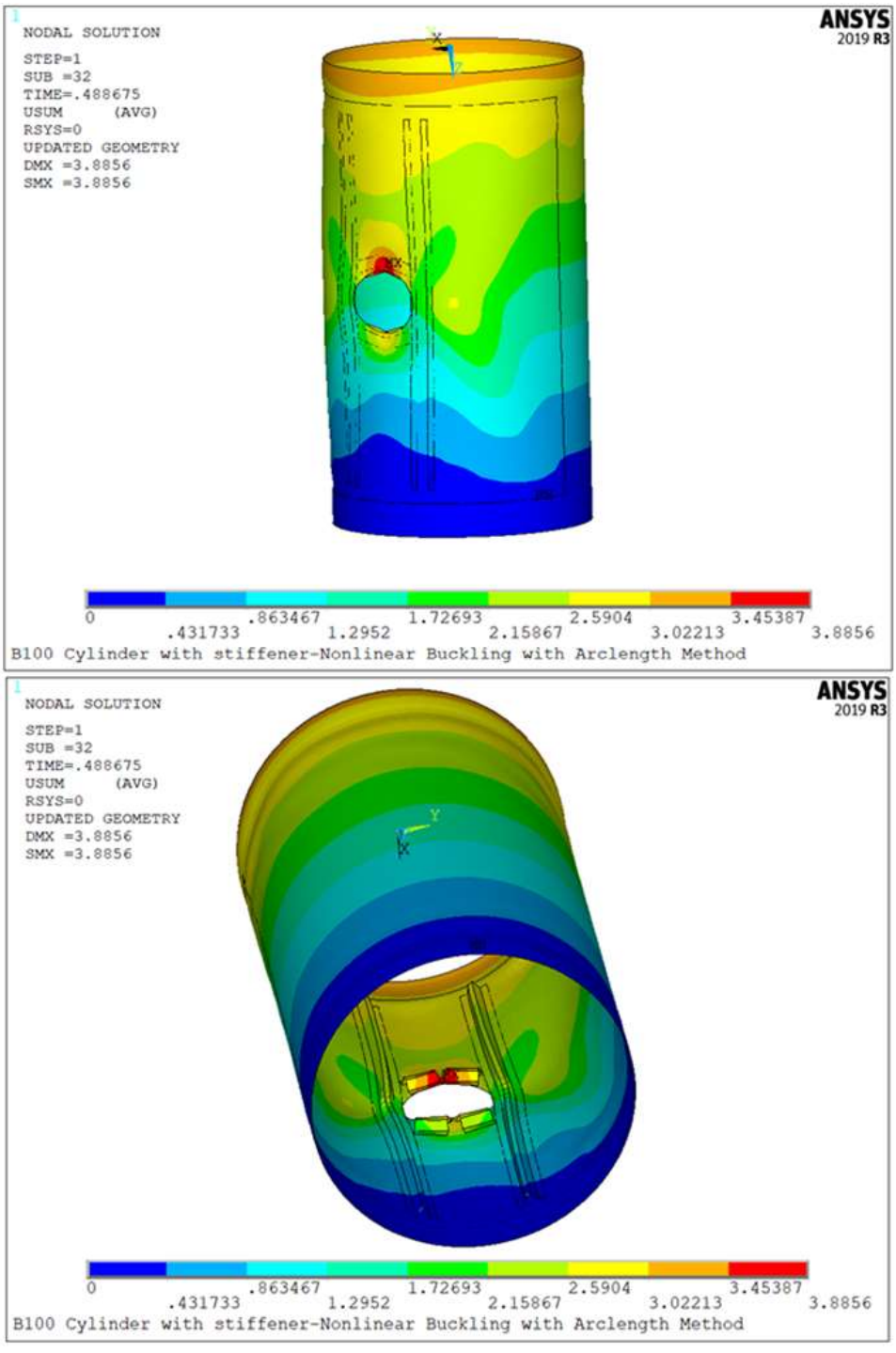

Figure 7.17. Resultant displacement contour plot of the optimum design with small stiffeners during buckling, with a scale factor of five.

7.4. Results of All Optimization Studies

Optimum configurations found in three optimization studies are shown in Table 7.7 where m_{st} denotes the mass of the stiffeners.

Table 7.7. Comparison of three optimization studies carried out.

Optimization Study	$m_{ur}\ (kg)$	$m_{st}\ (kg)$	$F_{ur}\ (kN)$	$F_{re}\ (kN)$	$f_{objective}$
Optimization #1	3.879	0.066	96.2	184.9	0. 669286
Optimization #2	3.879	0.060	96.2	192.8	0.653859
Optimization with small stiffeners	3.879	0.068	96.2	195.5	0.649678

According to the results given in Table 7.7, the best design is obtained by using only straight stiffeners in optimization #2, which gives a buckling load of 192.8 kN, a 100.4% increase compared to the unreinforced configuration, while adding an additional weight by 1.54%. The fact that the critical buckling load of the cylinder without cutout was measured as 182 kN in the reference experimental study, it can be concluded that not only the strength lost due to the introduction of the cutout is recovered but also the strength is increased even further. Thus, application of straight stiffeners is found highly effective in improving the buckling resistance of the structure by increasing the bending stiffness locally around the cutout.

The optimum design from the optimization with small stiffeners not only provides the highest amount of critical buckling load, 195.5 kN, but also the lowest objective function value amongst all three, even though it results in the maximum increase in the weight, 1.75%. That is because the objective function weighting coefficient used for the buckling load is more than double of that for the weight. Using a lower weighting coefficient for the buckling load and a higher weighting coefficient for the weight of the cylinder would yield an optimum design lighter but also weaker against buckling.

Comparing the optimization with small stiffeners to optimization #2, addition of small stiffeners only yields an extra gain of 1.4% in the buckling load found in the latter. Therefore, it can be concluded that use of straight stiffeners axially all along the cylinder and close to the cutout is much more effective compared to the small stiffeners applied on the top and bottom of the cutout.

8. RECOMMENDATIONS FOR FUTURE WORK

In this study, the buckling strength of a thin-walled composite cylindrical is improved via use of stiffener reinforcements. Although the buckling strength of the optimally reinforced cylinder is the double of that of the unreinforced one, there are some improvements that can be applied. The effect of ply orientations for straight stiffeners and small stiffeners can be analyzed and included to the model. Increasing the number of layers or the thickness of each layer of stiffeners can also increase the bending stiffness coming from stiffeners. In order to simulate the buckling more realistically, non-linear material model along with composite damage mechanisms can be included. By use of a progressive damage modelling, post-buckling behavior of the reinforced and unreinforced cylinders can be simulated as well.

This study is carried out using the geometries and the results of a reference study. The reference design that is optimized is not a real-life application. In the future, a similar structure with geometric sizes corresponding to a real-life application such as a fuselage of an aircraft of the main structure of a space shuttle can be optimally reinforced using the conclusions deduced from this study. For example, a higher number of holes with smaller cutout diameters can be introduced to the structure. Furthermore, the search for an optimum stiffener configuration away from the cutout can also be carried out using a different configuration than that used in the local region around the cutout.

9. CONCLUSIONS

The main objective of this study is to optimally reinforce a thin-walled composite cylindrical shell with a cutout. A parametric finite element model of a composite cylindrical shell with a circular opening is developed and validated using the results of an experimental and numerical study. Then straight stiffeners are placed at both sides of the cutout in the axial direction. The upper and lower limits to be used in the optimization studies are determined via a parametric study. Using a modified simulated annealing algorithm, optimizations are carried out considering different configurations and different design parameters. Using the optimum cross-sectional parameters, additional small stiffeners are placed to the top and bottom of the cutout, and a final optimization is carried out using the design parameters that define small stiffeners only. The parametric FE model and the optimization code are developed in Ansys Mechanical APDL.

Use of stiffeners is proved to be highly effective and useful for increasing the bending stiffness and therefore increasing the buckling resistance of the structure without significant increase in the structural weight. According to the results of the first level of the optimization, use of optimized straight stiffeners at the sides of the cutout leads to 100.4% increase in the critical buckling load of the cylinder while adding an extra 1.54% weight. It is also concluded that applying the stiffeners as close to the cutout as possible yields a higher buckling strength. Use of small stiffeners on the top and bottom of the cylinder improves the buckling load by an additional 1.4%. Therefore, the increase due to the application of the small stiffeners is found to be marginal compared to that due to the straight stiffeners.

REFERENCES

1. Jones, R. M., *Mechanics of Composite Materials*, Taylor & Francis, 2nd edn., 1998.

2. Shi, S., Z. Sun, M. Ren, H. Chen and X. Hu, "Buckling Response of Advanced Grid Stiffened Carbon-Fiber Composite Cylindrical Shells with Reinforced Cutouts", *Composites Part B: Engineering*, Vol. 44, No. 1, pp. 26–33, 2013.

3. Tennyson, R. G., "The Effects of Unreinforced Circular Cutouts on the Buckling of Circular Cylindrical Shells Under Axial Compression", *Journal of Manufacturing Science and Engineering, Transactions of the ASME*, Vol. 90, No. 4, pp. 541–546, 1968.

4. Jullien, J. F. and A. Limam, "Effects of Openings of the Buckling of Cylindrical Shells Subjected to Axial Compression", *Thin-Walled Structures*, Vol. 31, No. 1-3, pp. 187–202, 1998.

5. Han, H., J. Cheng, F. Taheri and N. Pegg, "Numerical and Experimental Investigations of the Response of Aluminum Cylinders with a Cutout Subject to Axial Compression", *Thin-Walled Structures*, Vol. 44, pp. 254–270, 2006.

6. Jacob, G., K. K. Divya and P. Prabhakaran, "Buckling Analysis of Cylindrical Shells Subjected to Axial Compression", *International Research Journal of Engineering and Technology(IRJET)*, Vol. 4, No. 4, pp. 3483–3486, 2017.

7. "Numerical and Experimental Study of the Response of Selected Compression-Loaded Composite Shells with Cutouts", *Collection of Technical Papers - AIAA/ASME/ASCE/AHS/ASC Structures, Structural Dynamics and Materials Conference*, Vol. 3, pp. 2338–2351, 1998.

8. Tafreshi, A., "Buckling and Post-Buckling Analysis of Composite Cylindrical Shells with Cutouts Subjected to Internal Pressure and Axial Compression Loads", *In-*

ternational Journal of Pressure Vessels and Piping, Vol. 79, 2002.

9. Arbelo, M. A., A. Herrmann, S. G. Castro, R. Khakimova, R. Zimmermann and R. Degenhardt, "Investigation of Buckling Behavior of Composite Shell Structures with Cutouts", *Applied Composite Materials*, Vol. 22, No. 6, pp. 623–636, 2015.

10. Çelebi, M. and H. S. Türkmen, "Buckling Analysis of Cfrp Composite Cylindrical Shell with Cutouts in Bending", *Journal of Aeronautics and Space Technologies*, Vol. 10, No. 2, pp. 1–9, 2017.

11. Hühne, C., R. Rolfes, E. Breitbach and J. Teßmer, "Robust Design of Composite Cylindrical Shells Under Axial Compression - Simulation and Validation", *Thin-Walled Structures*, Vol. 46, No. 7-9, pp. 947–962, 2008.

12. Taheri-Behrooz, F., M. Omidi and M. M. Shokrieh, "Experimental and Numerical Investigation of Buckling Behavior of Composite Cylinders with Cutout", *Thin-Walled Structures*, Vol. 116, pp. 136–144, 2017.

13. Gangadhar, L. and T. S. Kumar, "Finite Element Buckling Analysis of Composite Cylindrical Shell with Cutouts Subjected to Axial Compression", *International Journal of Advanced Science and Technology*, Vol. 89, pp. 45–52, 2016.

14. Senocak, E. and A. M. Waas, "Optimally Reinforced Cutouts in Laminated Circular Cylindrical Shells", *International Journal of Mechanical Sciences*, Vol. 38, No. 2, pp. 121–140, 1996.

15. Hilburger, M. W. and J. H. Starnes, "Buckling Behavior of Compression-Loaded Composite Cylindrical Shells with Reinforced Cutouts", *International Journal of Non-Linear Mechanics*, Vol. 40, No. 7, pp. 1005–1021, 2005.

16. Jingxuan, H., R. Mingfa, H. Qizhong, S. Shanshan and C. Haoran, "Buckling Behavior of Compression-Loaded Advanced Grid Stiffened Composite Cylindrical Shells with Reinforced Cutouts", *Polymers and Polymer Composites*, Vol. 19, No.

4-5, pp. 357–362, 2011.

17. Hao, P., B. Wang, K. Tian, G. Li, K. Du and F. Niu, "Efficient Optimization of Cylindrical Stiffened Shells with Reinforced Cutouts by Curvilinear Stiffeners", *AIAA Journal*, Vol. 54, No. 4, pp. 1350–1363, 2016.

18. Alhajahmad, A., M. M. Abdalla and Z. Gürdal, "Optimal Design of Tow-Placed Fuselage Panels for Maximum Strength with Buckling Considerations", *Journal of Aircraft*, Vol. 47, No. 3, pp. 775–782, 2010.

19. Albazzan, M. A., B. F. Tatting, R. Harik, Z. Gürdal, A. W. Blom-Schieber, M. Rassaian and S. Wanthal, "Design of Variable Stiffness Cylinder with Holes Under Bending for Maximum Buckling Load Using Lamination Parameters", *International SAMPE Technical Conference*, Vol. 2019-May, 2019.

20. Shojaee, T., B. Mohammadi and R. Madoliat, "Experimental and Numerical Investigation of Stiffener Effects on Buckling Strength of Composite Laminates with Circular Cutout", *Journal of Composite Materials*, Vol. 54, No. 9, pp. 1141–1160, 2020.

21. Wang, C. M., C. Y. Wang and J. N. Reddy, *Exact Solutions for Buckling of Structural Members. CRC Series in Computational Mechanics and Applied Analysis*, CRC Press Taylor & Francis Group, 2005.

22. Ugural, A. C., *Stresses in Beams, Plates, and Shells*, CRC Press Taylor & Francis Group, 2010.

23. Bathe, K.-J., *Finite Element Procedures*, Prentice Hall, 1996.

24. Ansys, *Academic Research Mechanical, Release 2019 R3, Help System, Theory Reference*, 2019.

25. Vasios, N., "Nonlinear Analysis of Structures", *The Arc-Length Method*, 2015.

26. Riks, E., "An Incremental Approach To the Solution", *International Journal of Solids and Structures*, Vol. 15, No. 7, pp. 529–551, 1979.

27. Crisfield, M., "A Fast Incremental/Iterative Solution Procedure That Handles "Snap-Through"", *Computational Methods in Nonlinear Structural and Solid Mechanics*, Vol. 13, pp. 55–62, 1981.

28. Arora, J. S., *Introduction to Optimum Design – Second Edition*, Elsevier, 2017.

29. Erdal, O. and F. O. Sonmez, "Optimum Design of Composite Laminates for Maximum Buckling Load Capacity Using Simulated Annealing", *Composite Structures*, Vol. 71, No. 1, pp. 45–52, 2005.

30. Kirkpatrick, S., C. D. Gelatt and M. P. Vecchi, "Optimization by Simulated Annealing", *Science*, Vol. 220, No. 4598, pp. 671–680, 1983.

31. Metropolis, N., A. W. Rosenbluth, M. N. Rosenbluth, A. H. Teller and E. Teller, "Equation of State Calculations by Fast Computing Machines", *The Journal of Chemical Physics*, Vol. 21, No. 6, pp. 1087–1092, 1953.

32. Ali, M. M., A. Törn and S. Viitanen, "A Direct Search Variant of the Simulated Annealing Algorithm for Optimization Involving Continuous Variables", *Computers and Operations Research*, Vol. 29, No. 1, pp. 87–102, 2002.

33. Akbulut, M. and F. O. Sonmez, "Design Optimization of Laminated Composites Using a New Variant of Simulated Annealing", *Computers and Structures*, Vol. 89, No. 17-18, pp. 1712–1724, 2011.

34. Meyer-Piening, H. R., M. Farshad, B. Geier and R. Zimmermann, "Buckling Loads of Cfrp Composite Cylinders Under Combined Axial and Torsion Loading - Experiments and Computations", *Composite Structures*, Vol. 53, No. 4, pp. 427–435, 2001.

APPENDIX A: PERMISSION TO REPRINT MATERIALS

The e-mail correspondence regarding the permission request to reprint materials used in this thesis report are shown in Figure A.1 - Figure A.3.

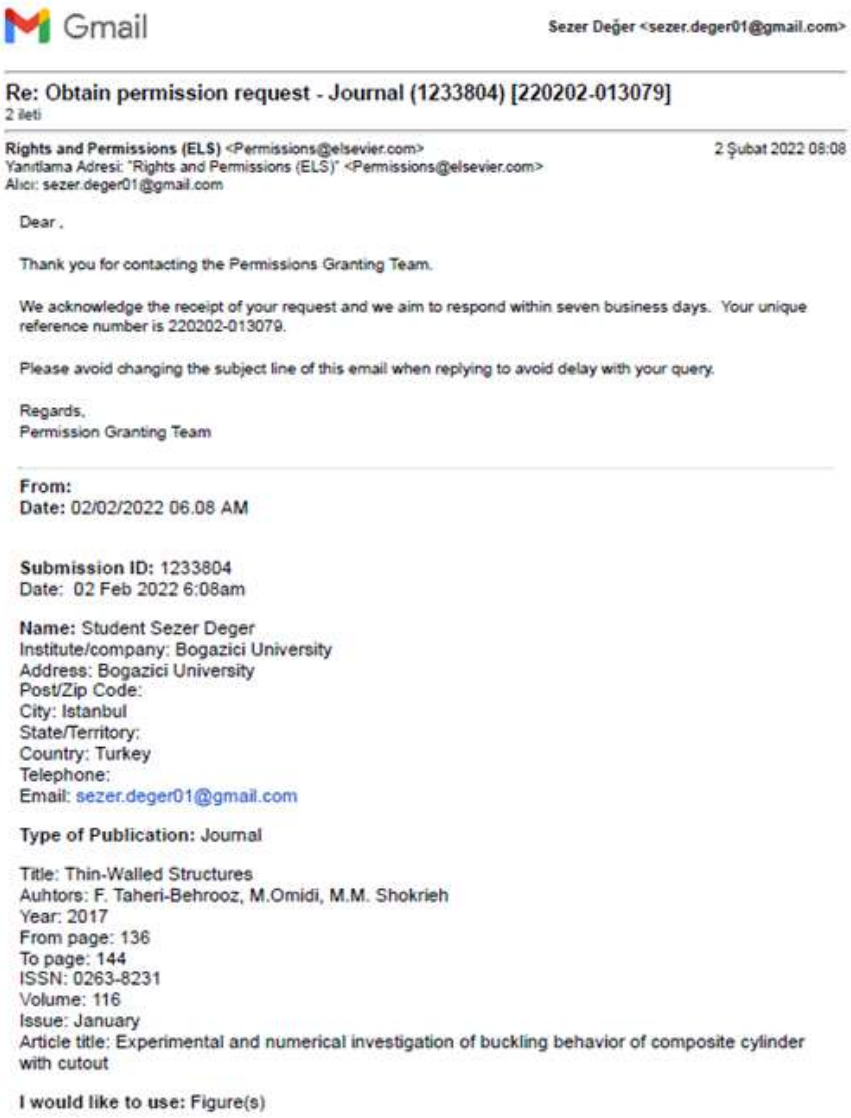

Gmail Sezer Değer <sezer.deger01@gmail.com>

Re: Obtain permission request - Journal (1233804) [220202-013079]
2 ileti

Rights and Permissions (ELS) <Permissions@elsevier.com> 2 Şubat 2022 08:08
Yanıtlama Adresi: "Rights and Permissions (ELS)" <Permissions@elsevier.com>
Alıcı: sezer.deger01@gmail.com

Dear ,

Thank you for contacting the Permissions Granting Team.

We acknowledge the receipt of your request and we aim to respond within seven business days. Your unique reference number is 220202-013079.

Please avoid changing the subject line of this email when replying to avoid delay with your query.

Regards,
Permission Granting Team

From:
Date: 02/02/2022 06.08 AM

Submission ID: 1233804
Date: 02 Feb 2022 6:08am

Name: Student Sezer Deger
Institute/company: Bogazici University
Address: Bogazici University
Post/Zip Code:
City: Istanbul
State/Territory:
Country: Turkey
Telephone:
Email: sezer.deger01@gmail.com

Type of Publication: Journal

Title: Thin-Walled Structures
Auhtors: F. Taheri-Behrooz, M.Omidi, M.M. Shokrieh
Year: 2017
From page: 136
To page: 144
ISSN: 0263-8231
Volume: 116
Issue: January
Article title: Experimental and numerical investigation of buckling behavior of composite cylinder with cutout

I would like to use: Figure(s)

Figure A.1. E-mail correspondance - 1.

Quantity of material: 6
I am the author of the Elsevier material: No
Elsevier author is involved in my project: No

In what format will you use the material: Print and Electronic
Translation: No

Proposed use: Reuse in a thesis/dissertation

Material can be extracted: No

Additional Comments / Information: Hello, The deadline of approval for my M.S. thesis is on February 23rd. It has to be reviewed beforehand, which requires about 2-3 weeks. Therefore, I need your help. May I have the permission as soon as possible? Best, Sezer Değer

---

—

Rights and Permissions (ELS) <Permissions@elsevier.com> 3 Şubat 2022 13:20
Yanıtlama Adresi: "Rights and Permissions (ELS)" <Permissions@elsevier.com>
Alıcı: sezer.deger01@gmail.com

Dear ,

We hereby grant you permission to reprint the material below at no charge in your thesis subject to the following conditions:

1. If any part of the material to be used (for example, figures) has appeared in our publication with credit or acknowledgement to another source, permission must also be sought from that source. If such permission is not obtained then that material may not be included in your publication/copies.

2. Suitable acknowledgment to the source must be made, either as a footnote or in a reference list at the end of your publication, as follows:

"This article was published in Publication title, Vol number, Author(s), Title of article, Page Nos, Copyright Elsevier (or appropriate Society name) (Year)."

3. Your thesis may be submitted to your institution in either print or electronic form.

4. Reproduction of this material is confined to the purpose for which permission is hereby given.

5. This permission is granted for non-exclusive world English rights only. For other languages please reapply separately for each one required. Permission excludes use in an electronic form other than submission. Should you have a specific electronic project in mind please reapply for permission.

6. As long as the article is embedded in your thesis, you can post/share your thesis in the University repository.

7. Should your thesis be published commercially, please reapply for permission.

Figure A.2. E-mail correspondance - 2.

This includes permission for the Library and Archives of Canada to supply single copies, on demand, of the complete thesis. Should your thesis be published commercially, please reapply for permission.

This includes permission for UMI to supply single copies, on demand, of the complete thesis. Should your thesis be published commercially, please reapply for permission.

8. Posting of the full article/ chapter online is not permitted. You may post an abstract with a link to the Elsevier website www.elsevier.com, or to the article on ScienceDirect if it is available on that platform.

Kind regards,
Subash Balakrishnan
Copyrights Coordinator
ELSEVIER | HCM - Health Content Management
Visit Elsevier Permissions

From: Administrator
Date: Wednesday, February 02, 2022 06:08 AM GMT

Dear ,

Thank you for contacting the Permissions Granting Team.

We acknowledge the receipt of your request and we aim to respond within seven business days. Your unique reference number is 220202-013079.

Please avoid changing the subject line of this email when replying to avoid delay with your query.

Regards,
Permission Granting Team

From:
Date: Wednesday, February 02, 2022 06:08 AM GMT
[Alıntılanan metin gizlendi]
[Alıntılanan metin gizlendi]

Figure A.3. E-mail correspondance - 3.